

Diss. ETH No. 17048

**NUMERICAL EXPLORATIONS ON  
STRESS HETEROGENEITY:  
DYNAMIC EARTHQUAKE RUPTURE AND  
NEAR-FAULT GROUND MOTION**

A dissertation submitted to

**ETH ZURICH**

for the degree of

**DOCTOR OF SCIENCES**

presented by

**JOHANNES RIPPERGER**

Diplom-Geophysiker Univ.,

Ludwig-Maximilians-Universität München

born August 24, 1974

citizen of Germany

accepted on the recommendation of

Prof. Dr. Domenico Giardini, examiner

Dr. P. Martin Mai, co-examiner

Dr. Jean-Paul Ampuero, co-examiner

Prof. Dr. Raul Madariaga, co-examiner

2007

Seite Leer /  
Blank leaf

From the moment I picked up your book until I laid it down,  
I was convulsed with laughter. Some day I intend reading it.

The Marx-Brothers

Hey-ho, let's go!

The Ramones

Seite Leer /  
Blank leaf

# Contents

<b>Zusammenfassung</b>	<b>1</b>
<b>Abstract</b>	<b>3</b>
<b>Introduction</b>	<b>5</b>
<b>1 Fast Computation of Static Stress Changes</b>	<b>11</b>
1.1 Introduction . . . . .	12
1.2 Method . . . . .	13
1.2.1 Description . . . . .	13
1.2.2 Range of Validity . . . . .	14
1.3 Example Calculations . . . . .	15
1.3.1 Synthetic Slip Distributions . . . . .	15
1.3.2 Past Earthquakes . . . . .	16
1.4 Conclusions . . . . .	19
<b>2 Heterogeneous Stress Drop</b>	<b>21</b>
2.1 Introduction . . . . .	22
2.2 Model Assumptions . . . . .	23
2.2.1 Stress Drop . . . . .	23
2.2.2 Nucleation Criterion . . . . .	24
2.2.3 Propagation and Arrest Criteria . . . . .	25
2.3 Rupture Properties in Stochastic Stress Drop Fields . . . . .	25
2.4 Discussion . . . . .	29
2.5 Conclusion . . . . .	32
<b>3 Dynamic Rupture with Stochastic Fault Stress</b>	<b>33</b>
3.1 Introduction . . . . .	34
3.2 Method . . . . .	37
3.2.1 Model Setup . . . . .	37
3.2.2 Loading and Nucleation . . . . .	40
3.3 Parameters and Non-dimensional Quantities . . . . .	41
3.4 Properties of the Dynamic Rupture Process . . . . .	42
3.4.1 Critical Load . . . . .	42
3.4.2 Stress Level . . . . .	43

3.4.3	Triggering Patch . . . . .	44
3.4.4	Initiation of Rupture . . . . .	46
3.4.5	Rupture Propagation Style . . . . .	48
3.4.6	Stress-dependent Size Transition . . . . .	49
3.5	Implications for Observable Macroscopic Properties . . . . .	51
3.5.1	Seismic Moment and Radiated Energy . . . . .	52
3.5.2	Moment Rate Spectra . . . . .	53
3.5.3	Hypocenter Location and Slip Distribution . . . . .	57
3.6	Discussion . . . . .	57
3.6.1	Nucleation . . . . .	57
3.6.2	Rupture Arrest . . . . .	58
3.6.3	Fracture Energy . . . . .	58
3.6.4	Slip Pulses . . . . .	59
3.6.5	High-Frequency Radiation . . . . .	59
3.6.6	Fault Boundary . . . . .	59
3.6.7	Plausible Stress Characterization . . . . .	60
3.7	Conclusions . . . . .	60
3.8	Appendix . . . . .	61
3.8.1	Approximation of Tectonic Loading . . . . .	61
3.8.2	Analysis of the Transition to Runaway Ruptures . . . . .	64
3.8.3	Estimation of Radiated Energy . . . . .	66
<b>4</b>	<b>Near-Field Ground Motion</b>	<b>69</b>
4.1	Introduction . . . . .	70
4.2	Dynamic Earthquake Rupture Simulations . . . . .	72
4.3	Computation of Synthetic Ground Motion . . . . .	77
4.3.1	Fault and Receiver Geometry . . . . .	77
4.3.2	Green's Functions . . . . .	79
4.4	Ground Motion Characteristics . . . . .	80
4.4.1	Example Waveforms . . . . .	81
4.4.2	Peak Ground Velocity . . . . .	82
4.4.3	PGV-Variability . . . . .	85
4.4.4	Spectral Acceleration . . . . .	90
4.5	PGV Variability of the 2004, Parkfield Earthquake . . . . .	93
4.5.1	Intra-event Variability . . . . .	93
4.5.2	Spatial Correlation of PGV . . . . .	95
4.6	Discussion . . . . .	96
4.7	Conclusions . . . . .	99
	<b>Conclusions and Outlook</b>	<b>101</b>
	Conclusions . . . . .	101
	Outlook . . . . .	102

<b>A Static Loading Procedure</b>	<b>105</b>
A.1 Introduction . . . . .	105
A.2 Efficient Solution . . . . .	105
A.3 The Algorithm . . . . .	106
<b>B Addendum to Chapter 3</b>	<b>109</b>
B.1 Spectra of Slip . . . . .	109
B.2 Stress Change . . . . .	113
<b>List of Tables</b>	<b>115</b>
<b>List of Figures</b>	<b>116</b>
<b>Bibliography</b>	<b>119</b>
<b>Curriculum Vitae</b>	<b>131</b>
<b>Acknowledgments</b>	<b>133</b>

# Zusammenfassung

Das Ziel der vorliegenden Dissertation ist es, die seismische Gefahrenanalyse in nächster Umgebung von Erdbeben-Bruchzonen zu verbessern. Dort sind die Erschütterungen an der Erdoberfläche am stärksten beeinflusst durch den Bruchprozess des Erdbebens, der sog. "Quelle". Aufgrund unzureichender Datendichte und der Vielzahl an Faktoren, die zur Komplexität des Bruchvorgangs beitragen können, ist kein umfassendes Verständnis der Variabilität der Bodenbewegung in der quellenahen Region vorhanden. Zur Verbesserung dieses Verständnisses können numerische Modellierungen des Bruchprozesses einen wichtigen Beitrag liefern.

Das Hauptaugenmerk dieser Arbeit liegt dabei auf der Auswirkung von heterogenen Scherspannungs-Verteilungen auf der Bruchfläche auf den Bruchprozess und die davon angeregte Bodenbewegung. Zu diesem Zweck führen wir numerische Simulationen der dynamischen Bruchausbreitung durch, in denen die Scherspannung durch ein zufallverteiltes Feld mit definierten statistischen Eigenschaften beschrieben ist. Eine wichtige Beobachtung in diesen Simulationen ist die Existenz eines Schwellenwerts im gemittelten Spannungszustand. Oberhalb dieses Schwellenwerts erfolgt ein scharfer Übergang von kleinen Beben, bei denen der Bruchprozess früh durch die Zonen niedriger Scherspannung gestoppt wird, hin zu systemweiten Beben, die nur noch durch die Ausdehnung der vorgegebenen Bruchfläche begrenzt sind. Wir beobachten dass der Mittelwert der Scherspannung, und damit die Lage ober- oder unterhalb des Schwellenwerts, hauptsächlich durch die Amplitude der räumlichen Spannungsverteilung beeinflusst wird. Während die kleineren Beben im Vergleich zu echten Daten niedrigere Bruchausbreitungsgeschwindigkeiten und seismische Abstrahlung zeigen, sind die makroskopischen Quellparameter der grossen Beben durchweg im Einklang mit Skalierungsbeziehungen beobachteter Daten.

Die beobachtbare Bodenbewegungen die durch die simulierten Bruchvorgänge hervorgerufen werden und insbesondere ihre Variabilität wird im letzten Abschnitt dieser Arbeit untersucht. Die maximalen Bodenbewegungen stimmen im langperiodischen Bereich gut mit empirischen Abminderungskurven überein und zeigen bei kurzen Perioden Abweichungen zu kleineren Werten. Die Variabilität der maximalen Bodenbewegung liegt in derselben Grössenordnung wie die der empirischen Daten. Dies deutet darauf hin, dass Unterschiede im Bruchprozess einen beträchtlichen Anteil der gesamten beobachteten Vari-



abilität ausmachen.

Der Inhalt der vorliegenden Arbeit behandelt die numerisch effiziente Berechnung von Spannungsänderungen, die Entstehung, Ausbreitung und Arretierung von Brüchen in heterogenen Spannungsfeldern und die resultierenden quellnahen Bodenbewegungen. Diese Dissertation stellt somit eine umfassende Studie der quellnahen Effekte dar, welche mittels der gewonnenen Erkenntnisse und der zur Verfügung gestellten Hilfsmittel potentiell in die seismische Gefahrenanalyse einfließen können.

# Abstract

This thesis aims at improving seismic hazard assessment close to earthquake faults. In this near-fault region the influence of the earthquake source on the observable ground shaking at the surface is largest. Due to the scarcity of observational data and the number of factors potentially contributing to the complexity of the source process, the variability of ground motion in the near-source region is not fully understood. Numerical modeling can help to improve this understanding.

The main emphasis of this work is placed on the effects of heterogeneous distributions of initial shear stress on the rupture process and the excited ground motions. To this end we perform numerical simulations of the dynamic rupture propagation, with initial shear stress described as a spatial random field with given statistical properties. An important observation in our simulations is the existence of a threshold value in the average stress level. At the threshold a sharp transition occurs between small events that are stopped early by the regions of low initial stress to system-wide events that are limited only by the imposed fault boundaries. We find that the average stress level, and thus the position above or below the transition, are mainly controlled by the amplitude of the stress heterogeneity. While the small events show reduced rupture velocities and seismic radiation compared to real data, the macroscopic source properties of the large events are found to be consistent with scaling relations of observed data.

The ground motions excited by the simulated dynamic ruptures and in particular their variability is investigated in the final part of the thesis. A comparison of peak ground motions to empirical attenuation relations shows a good match at long periods and an underestimation at short periods. The variability in our peak ground motion estimates is found to be on the same order as the variability in empirical data, therefore suggesting a strong contribution of source-effects to the empirically observed variability.

The contents of this work address numerically efficient stress-change calculations, investigations on rupture nucleation, propagation and arrest in a heterogeneous stress field and the resulting excitation of near-source ground motion. The thesis therefore presents a comprehensive study related to near-source effects which potentially can be folded into seismic hazard assessment by providing new understanding and effective numerical tools for the construction of future earthquake scenarios.

Seite Leer /  
Blank leaf

# Introduction

Earthquakes are forceful reminders that the human race inhabits an actively deforming planet. The larger ones pose a significant danger to man-made buildings and structures and thereby also to the life and health of their inhabitants. With world population still growing and cities expanding in endangered regions, the amount of lives and economic value at risk is continuously increasing.

The task to reduce the risk and protect people from the effects of earthquakes can not be formulated as a purely scientific problem. It has political, economical, societal and sometimes religious dimensions. For example it is known in principle how to improve the earthquake resistance of buildings, but still the majority of houses in many earthquake-prone regions do not fulfill the basic requirements of earthquake-safe design. Although a discussion of the particular reasons for this is beyond the scope of this thesis, it should be kept in mind that in general it needs more than scientific understanding to prevent natural phenomena like earthquakes from becoming human disasters.

Nevertheless, or maybe even *because* of that, scientists should strive to improve their understanding of earthquakes, because to spend the always limited resources for earthquake preparedness most effectively, it is important to gather the best available estimates of future earthquakes and their potential dangers. The techniques to do so comprise many fields: geologic mapping of faults, laboratory experiments on rock samples, paleoseismic investigations of past events, historical studies of earthquake reports and recordings, seismological and statistical analysis of instrumentally recorded seismicity and geodetic measurements of the ground deformation. There has been progress in each individual discipline, leading to an unprecedented level of knowledge and understanding of earthquake processes.

All these studies combined can provide an estimate of the potential type and size of a future earthquake on a given fault. Ideally, one would like to know *when* that earthquake will happen. The topic of earthquake prediction or forecasting has been the subject of many studies and scientific debates since decades of seismological research and will not be covered here. In this thesis we will rather focus on the next question one would like to have answered: What

happens, *if* a given earthquake takes place? In many applications, planning of buildings etc., it is important to quantify the level of ground shaking a given site is likely to experience in a defined time interval (e.g., the lifetime of a building). The process of estimating this likelihood by combining all the available information is known as seismic hazard assessment (SHA).

Many factors contribute to the motion of the ground experienced at a given site: First of all, there are factors related to the origin of the seismic waves, often termed "source effects". The seismic source is basically a sudden movement of rock masses past each other and the way this displacement takes place influences the characteristics of the seismic waves that are emitted by this process. These waves can then be modified in frequency and amplitude due to the structure of the earth's crust, ("path effects"). Finally, so called "site effects", the structure close to the site of interest (e.g., the soil conditions, topography) can additionally influence the incoming seismic wave field locally, such that recorded motions can vary on very short spatial scales. So the observed ground motion at the earth surface results from all three effects, where the relative contribution of each can strongly vary. In the region close to the seismic fault, the source process is expected to play an important role. The seismic source process and its effect on the ground motion in the near field are the main focus of this thesis.

Comprehensive studies of near-field ground motion based on observations have always suffered from a scarcity of recordings. In recent years the number of events with many near-fault recordings has increased, but they still remain the exception. Thus the data available today is still not sufficient to reliably estimate the statistical properties of ground motion close to active faults. Despite this limitation, researchers have derived so called empirical attenuation relations from the available data, often mainly based on observations at larger distances and extrapolated to the closest distances. These relations typically provide a measure of ground motion (e.g., peak ground acceleration) as a function of earthquake magnitude and distance. In applications in seismic hazard assessment the expected variability of ground motion around the average estimate is of great importance. However, due to the inhomogeneous datasets it has been difficult to estimate the variability and its potential dependency on distance, magnitude and frequency.

This is exactly the point, where numerical modeling may contribute to the assessment of seismic hazard. Simulating the processes on the fault that are responsible for the radiation of the seismic waves can help to understand the physical factors leading to the variability of observed near-source ground motion. Since all physical models are simplifications of the real world, the important question that has to be answered is which physical effects have to be included and which can be neglected, in other words: how detailed does a

model have to be? The general answer is: As detailed as necessary, as simple as possible. Therefore, to find the right level of detail one has to define the set of observations the model is supposed to explain. Then it is aimed for the simplest model with the fewest parameters that is still able to predict the observed data.

In the case of constructing earthquake source models for ground motion prediction, observational constraints are the macroscopic earthquake parameters like the ruptured surface, the seismic moment and the duration of the event. For many earthquakes kinematic models of the source process have been derived by fitting the recorded ground motions. These models describe the pattern and timing of displacements which is compatible with the observed ground motion, but not necessarily obeys the physical principles of fracture mechanics. Nevertheless, the heterogeneous distributions of fault displacement obtained from the kinematic models constitute important evidence for complexity in the faulting process, which any model of the physical fault processes should be able to reproduce. These models of the rupture process and the frictional sliding of rock interfaces past each other are termed dynamic models. In contrast to the kinematic models they are based on fundamental principles of fracture mechanics and rock physics.

Basic models originating from fracture mechanics are circular or elliptical cracks expanding symmetrically on a rupture plane under completely homogeneous conditions. While such models were instrumental in elaborating fundamental relations and still serve as important reference cases, they proved to be too simple to explain the observed complexities in real earthquakes. Which is not surprising, since of course it is known from geology that rocks are not homogeneous and fault structures are never perfectly planar. Instead we are faced with complex networks of connected faults, subject to variable physical conditions and embedded in heterogeneous rock formations. Therefore very general conclusions that have been reached in previous studies were that the geometry of the fault plays an important role and many of the parameters of earthquake models have to be inhomogeneously distributed over a fault.

This thesis focuses on the heterogeneity in the initial shear stress on a planar fault. As outlined above, in reality there is likely a heterogeneity in more parameters, but we deliberately keep much of the remaining model as simple as possible to isolate the effects of the stress heterogeneity. Theoretical considerations and observational studies provide first order limits on the plausible stress heterogeneity and guide our parameterization of stochastic fault stress. However, in the future it will become essential to further constrain the stress parameters by independent observations.

It is rather straightforward to produce some kind of randomness in a given model parameter. It is however not possible to understand the effect of this randomness on the model behavior from a single realization of such a model.

Many models have to be calculated to reliably estimate the average behavior and its variability. In this thesis we do not present something like a best model, but rather aim at understanding the effect of different kinds of stochastic stress heterogeneity on the response of the model.

This knowledge might prove very helpful in a research direction that is currently gaining increasing interest. Simulations of potential future earthquakes can be performed on an unprecedented computational scale with the steadily improving high-performance computing facilities. But such scenario simulations will gain much more reliability and acceptance if they are able to provide some error bounds on their results. A potential way to achieve this is to consider the uncertainty in the unknown source process of a simulated future earthquake by running multiple models with some randomized input parameters. The results of this thesis may provide important guidance on designing the input models for such deterministic scenario simulations.

The general organization of the thesis is as follows: The first part of the thesis introduces stress heterogeneity through a more technical study. In Chapter 1 we explore an efficient numerical tool to compute the static stress change distribution on a planar fault associated with a given distribution of displacement on that fault. We expand the approach by *Andrews* [1980] and validate the computed stress changes against results obtained with the analytical formulations derived by *Okada* [1992]. Since the formulation by *Andrews* [1980] relates displacement and stress changes in the frequency domain, the method can make use of the Fast Fourier Transform and is therefore computationally very efficient. This property makes it an interesting tool when stress changes have to be calculated for a large set of synthetic slip distributions as envisioned for scenario simulation using the pseudo-dynamic approach of *Guatteri et al.* [2003]. In addition the method became very useful at a later stage of the thesis, as will be shown in Chapter 3 and Appendix A for computing the stress changes due to quasi-static slip during the nucleation stage of an earthquake.

The main question addressed in Chapter 2 and 3 is to what extent simple analytical models can be used to predict the average behavior of a given class of complicated models of dynamic earthquake rupture. Whereas Chapter 2 starts with simplified 2-dimensional models, Chapter 3 extends this in more detail to the three-dimensional case. The common main feature of the dynamic models is a heterogeneous, random initial stress field characterized by a few statistical parameters. By systematic variation of these parameters we are able to extract their influence on the average model behavior. To first order, this average behavior can be reasonably well predicted by simple analytical models. These results constitute an important foundation for construction of earthquake scenarios with randomized input parameters.

The last part of the thesis establishes a direct link to current problems in seismic hazard assessment by taking a look at the actual ground motion that results from the dynamic rupture simulations of the preceding chapters. The dynamic rupture models themselves are only concerned with the processes on the fault, but it is mandatory to validate their predictions in terms of actual ground motion with observed data. To this end we compute synthetic seismograms at a number of hypothetical stations surrounding the fault and compare them to the empirically derived attenuation relations. We find a generally good agreement between the empirical and synthetic results, but we also note significant discrepancies in particular cases, pointing out strengths and weaknesses of both the empirical relations as well as our ground motion estimates.

The thesis is finally rounded up by a summary of the main findings and a discussion of their relevance and applicability to seismic hazard assessment, along with an outline of potential future research directions.



Seite Leer /  
Blank leaf

# Chapter 1

## Fast Computation of Static Stress Changes on 2D Faults from Final Slip Distributions

J. Ripperger and P. M. Mai

Published in Geophysical Research Letters as:  
Ripperger, J., and P. M. Mai (2004), Fast computation of static stress changes  
on 2D faults from final slip distributions, *Geophys. Res. Lett.*, 31, L18610,  
[doi:10.1029/2004GL020594](https://doi.org/10.1029/2004GL020594)

## Abstract

Computing the distribution of static stress changes on the fault plane of an earthquake, given the distribution of static displacements, is of great importance in earthquake dynamics. This study extends the approach developed by *Andrews* [1980], and compares it against existing analytical formulations. We present calculations for slip maps of past earthquakes and find that the stress-change results are accurate to about 1-2% of the maximum absolute stress change, while the computation time is greatly reduced. Our method therefore provides a reliable and fast alternative to other methods. In particular, its speed will make computation of large suites of models feasible, thus facilitating the construction of physically consistent source characterizations for strong motion simulations.

## 1.1 Introduction

One of the fundamental quantities in earthquake source physics is the static stress change associated with earthquake faulting. The static stress change on the fault plane itself is linked to the dynamics of earthquake rupture and hence also to the associated energy release and seismic radiation. Its knowledge is therefore required in dynamic rupture modeling of past (and future) earthquakes [*Peyrat et al.*, 2001]. Moreover, stress-drop distributions for simulated slip maps in scenario earthquakes for near-source strong-motion simulations allow to constrain the temporal rupture evolution [*Guatteri et al.*, 2003] and the energy budget of earthquake rupture [*Guatteri et al.*, 2004].

Estimating the distributed stress changes on the fault plane directly from seismological data is cumbersome [*Peyrat and Olsen*, 2004], and usually it is inferred from imaged slip distributions [e.g., *Bouchon*, 1997]. Kinematic source inversions have revealed the complexity of earthquake rupture at all scales [*Heaton*, 1990; *Somerville et al.*, 1999; *Mai and Beroza*, 2002]. Therefore, also static stress changes on the rupture plane are highly heterogeneous, exhibiting locally large stress drop in the region of high slip but also zones of stress increase.

*Okada* [1992] derived analytical expressions to compute static stress changes for given final displacements in an elastic homogeneous half space. In contrast, finite difference methods (FDM) [e.g., *Ide and Takeo*, 1997; *Day et al.*, 1998] and the discrete wavenumber method by [*Bouchon*, 1997] require knowledge of the entire slip-time history at each point of the fault, but these approaches return the complete spatio-temporal evolution of stress changes on a fault plane. However, computations are time consuming for all methods mentioned so far, particularly for large grid sizes.

In this study, we propose a shortcut to calculating stress changes on a 2D fault plane, based on the work by *Andrews* [1980]. He presented a wavenumber representation relating the distribution of static slip to the associated collinear

static stress change. We give a brief introduction of Andrews' method and our extensions to it and discuss its range of applicability. We then examine the method under various initial assumptions and evaluate its performance in terms of computational speed and accuracy, when compared to the analytical solutions obtained with Okada's formulations. This comparison is performed for synthetic slip distributions as well as for examples of inverted slip maps of past earthquakes.

## 1.2 Method

### 1.2.1 Description

For a given slip distribution  $D(\mathbf{x})$  on a planar fault *Andrews* [1974] presented the following expressions for the two components (parallel and perpendicular to the slip direction), of shear strain on the fault:

$$\varepsilon_{\parallel}(\mathbf{x}) = \frac{1}{8\pi} \iint \frac{1}{r} \left[ \frac{2(\lambda + \mu)}{\lambda + 2\mu} \frac{\partial^2 D(\mathbf{x})}{\partial x_{\parallel}^2} + \frac{\partial^2 D(\mathbf{x})}{\partial x_{\perp}^2} \right] dx_{\parallel} dx_{\perp} \quad (1.1)$$

$$\varepsilon_{\perp}(\mathbf{x}) = \frac{1}{8\pi} \iint \frac{1}{r} \left[ \frac{2(\lambda + \mu)}{\lambda + 2\mu} - 1 \right] \frac{\partial^2 D(\mathbf{x})}{\partial x_{\parallel} \partial x_{\perp}} dx_{\parallel} dx_{\perp} \quad (1.2)$$

Based on equation (1.1), *Andrews* [1978, 1980] developed a formulation which relates the slip-parallel shear-stress change to the slip distribution in the wavenumber domain:

$$\Delta\sigma_{\parallel}(\mathbf{k}) = K_{\parallel}(\mathbf{k})D(\mathbf{k}) \quad (1.3)$$

Here, written as functions of the wavenumber vector  $\mathbf{k}$ ,  $D$  is the static slip distribution,  $\Delta\sigma_{\parallel}$  is the component of shear-stress change parallel to the slip direction and  $K_{\parallel}$  is the static stiffness matrix given by

$$K_{\parallel}(\mathbf{k}) = -\frac{1}{2} \frac{\mu}{\sqrt{k_{\parallel}^2 + k_{\perp}^2}} \left[ \frac{2(\lambda + \mu)}{\lambda + 2\mu} k_{\parallel}^2 + k_{\perp}^2 \right], \quad (1.4)$$

with  $k_{\parallel}$  and  $k_{\perp}$  being the wavenumbers in the directions parallel and perpendicular to the slip direction, respectively, and  $\lambda$  and  $\mu$  being the Lamé constants. Starting from equation (1.2) and proceeding in an analogous manner, we derive a similar expression for the component of shear-stress change perpendicular to the slip direction:

$$\Delta\sigma_{\perp}(\mathbf{k}) = K_{\perp}(\mathbf{k})D(\mathbf{k}), \quad (1.5)$$

where the slip-perpendicular static stiffness function is given by

$$K_{\perp}(\mathbf{k}) = -\frac{1}{2} \frac{\mu}{\sqrt{k_{\parallel}^2 + k_{\perp}^2}} \left[ \frac{2(\lambda + \mu)}{\lambda + 2\mu} - 1 \right] k_{\parallel} k_{\perp}. \quad (1.6)$$

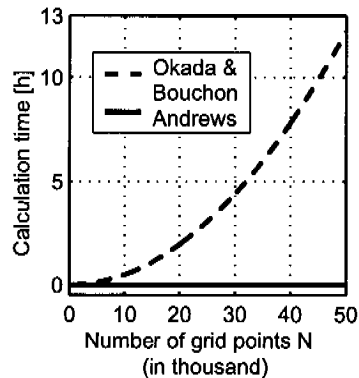


**Figure 1.1:** Comparison of calculation times observed on a 1.7 GHz PC. They are proportional to  $N^2$  for Okada's and Bouchon's method and to  $N \log N$  for Andrew's method. However, for Andrew's method also the proportionality factor is much smaller, so the total increase over the plotted range is only in the range of seconds, making the curve appear to be a horizontal line.

Calculating the static stress changes for a given slip distribution therefore only requires the Fourier transformation of slip into the wavenumber domain, application of equation (1.3) and (1.5) and the inverse transformation of  $\Delta\sigma(\mathbf{k})$  back into space domain. Varying rake angles are treated by splitting the total slip at each point in an along-strike and down-dip component and calculating parallel and perpendicular stress changes for each slip component separately. Then the resulting two distributions of the down-dip stress component are summed up, as well as the two distributions of the along-strike stress component. Especially for grids with a large number of points, Andrews' method reduces calculation time by several orders of magnitude compared to Okada's and Bouchon's method (Figure 1.1).

A general problem in calculating stress changes from slip arises if non-zero slip occurs at the edges of the fault plane. Non-zero slip at the fault boundaries constitutes a discontinuity in slip that will always lead to unrealistically high values of stress change at the edges. In our tests with synthetic slip maps we avoid this problem by using slip distributions which decrease to zero at all boundaries. In the case of inverted slip distributions for past earthquakes we reduce the influence of non-zero slip at the boundaries with the following procedure: The numerical grid is extended outward across the physical fault edges by 10 grid points, over which slip is tapered to zero. For both methods, computations are performed for the expanded slip distribution, but we only retain the inner part of the stress change distribution, corresponding to the original fault dimensions.

### 1.2.2 Range of Validity

Strictly speaking, equations (1.3) and (1.5) are valid for stress changes on a 2D fault plane embedded in a homogeneous full space, and hence several

limitations apply.

First of all, the shape of the fault to be modeled is restricted to a single 2D fault plane, thus excluding more complex fault geometries, e.g., multiple segments. In contrast, Okada's code allows for modeling arbitrary displacement and observation point positions. This is not a serious limitation, however, since for many seismological applications the assumption of a 2D fault plane constitutes a good approximation of the true, complex fault geometry.

Secondly, both Andrews' and Okada's formulation assume a homogeneous medium. We can approximately account for variations in shear wave velocity and density by scaling the calculated stress change with rigidity  $\mu$ . However, this can not take into account variations in Poisson's ratio  $\nu$ .

Finally, being defined for a full space, Andrews' method lacks the effect of the free surface, whereas Okada's formulations are valid for a half space. The resulting differences in the stress changes depend on the actual slip distribution, with the effect being stronger if large slip occurs at shallower depth. For the special case of strike slip on a vertical fault, the free-surface effect can be approximated by including a mirror image of the slip distribution above the free surface (*Steketee* [1958]), resulting in very small stress differences of 1-2% even for events with very large surface slip (e.g., Landers). However, the free-surface effect is generally alleviated by the fact that material strength usually decreases towards the free surface (rigidity often varies by a factor of about 2 between the uppermost and lowermost part of the fault plane, see next section for details). If depth-dependent rigidity is taken into account, the absolute stress change values are decreased in the uppermost low-strength part, also decreasing the differences due to the missing free-surface effect.

## 1.3 Example Calculations

### 1.3.1 Synthetic Slip Distributions

As a first test, we assume a simple strike slip fault embedded in a full space. To emulate the full space in the calculations with Okada's method, we position the fault top at 200 km depth. The fault plane is vertically dipping and has extensions of 20 km  $\times$  20 km, discretized with a spatial sampling of 0.2 km. Rigidity is set to  $\mu = 3.3 \times 10^{10}$  N/m<sup>2</sup> and a Poisson ratio of  $\nu = 0.25$  is assumed. Slip on the fault plane is modeled as  $d(x, z) = d_{\max} \cdot \exp(-r(x, z)^2/a^2)$  with  $d_{\max} = 1$  m,  $a = 2500$  m and  $r(x, z)$  being the distance to the center of the fault plane at (10,10) km. This yields a mean slip of 0.048 m and a magnitude of roughly  $M_W = 5.8$ .

The static stress changes in the slip-parallel component range from a maximum stress drop of 13.6 MPa to a maximum stress increase of 1.5 MPa. The absolute differences in both shear-stress components between the results of Andrews' and Okada's method are very small with maximum values of 0.05 MPa, equal to about 0.36 % of the maximum stress drop.

We repeat the calculation with Okada's method for the same slip distribution with the top of the fault plane coinciding with the free surface. In this case the influence of the free surface results in a difference of about 0.036 MPa ( $\approx 0.26\%$ ) at the surface. If we switch from strike slip to dip slip with the same distribution, we observe slightly higher differences of 0.12 MPa at the free surface, equal to 0.9% of the maximum stress drop. For source models with most of the slip happening in a depth of around 10 kilometers, the effect of the free surface is therefore negligible.

### 1.3.2 Past Earthquakes

In the next section we evaluate how Andrews' method performs for past earthquakes. We use published slip distributions obtained from inversion of strong-motion and/or teleseismic data. The slip models are interpolated onto a grid with 0.2 km spacing using a spline interpolation. In general the choice of the interpolation method is not trivial, but is of minor importance here, as we are interested only in the relative differences between the methods.

#### Morgan Hill

The 1984 Morgan Hill, California, earthquake provides an example of a pure strike-slip event on a buried fault. We use the slip model from *Beroza and Spudich* [1988]. The fault plane has dimensions of 10 km width and 30 km length. It extends from a depth of 2.5 km to roughly 12.5 km with a dip of  $85^\circ$ . The model comprises strike-slip displacement only (Figure 1.2a).

The calculated stress changes are scaled with the depth-dependent rigidity model (Figure 1.2d), derived from the velocity and density profiles specified by *Beroza and Spudich* [1988]. The differences between the static stress changes calculated with Okada's and Andrews' method have mean and maximum absolute values of 0.09 MPa and 1.82 MPa, respectively, corresponding to 0.1% and 1.9% of the maximum stress drop of 95 MPa.

#### Northridge

The 1994 Northridge earthquake constitutes an example of a thrust event on a shallow dipping fault. We use the slip model obtained by *Hartzell et al.* [1996], neglecting the slight rake variations in their model and treating the total slip amplitude to be pure dip slip (Figure 1.3a). The fault plane extends from 5 km to 21 km depth with a dip of  $40^\circ$ . It has dimensions of 20 km along strike and approximately 25 km down dip. A homogeneous medium is assumed, because the whole fault plane is located within a single layer of the velocity model used by *Hartzell et al.* [1996]. Figure 1.3 displays the stress changes calculated

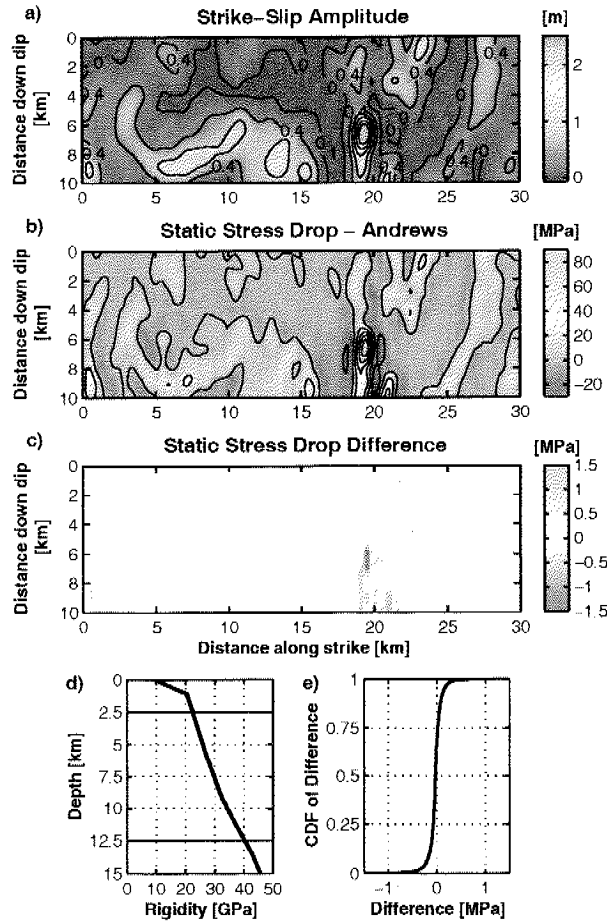


**Figure 1.2:** Morgan Hill earthquake. (a) Slip distribution interpolated from the model by *Beroza and Spudich* [1988]. (b) Static stress drop distribution calculated with Andrews' method. (c) Difference between the two calculated stress-drop distributions,  $\Delta\sigma_{Okada} - \Delta\sigma_{Andrews}$ . The regularity of the pattern is due to the interpolation of the slip map. (d) Depth dependent rigidity model used to scale the stress changes. Horizontal lines mark the fault extensions. (e) Cumulative distribution function of the stress-drop difference displayed in c).



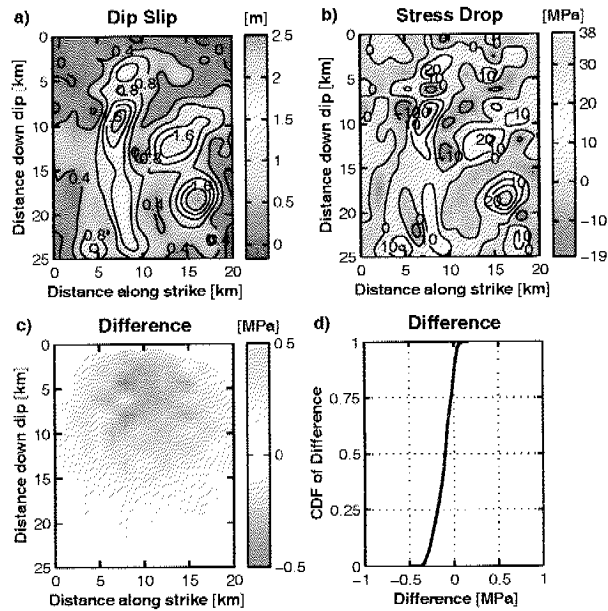


**Figure 1.3:** Northridge earthquake. (a) Slip distribution, modified from *Hartzell et al.* [1996]. The total slip amplitude is treated as being pure dip slip. (b) Down-dip component of static stress drop calculated with Andrews' method. (c) Difference in static stress drop calculated with both methods  $\Delta\sigma_{\text{Okada}} - \Delta\sigma_{\text{Andrews}}$ . The regularity in the pattern arises from the interpolation of the slip distribution. (d) Cumulative distribution function of the stress-drop difference displayed in c).

with Andrews' method and the difference to the Okada results. The most pronounced differences are observed in the upper part and can be attributed to the influence of the free surface. However, the differences remain small (0.1 MPa mean and 0.5 MPa maximum absolute value, equal to 0.3% and 1.3% of the maximum stress drop of 37 MPa).

### Loma Prieta

The 1989 Loma Prieta earthquake finally is a case in which significant amounts of both dip slip and strike slip have occurred. We use the inverted slip distribution from *Beroza* [1991]. The modeled fault plane has a width of 14 km and a length of 40 km, extending from about 5 km to 18 km depth with a dip of 70° (Figure 1.4). The observed stress drop differences are again in the same range (0.3 MPa mean and 1.5 MPa maximum absolute value, equal to 0.4% and 2.1% of the maximum stress drop of 72 MPa).

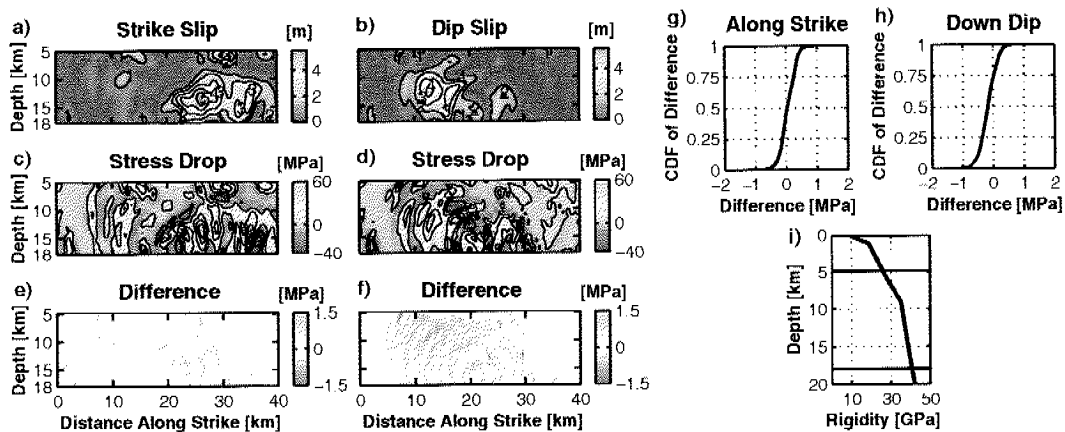


**Figure 1.4:** Loma Prieta Earthquake. (a) and (b) Strike-slip and dip-slip distribution, interpolated from the model by *Beroza* [1991]. (c) and (d) Along-strike and down-dip component of static stress drop calculated with *Andrews'* method. (e) and (f) Difference in along-strike and down-dip component of static stress drop, respectively, calculated as  $\Delta\sigma_{Okada} - \Delta\sigma_{Andrews}$ . (g) and (h) Cumulative distribution functions of the differences displayed in (e) and (f), respectively. (i) Depth dependent rigidity model used to scale the stress changes. It corresponds to the velocity and density model specified by *Beroza* [1991] for the region SW of the fault. Horizontal lines mark the fault extensions.

## 1.4 Conclusions

We have expanded the approach by *Andrews* [1980] for computing static stress changes on a two-dimensional fault plane from a given slip distribution, in order to account for both slip-parallel and slip-perpendicular stress changes. Computations with this method are fast, and especially for large grid sizes the increase in computation speed compared to other methods is enormous.

However, it has to be kept in mind that the formulation is valid only for stress changes on a fault embedded in a homogeneous full space. Under these assumptions, the calculated stress changes show little or no deviation (i. e.  $\approx 0.3\%$  of the maximum stress change) from results obtained with the analytical formulations derived by *Okada* [1992]. To evaluate the performance of *Andrews'* method for realistic model setups, we applied it to published slip maps from past earthquakes. We found, that the errors generally remain negligible (max.  $\approx 2\%$ , mean  $\approx 0.3\%$ ).

In particular, the accuracy is considered sufficient for the purpose of constraining dynamic rupture models and constructing physically consistent source characterizations for strong-motion simulations [*Guatteri et al.*, 2003]. Especially in the latter field of research, the speed of the method will provide an important advantage, allowing fast calculations for large sets of slip models.

## Acknowledgments

We thank M. Bouchon for providing his code to compute stress changes for finite-source models. We thank J. Andrews and one anonymous reviewer for valuable suggestions. Comments by G. Hillers, D. Schorlemmer, S. Wiemer and J. Wössner also helped to improve the manuscript. This is contribution No. 1356 of the Institute of Geophysics, ETH Zurich.

## Chapter 2

# Properties of Dynamic Earthquake Ruptures with Heterogeneous Stress Drop

J.-P. Ampuero, J. Ripperger and P. M. Mai

published in AGU Geophysical Monograph Series as:  
Ampuero, J.-P., J. Ripperger, and P. M. Mai (2006), Properties of dynamic earthquake ruptures with heterogeneous stress drop, in *Earthquakes: Radiated energy and the physics of faulting*, Geophys. Monogr. Ser., vol. 170, edited by R. Abercrombie et al., pp. 255-261, AGU, Washington, D. C., doi:10.1029/170GM25

## Abstract

Earthquake rupture is a notoriously complex process, at all observable scales. We introduce a simplified semi-dynamic crack model to investigate the connection between the statistical properties of stress and those of macroscopic source parameters such as rupture size, seismic moment, apparent stress drop and radiated energy. Rupture initiation is treated consistently with nucleation on a linear slip-weakening fault, whereas rupture propagation and arrest are treated according to the Griffith criterion. The available stress drop is prescribed as a spatially correlated random field and is shown to potentially sustain a broad range of magnitudes. By decreasing the amplitude of the stress heterogeneities or increasing their correlation length the distribution of earthquake sizes presents a transition from Gutenberg-Richter to characteristic earthquake behavior. This transition is studied through a mean-field analysis. The bifurcation to characteristic earthquake behavior is sharp, reminiscent of a first-order phase transition. A lower roll-off magnitude observed in the Gutenberg-Richter regime is shown to depend on the correlation length of the available stress drop, rather than being a direct signature of the nucleation process. More generally, we highlight the possible role of the stress correlation length scale on deviations from earthquake source self-similarity. The present reduced model is a building block towards understanding the effect of structural and dynamic fault heterogeneities on the scaling of source parameters and on basic properties of seismicity.

## 2.1 Introduction

Kinematic source inversions indicate that earthquake rupture is complex on a broad range of length-scales [Mai and Beroza, 2002]. However the details of fault dynamic weakening are beyond their intrinsic resolution limits [Guatteri and Spudich, 2000], which is in contrast with the high resolution of modern dynamic earthquake simulations. This warrants the introduction of more elementary rupture models that can nevertheless elucidate essential aspects of earthquake complexity. In linear elastic fracture dynamics (subshear) rupture is controlled by two parameters: stress drop and fracture energy [Freund, 1998; Hussein et al., 1975]. Both can be non uniform. Slip distributions inferred from seismological and geodetic data provide a valuable constraint on possible stochastic parameterizations of stress drop [Mai and Beroza, 2002; Lavallée and Archuleta, 2003]. Fracture energy might be the only dynamic parameter that can be robustly inferred from frequency-limited strong motion data [Guatteri and Spudich, 2000]. Rupture under non uniform stress or strength has been previously studied through numerical simulation [Day, 1982; Boatwright and Quin, 1986; Oglesby and Day, 2002] or statistical approaches [Heimpel, 1996; Rundle et al., 1998]. It is still important for strong ground motion prediction and for studies of source scaling to understand how the heterogeneity of me-

chanical fault parameters and initial conditions leads to variability of dynamic rupture properties. A computationally intensive approach consists on the statistical analysis of a large number of dynamic simulations with stochastic fault properties [Ripperger *et al.*, 2005]. As a preliminary step we explore here a simplified model based on fracture mechanics with emphasis on the effects of heterogeneous stress drop. Our aim is to identify and quantify the aspects of the spatial distribution of stress drop that control the overall tendency and variability of macroscopic source properties such as earthquake size, average rupture velocity, apparent stress drop, seismic moment and radiated energy. Here stress drop heterogeneities are mapped onto initial stress heterogeneities that mimic the result of prior seismicity and are prescribed as correlated stochastic fields parameterized by a few statistical quantities. We explore the parameter space using an efficient semi-dynamic model, formulated in the next section, that despite its simplicity encapsulates the main ingredients. In Section 3 a transition from Gutenberg-Richter (GR) to characteristic-earthquake (CE) frequency-size statistics is identified. The role of the stress correlation length on the scaling of source properties is highlighted and explained through a mean-field analysis of crack arrest. These results and further extensions are discussed in Section 4.

## 2.2 Model Assumptions

### 2.2.1 Stress Drop

We consider a 1D antiplane fault with coordinate  $x$  along strike. Linear slip-weakening friction is assumed, with uniform yield strength  $\tau_p$ , dynamic strength  $\tau_d$  and characteristic slip-weakening distance  $D_c$ . Neglecting dynamic overshoot and undershoot, the final stress is fixed to  $\tau_d$ . The stress  $\tau_0(x)$  at the onset of an earthquake results from the large scale tectonic stressing and from the previous seismicity contributing over a broad range of scales. Dynamic crack propagation is primarily sensitive to stress drop  $\Delta\tau(x) = \tau_0(x) - \tau_d$ , strength excess  $\tau_p - \tau_0(x)$  being essential only during nucleation and inplane super-shear transition. Simulating 3D seismic cycles in well resolved continuum models is still at the edge of our computational capabilities. Alternatively we can draw hypothetical stress fields from a statistical distribution, characterized by a few parameters, and study the properties of the resulting earthquake ruptures. *Mai and Beroza* [2002] found that coseismic slip distributions from finite-fault source inversions can be described as random fields with von Karman auto-correlation function. Our focus here is on correlated spatial distributions of available stress drop, with well defined standard deviation  $std$  and correlation length  $a_c$ . We consider normally distributed fields with truncated power law spectrum:

$$\Delta\tau(k) \propto std (a_c^{-2} + k^2)^{-(H/2+1/4)} \quad (2.1)$$

where  $k$  is the along strike wavenumber and  $H$  the roughness (Hurst) exponent. If  $H > 0$ , the auto-correlation function is well defined:

$$C(x) = \frac{(x/a_c)^H K_H(x/a_c)}{2^{H-1} \Gamma(H)} \quad (2.2)$$

where  $K_H$  is the modified Bessel function of the second kind, of order  $H$ , and  $\Gamma$  is the Gamma function. The mean value of  $\Delta\tau(x)$  is not prescribed arbitrarily but results from the nucleation process, as described in the next section.

### 2.2.2 Nucleation Criterion

In previous numerical studies [e.g., *Oglesby and Day, 2002*] the hypocenter location has been treated as a free parameter. Here, instead, it is determined in consistency with a mechanical analysis of nucleation. Instabilities on linear slip-weakening faults are preceded by aseismic slip, driven by tectonic load, in regions where stress overcomes the yield strength. As shown by *Uenishi and Rice [2003]*, this stable nucleation stage ends when the half-size of the slipping zone reaches the critical length

$$a_\nu = 0.5789 \frac{\mu D_c}{\tau_p - \tau_d} \quad (2.3)$$

This length is “universal” in the sense that it is independent of the spatial distribution of the initial stress  $\tau_0(x)$ . This result assumes that aseismic slip remains smaller than  $D_c$  and that stress peaks are well separated leading to weakly interacting nucleation sites. Both requirements are satisfied in particular when  $a_c \gg a_\nu$ . The uniform stress increase  $\tau_c$  required to reach instability and the location of the center of the nucleation zone are given by the minimum of a filtered version of the strength excess:

$$\tau_c = \min_x [(\tau_p - \tau_0) * \Phi_c] \quad (2.4)$$

where  $*$  denotes space convolution. The “nucleation filter”  $\Phi_c$  is the first eigenfunction of the elastostatic problem, rescaled to  $a_\nu$  and normalized to unit average. For all practical purposes it is approximated by

$$\Phi_c(\xi) = (0.6944 - 0.2312 \xi^2) \sqrt{1 - \xi^2} \quad (2.5)$$

for  $|\xi| \leq 1$ , where  $\xi = x/a_\nu$  [*Uenishi and Rice, 2003*]. The nucleation location and  $\tau_c$  are insensitive to stress heterogeneities of length scales much shorter than  $a_\nu$ . The stress drop  $\Delta\tau$  available for the ensuing earthquake is inherited from the nucleation process. For  $a_c \gg a_\nu$ , the aseismic stress drop can be neglected and

$$\Delta\tau(x) \approx \tau_0(x) + \tau_c - \tau_d = \tau_p - \tau_d + \tau_0(x) - \max[\tau_0 * \Phi_c] \quad (2.6)$$

Note that the contribution from the last two terms is proportional to *std*. We further restrict our attention to bilateral ruptures by symmetrizing each stress drop field with respect to its nucleation point, relocated at  $x = 0$  without loss of generality.

### 2.2.3 Propagation and Arrest Criteria

Dynamic rupture begins with an initial slip acceleration stage [*Campillo and Ionescu, 1997; Ampuero et al., 2002*] that we will not consider in our model. Soon after, crack-like rupture develops and the size of the process zone becomes small enough to warrant a small scale yielding approximation. The details of the friction law can then be ignored and rupture is governed by the balance between the energy release rate  $G$  flowing towards the crack tip and fracture energy,  $G_c = (\tau_p - \tau_d) D_c/2$  for linear slip-weakening. For a mode III crack of half-size  $a$ , rupture velocity  $V_R$  and stress drop  $\Delta\tau(x)$ :

$$G(v, a, \Delta\tau) = \sqrt{\frac{1 - V_R/c_S}{1 + V_R/c_S}} G^*(a, \Delta\tau) \quad (2.7)$$

with

$$G^*(a, \Delta\tau) = \frac{K^{*2}}{2\mu} \quad (2.8)$$

where  $c_S$  is shear wave velocity,  $\mu$  shear modulus and  $K^*$  the stress intensity factor that would prevail immediately after rupture arrest. Following the Griffith criterion, the rupture propagates with  $G = G_c$ , which provides a ‘‘crack tip equation of motion’’ [*Freund, 1998*], and stops if  $G^* \leq G_c$ . In general  $K^*$  is a convoluted function of crack growth history  $a(t)$  and stress drop  $\Delta\tau(x)$ , especially complicated by the interaction between the two crack tips [*Rose, 1976; Leise and Walton, 2001*]. After rupture arrest waves multiply diffracted at the crack tips bring  $K^*$  progressively, with oscillations, to its static value  $K_0$ . For symmetric non uniform stress drop:

$$K_0(a) = \sqrt{\pi a} \frac{2}{\pi} \int_0^a \frac{\Delta\tau(x)}{\sqrt{a^2 - x^2}} dx \quad (2.9)$$

A ‘‘semi-dynamic’’ approximation combines equations (2.7) and (2.8) with the assumption  $K^* \approx K_0$ . Although exact only for semi-infinite straight cracks, it has been applied with success to dynamic fracture problems involving branching and crack-microcrack interactions [*Bouchbinder et al., 2004, 2005*]. For our purposes, this approximation encapsulates the main dependency on stress drop heterogeneity, as will be illustrated later by favorable comparisons to fully dynamic 3D simulations. The criterion for crack arrest becomes

$$G_0 \doteq \frac{K_0^2}{2\mu} = G_c \quad \text{and} \quad \frac{dG_0}{da} < 0 \quad (2.10)$$

## 2.3 Rupture Properties in Stochastic Stress Drop Fields

For each realization of  $\Delta\tau(x)$ ,  $K_0(a)$  is computed by numerical integration of equation (2.9). The final earthquake size is determined as the crack size  $a$  at



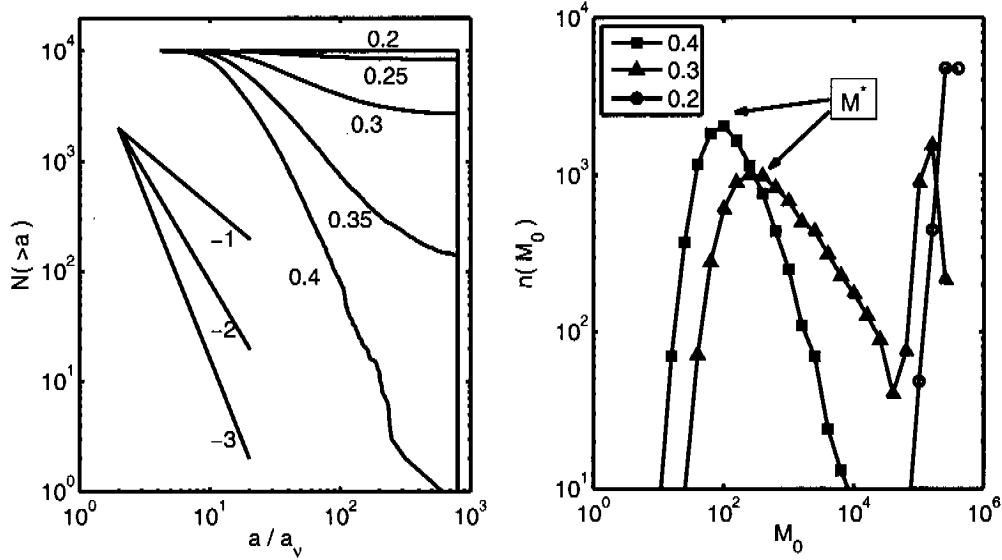


**Figure 2.1:** Frequency-size statistics in the semi-dynamic model: cumulative crack size distributions (left) and seismic moment histograms (right). Each curve contains  $10^4$  realizations of the stochastic stress field, with  $H = 1$ ,  $a_c = 5a_\nu$  and different values of  $std$  as indicated by labels (normalized by  $\tau_p - \tau_d$ ). The straight lines on the left are visual guides for power law distributions with exponents as labeled. A transition from GR-like to CE-like behavior is observed. The lower roll-off moment  $M^*$  of the GR is higher for smaller  $std$  and is related to both the nucleation length  $a_\nu$  and the correlation length  $a_c$ .

which  $G_0(a)$  becomes smaller than  $G_c$ . Figure 2.1 shows the distribution of earthquake sizes obtained at fixed  $H$  and  $a_c$  for different values of  $std$  (normalized by strength drop  $\tau_p - \tau_d$ ). Each curve contains  $10^4$  realizations of the heterogeneous stress field. The seismic moment is computed as [Madariaga, 1979]

$$M_0 = 2 \int_0^a \Delta\tau(x) \sqrt{a^2 - x^2} dx \quad (2.11)$$

Note that in this 2D model  $M_0$  is a seismic moment per unit of out-of-plane length and has units of force instead of newton-meters.

For high values of  $std$  the frequency-size distribution is reminiscent of a Gutenberg-Richter distribution (GR), with fast decay at large magnitudes and a lower roll-off moment  $M^*$ . At lower  $std$  we observe instead a characteristic-earthquake distribution (CE), with event sizes dominated by the highest magnitude, ultimately determined by the finite size of the modelled fault segment. To understand this transition we analyze the mean-field properties of the model. Figure 2.2-a shows the stress drop distribution stacked over  $10^4$  realizations as a function of hypocentral distance.

Assuming  $a_c \gg a_\nu$  this ensemble-averaged stress drop is related to the the auto-correlation function (2.2) by

$$\Delta\tau(x) \approx \tau_p - \tau_d + m \, std [C(x/a_c) - 1] \quad (2.12)$$

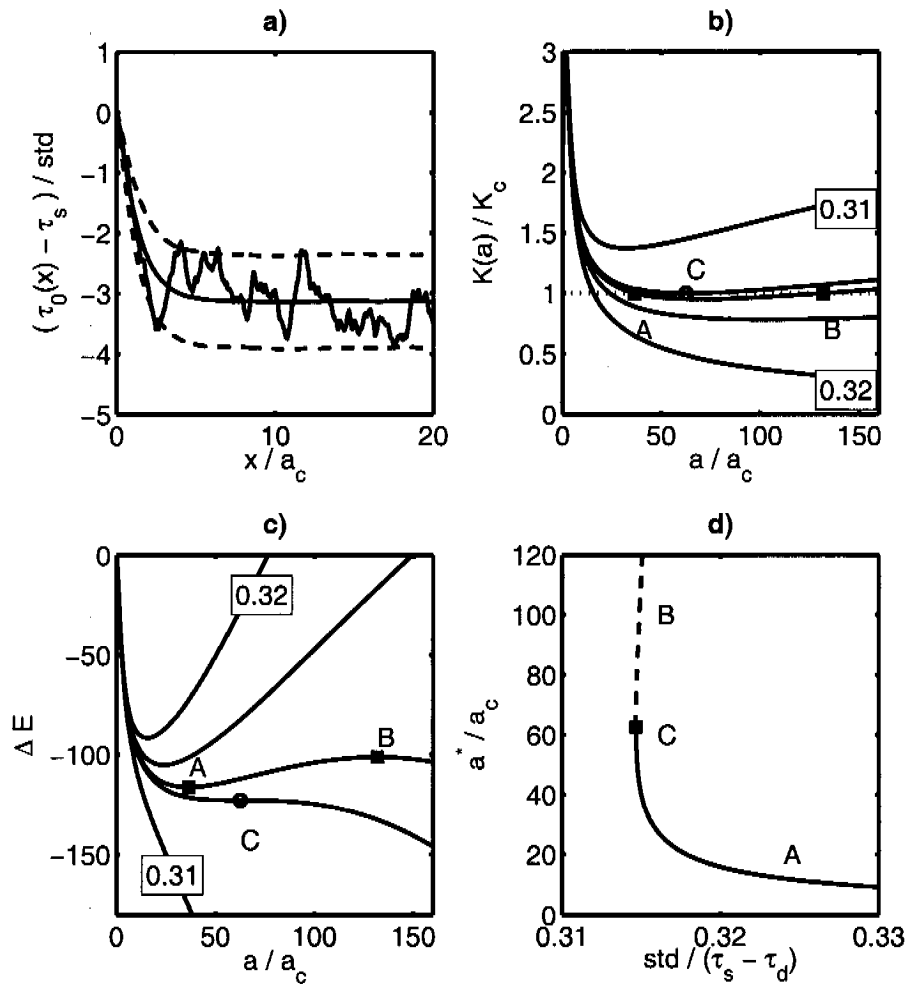


**Figure 2.2:** (a) Initial stress distribution as a function of hypocentral distance: typical realization (rough solid line), ensemble-average (smooth solid curve) with standard deviation (dashed curves). (b) Ensemble-averaged stress intensity factor and (c) total energy change as a function of crack size for some values of  $std$  within the range indicated by labels. Points A, B and C are stable, unstable and critical equilibria respectively, they verify  $K = K_c$  and are energy extrema. As  $std$  is reduced, A and B collapse into C, then disappear. (d) Crack length  $a^*$  corresponding to mean-field stable (solid curve, A) and unstable (dashed curve, B) equilibria as a function of  $std$ . The stable crack size is associated to the roll-off moment  $M^*$  of the frequency-size statistics. A discontinuous transition occurs at a critical  $std$  (point C).

where  $m$  is a slowly decreasing function of the ratio between  $a_c$  and whole fault size. The associated ensemble-averaged stress intensity factor (Figure 2.2-b) is

$$\bar{K}_0(a) \approx \sqrt{\pi a} \left[ \tau_p - \tau_d + m \text{ std} \left( \frac{2}{\pi} \int_0^a \frac{C(x/a_c)}{\sqrt{a^2 - x^2}} dx - 1 \right) \right] \quad (2.13)$$

For cracks growing far beyond the correlation length, following *Dyskin* [1999] the behavior of  $\bar{K}_0(a)$  is best understood as the competition between a uniform background stress drop,  $\Delta\bar{\tau} = \tau_p - \tau_d - m \text{ std}$ , and a pair of tangential point forces,  $F = m \text{ std} a_c \int_0^\infty C(\xi) d\xi$ , located at the crack center:

$$\bar{K}_0(a) \approx \sqrt{\pi a} \left( \Delta\bar{\tau} + \frac{2}{\pi} \frac{F}{a} \right) \quad (2.14)$$

Note how these two contributions have opposite dependencies on both  $a$  and  $\text{std}$ . For large enough  $\text{std}$  the arrest criterion (2.10) applied to  $\bar{K}_0$  leads to a typical crack size  $a^*$  that corresponds to the roll-off moment of Figure 2.1. If  $\text{std}$  is reduced the background stress drop  $\Delta\bar{\tau}$  becomes higher and  $F$  smaller,  $\bar{K}_0(a)$  curves upwards and  $a^*$  increases (Figure 2.2-b). Above a critical value  $\text{std}_c$ , for which

$$F\Delta\bar{\tau} = \mu G_c/4, \quad (2.15)$$

the arrest condition can no longer be met and ruptures run away, breaking the whole fault length. This transition is better visualized in Figure 2.2-c in terms of the total energy change

$$\Delta E = \int_{a_\nu}^a [G_c - G_0(a')] da' \quad (2.16)$$

The Griffith criterion for a stable equilibrium crack (2.10) is equivalent to a minimization of  $\Delta E$  with respect to  $a$ . For large  $\text{std}$  there is a distinct energy minimum corresponding to the stable equilibrium at crack arrest (point A in Figure 2.2). At a larger  $a$  there is an energy maximum corresponding to an unstable equilibrium state (point B). As  $\text{std}$  decreases the two equilibria collapse (point C) and disappear. The typical event size  $a^*$  does not diverge continuously at the transition but jumps to  $\infty$  from a finite critical size (Figure 2.2-d). From the condition (2.15) the critical size is found to scale as

$$a^* \propto \frac{a_c^2}{a_\nu} \quad (2.17)$$

and the critical  $\text{std}$  as

$$\text{std}_c \approx (\tau_p - \tau_d)/m \quad (2.18)$$

Two important source quantities are plotted in Figure 2.3, for a fault in the GR regime. An apparent stress drop is defined with reference to a constant stress drop crack:

$$\Delta\tau' = M_0/(\pi/2 a^2) \quad (2.19)$$

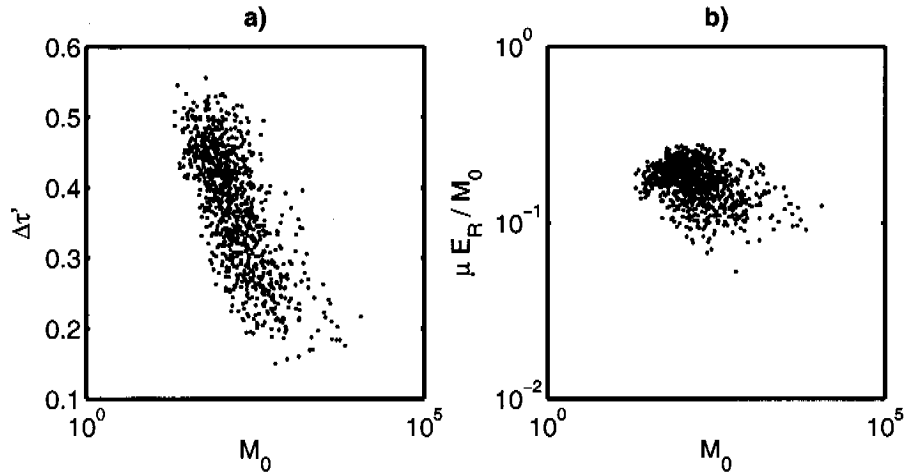


**Figure 2.3:** Apparent stress drop (a) and apparent stress (b) for  $10^3$  events with  $std = 0.4$ . All stresses are scaled by  $\tau_p - \tau_d$ . The observed magnitude-dependence, stronger for earthquake sizes comparable to the stress correlation length, is due to nucleation near stress peaks.

(Note again that  $M_0$  is in newtons.) Stress drop shows a tendency to decrease with moment, especially for earthquake sizes comparable to the correlation length  $a_c$ . This is expected from nucleation in regions of high stress. If stress is assumed constant ( $= \tau_d$ ) after the passage of the rupture front radiated energy is related to the total energy change during rupture (2.16) by [Husseini and Randall, 1976; Freund, 1998]:

$$E_R = -\Delta E \quad (2.20)$$

Radiated energy is overall constant in the logarithmic scale of Figure 2.3-b, although some weak tendencies are observed at the lowest ( $a < a_\nu$ ) and largest magnitudes ( $a > a_c$ ). The scale-dependency of these quantities is a combined signature of the correlation length  $a_c$  and the nucleation length  $a_\nu$ .

## 2.4 Discussion

The statistical properties of  $\Delta\tau(x)$  may be non stationary during the earthquake cycle. In models of seismicity featuring intermittent criticality the variability and correlation length increases as a large event approaches. As we make no attempt to describe the evolution of seismicity our analysis relates to ensemble statistics over snapshots of fault zones taken at a fixed stage of their cycle. In this way we identify intrinsic statistical features for given  $std$  and  $a_c$ , which can be useful to interpret more complete models of seismicity. These intrinsic statistics may be directly observable over a limited time window only if the time-scale of non-stationarity is longer. Fracture energy has been often understood as a material property although the paradigm of scale-dependent

$G_c$  has resurrected recently. A recurrent claim is that a constant  $G_c$  leads inevitably to run-away cracks, which is incompatible with the GR distribution of earthquake sizes. This argument holds for uniform stress drop but may not be reasonable for events breaking on natural faults that have sustained prior seismicity. The present model illustrates how a broad distribution of magnitudes can be generated solely by stress heterogeneities, without requiring a systematic scale-dependent  $G_c$ . In turn, assuming for instance  $G_c \propto a$  favors rupture arrest and promotes larger apparent stress drops. Statistical properties of rupture arising from uncorrelated heterogeneities of  $G_c$  have been studied by *Heimpel* [1996] and remain to be merged with the results of the present study.

A roll-off in frequency-size distributions at a low moment  $M^*$  is usually associated to catalog incompleteness. However, in dense borehole and deep mine monitoring networks  $M^*$  has been suggested to be above the detection threshold [*Heimpel and Malin*, 1998; *Richardson and Jordan*, 2002] and has been interpreted as a signature of a minimal nucleation size  $a_\nu$ , yielding an estimate of  $D_c$  in the high end of the laboratory range or much higher. Our analysis indicates that  $M^*$  may strongly depend on the correlation length of stress. The associated source size  $a^*$  can be much larger than  $a_\nu$  and, in the absence of an independent estimate of  $a_c$ , it cannot be mapped directly into a nucleation length.

The transition from GR to CE frequency-size statistics in the present semi-dynamic 2D model is relevant to understand some features of fully dynamic 3D simulations. Figure 2.4-left shows three ruptures simulated with the same stress drop distribution but different standard deviation  $std$ . At a critical value  $std_c$  the rupture percolates through the whole fault. As shown in Figure 2.4-right for a large collection of dynamic calculations [*Ripperger et al.*, 2005] this transition is well explained by the analysis proposed here, adapted to 3D with expressions of  $K_0$  for circular mode I cracks averaged over the crack contour as in *Dyskin* [1999]. The present model suggests that this is a first-order, discontinuous, transition. Although our presentation has focused on the effect of  $std$  a similar transition can be driven by an increasing correlation length at fixed  $std$ , as can be deduced from (2.18) noting that  $m$  is a decreasing function of  $a_c$ .

The current framework can be extended in many ways but also has intrinsic limitations. At present, only bilateral, symmetric, ruptures are considered and thus the effect of directivity has not been assessed. A generalization requires an efficient determination of the crack path in a random energy landscape. The model applies to events that do not break the whole seismogenic depth, otherwise the scaling of the energy release rate  $G$  should be modified. We consider only single connected cracks, although interaction and coalescence between many nucleation sites or dynamic triggering ahead of the rupture front is typically seen in our fully dynamic 3D models. Interaction between more than two cracks is hard to include. Our focus has been on crack-like

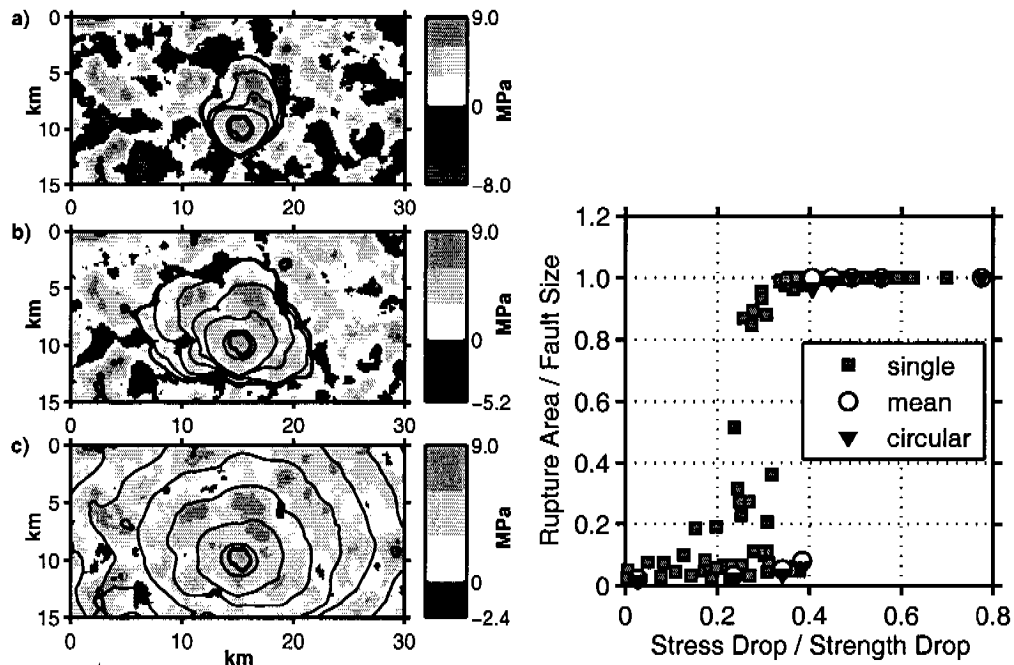


**Figure 2.4:** Properties of a collection of fully dynamic 3D rupture simulations with non uniform initial stress. (a-c) Rupture fronts for three simulations that differ only by the amplitude (*std*) of the available stress drop (gray scale). (right) Dependence of rupture area on fault-average stress drop (gray squares). Ruptures with small *std*, large stress drop, percolate through the whole fault. The transition to run-away events is well captured by dynamic simulations that start with the ensemble-averaged stress (circles) and by a mean-field analysis for circular mode I cracks (triangles).

ruptures, however earthquakes are often interpreted as short rise-time rupture pulses. Expressions of  $G$  for pulses are available but the relation between pulse width and some characteristic healing length contained in the stress/strength heterogeneity spectrum is still poorly understood. Although important aspects of 3D dynamic rupture cannot be rendered by the present model we believe it is a useful tool to guide the analysis of more complex models.

## 2.5 Conclusion

We have introduced a semi-dynamic model of earthquake rupture, based on fracture mechanics, to study the effect of spatially correlated stress drop heterogeneities on macroscopic source parameters and general properties of seismicity. We identified a transition in magnitude-frequency statistics from Gutenberg-Richter to characteristic earthquake, driven by the amplitude of stress drop heterogeneities. The stress correlation length plays an important role, appearing as a characteristic short length in the scaling behavior of macroscopic source properties, and may mask or may be confused with the signature of the nucleation process.

## Acknowledgments

We thank A. McGarr, R. Abercrombie and H. Kanamori for organizing the 2005 Chapman conference on Radiated Seismic Energy which provided the stimulating discussions that led to this work. J.-P. A. is grateful to T. Heaton, J. Schmittbuhl and A. Cochard for fruitful discussions. Funding for J.-P. A. was provided by SPICE, a Marie Curie Research Training Network in the 6th Framework Program of the European Commission. This is ETH contribution No. 1443.

## Chapter 3

# Earthquake Source Characteristics From Dynamic Rupture With Constrained Stochastic Fault Stress

J. Ripperger, J.-P. Ampuero, P. M. Mai and D. Giardini

Published in Journal of Geophysical Research as:  
Ripperger, J., J.-P. Ampuero, P. M. Mai, and D. Giardini (2007), Earthquake  
source characteristics from dynamic rupture with constrained stochastic fault  
stress, *J. Geophys. Res.*, 112, B04311, doi:10.1029/2006JB004515



## Abstract

One of the challenging tasks in predicting near-source ground motion for future earthquakes is to anticipate the spatio-temporal evolution of the rupture process. The final size of an event but also its temporal properties (propagation velocity, slip velocity) depend on the distribution of shear stress on the fault plane. Though these incipient stresses are not known for future earthquakes, they might be sufficiently well characterized in a stochastic sense.

We examine the evolution of dynamic rupture in numerical models of a fault subjected to heterogeneous stress fields with varying statistical properties. By exploring the parameter space of the stochastic stress characterization for a large number of random realizations we relate generalized properties of the resulting events to the stochastic stress parameters. The nucleation zone of the simulated earthquake ruptures in general has a complex shape, but its average size is found to be independent of the stress field parameterization and is determined only by the material parameters and the friction law. Furthermore, we observe a sharp transition in event size from small to system-wide events, governed mainly by the standard deviation of the stress field. A simplified model based on fracture mechanics is able to explain this transition. Finally, we find that the macroscopic rupture parameters (e.g., moment, moment rate, seismic energy) of our catalog of model quakes are generally consistent with observational data.

## 3.1 Introduction

The region close to active earthquake faults is the most challenging to deal with in terms of seismic hazard assessment. Not only is it the zone most likely to experience strong shaking and severe damage, but it is also the region with very large variability in observed ground-motion intensities (PGA) [e.g., *Shakal et al.*, 2006]. While part of the ground motion variability can be attributed to local site effects and/or (de-) amplification of waves due to complex geological structure, the contribution of earthquake source complexity to this variability is still not fully understood.

Despite an increasing number of strong motion recordings in recent years, observations for the very near-source region are still scarce, in particular for large earthquakes. Inferring the details of the source-rupture process and its effects on the resulting near-source motions is therefore strongly limited by the available data; this is even more accentuated when it comes to deducing statistical properties of earthquake ruptures. Events like the 1999 Taiwan earthquake generated a wealth of recordings, but this dataset still contains information only about one single realization of a large crustal thrust-faulting earthquake that produced extensive surface faulting. On the other hand, recent large strike-slip earthquakes, like the 1999 Izmit and the 2002 Denali earthquakes resulted only in few near-source recordings. Our ability to study earthquake

source complexity and to make statistically sound inferences about its effects on near-source ground motions, using observations alone, is therefore limited. Nevertheless, inversion of seismic and/or geodetic data of past earthquakes have inevitably shown that earthquakes are complex at all spatio-temporal scales [e.g., *Hartzell and Heaton*, 1983; *Beroza and Spudich*, 1988; *Wald and Heaton*, 1994; *Sekiguchi et al.*, 1996; *Delouis et al.*, 2002, and many others]. The potential origins of this imaged source variability are heterogeneities in fault stress, heterogeneities in material and friction parameters and complexity of the fault geometry.

This paper deals with the first possibility, i.e., with heterogeneous stress distributions on the fault plane. Early work on heterogeneous stress focused on generic cases, i.e., simple geometric configurations of high or low stress patches [e.g., *Day*, 1982; *Fukuyama and Madariaga*, 2000]. A number of studies have successfully constructed dynamic rupture models with highly heterogeneous stress fields to reproduce data for past events [e.g., *Miyatake*, 1992a,b; *Beroza and Mikumo*, 1996; *Bouchon*, 1997; *Olsen et al.*, 1997; *Ide and Takeo*, 1997; *Nielsen and Olsen*, 2000; *Peyrat et al.*, 2001; *Zhang et al.*, 2003]. These low-resolution images of dynamic earthquake rupture allow us to visualize stress heterogeneity on the fault plane, but they still represent only particular realizations of source complexity for a small number of earthquakes. They have not been used to attempt a more general, quantitative investigation of stress heterogeneity and its effects on rupture dynamics.

Unfortunately, the parameters and quantities governing the dynamics of an earthquake (e.g., stress on the fault) cannot be determined experimentally prior to an earthquake. What might be estimated with sufficient accuracy, however, are statistical descriptions of the stress field. *Oglesby and Day* [2002] went in that direction by numerical modeling of dynamic ruptures with various cases of strength variabilities combined with heterogeneous stress, using random stress fields that were constructed in a somewhat ad-hoc manner. Their work, however, did not attempt to statistically quantify the effects of different parameterizations of stress variability on the dynamic rupture process and the resulting ground-motions. In contrast, earlier work by *Andrews* [1980, 1981] discusses static and kinematic stochastic models of earthquake rupture, with stress heterogeneity described by a power-law decay of its wave-number spectrum, and their effects on the radiated wave-field. Following this line of thought and adding some simplifying assumptions (e.g., rupture geometry), *Frankel* [1991] established some general connections between stress heterogeneity, the characteristics of far-field displacement amplitude spectra and the frequency-size statistics of earthquakes. Based on this approach, fractal descriptions of fault slip have been used [e.g., *Herrero and Bernard*, 1994; *Zeng et al.*, 1994; *Gallovic and Brokesova*, 2004] for ground-motion simulation, while other studies estimate statistical parameters to characterize the heterogeneity of slip [e.g., *Mai and Beroza*, 2002; *Lavallée and Archuleta*, 2003; *Liu-Zeng et al.*, 2005; *Lavallée et al.*, 2006] and relate those to the faulting process.

In the present study we employ a concise and quantifiable statistical description of stress distribution in order to examine the dynamic rupture behavior due to different parameterizations of stress heterogeneity. The motivation for this work stems from the preceding discussion and the question of how heterogeneity in the initial stress conditions on the fault plane affects rupture nucleation, propagation and arrest. Under what general conditions does rupture nucleate and propagate and exhibit properties similar to observed earthquakes? Rather than focusing on single events we carry out a large number of fully spontaneous dynamic rupture simulations for many realizations of heterogeneous initial stress fields for a variety of stochastic-field parameters. This allows us to investigate ensemble statistics of dynamic rupture under inhomogeneous stresses and to determine general patterns in the response of this system that can then be compared against analytical predictions and observations. It is important to point out that we are not modeling seismicity evolution or full earthquake cycles. Our statistical description represents ensemble statistics of possible fault zone states. These states can either be determined by the maturity of the fault in terms of their geological evolution [e.g., *Wesnowsky*, 1988; *Hillers et al.*, 2007], or can be viewed as a particular state due to the background seismicity just before an impending earthquake.

In contrast to previous works with rather generic characterizations of stress heterogeneity, we adopt a spectral description of initial stress as a self-affine correlated random field with a power-law decay at high wave numbers. This approach follows the characterization of slip in past earthquakes by *Mai and Beroza* [2002], and allows us to generate many different stress patterns that differ in their details (i.e., for each realization) but are statistically identical. In choosing this method, we vary the parameters describing the fractal stress distribution, always retaining some common characteristics of the different classes of heterogeneous input stress fields. Moreover, instead of imposing a nucleation point and size, we apply a simplified approach to mimic tectonic loading, coupled to an algorithm for finding the physically most consistent rupture nucleation region (generally of geometrically complex shape).

We point out that we also fix fracture energy for simplicity since its scale-dependency is still actively debated [e.g., *Abercrombie and Rice*, 2005; *Mai et al.*, 2006], and its non-homogeneous parameterization, in conjunction with heterogeneous stress, yields a vast parameter space that would be difficult to fully explore. Moreover, we instead attempt to isolate and understand the effects of stress heterogeneity on dynamic rupture before including (potentially correlated) heterogeneous distributions of two (or more) dynamic quantities into the modeling strategy. Within the simplifying assumptions in our dynamic modeling, our technique provides a fully self-consistent physical model for earthquake nucleation and propagation, allowing us to investigate the statistics for a large number of rupture simulations with different parameterizations of stress heterogeneity.

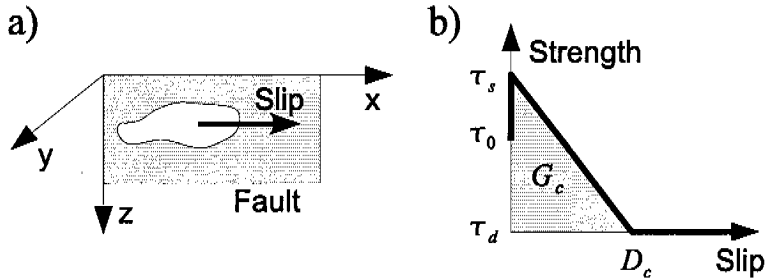


**Figure 3.1:** a) Geometry of the problem. Slip is occurring on a rectangular fault in the  $xz$ -plane. b) Linear slip-weakening friction law. Once stress has reached the static yield level  $\tau_s$ , strength decreases linearly with slip, until it reaches the dynamic frictional level  $\tau_d$  at the critical slip-weakening distance  $D_c$ . The area under the curve represents fracture energy  $G_c$ .

The paper is laid out as follows: In section 3.2 we introduce the model setup, the numerical scheme, and the stochastic characterization of heterogeneous stress we use. We then present the results for various stress heterogeneity parameterizations in terms of nucleation and propagation behavior of a large set of model quakes; we then investigate the resulting dynamic ruptures in terms of their overall scaling properties, their moment-rate functions and radiated seismic energy. This enables us to infer which heterogeneity characterization is perhaps the most plausible when comparing our simulations against observations. Our results suggest that it should be possible to place constraints on stress heterogeneity from independent observations which potentially could help to infer general properties of the rupture process of future earthquakes on a given fault.

## 3.2 Method

### 3.2.1 Model Setup

To single out the effects of the heterogeneity in shear stress, we restrict the rest of our model to relative simplicity. We consider a planar fault embedded in a homogeneous, elastic full space. This setting can be treated numerically very efficiently with a boundary integral method. The dynamic rupture calculations presented here are performed using a spectral boundary integral method coded by *Dunham* [2005], following the methodology of *Geubelle and Rice* [1995]. The fault is rectangular and slip on the fault is governed by a linear slip-weakening friction law (Figure 3.1). The critical slip-weakening distance  $D_c$  is assumed to be uniform over the whole fault, as are the static yield strength  $\tau_s$  and frictional sliding strength  $\tau_d$ . By fixing  $D_c$  in the slip-weakening model, along with constant strength drop  $\tau_s - \tau_d$ , we constrain fracture energy  $G_c$  and hence seismic radiation to values roughly consistent for moderate-size to large earthquakes ( $M_W \approx 6.4-6.8$ ), representing a magnitude range particularly important for

near-source seismic hazard. In contrast, small earthquakes generated via this approach will be characterized by relatively high fracture energy, resulting in rather low seismic radiation in the higher-frequency range. However, since we focus on studying earthquake dynamics for seismic hazard applications, we deliberately accept the limitations our current modeling strategy places on the smaller magnitude events.

There is no free surface, but the fault is surrounded by unbreakable barriers on all sides, which are modeled by setting  $\tau_s$  to a practically unreachable value. Following *Ampuero et al.* [2006] we adopt a spectral description of initial shear stress as a self-affine correlated random field with a power-law decay at high wave numbers. In the wave-number domain the stress field is constrained to a two-dimensional amplitude spectrum  $\tau(k)$ , where  $k = \sqrt{k_x^2 + k_z^2}$  and  $k_x$ ,  $k_z$  are the wave-number components in the  $x$  and  $z$  directions, respectively. In particular, the spectrum has a plateau below a given corner wave number  $k_c$ , while above  $k_c$  the decay is governed by the Hurst exponent  $H$  [e.g., *Voss*, 1988; *Mai and Beroza*, 2002]:

$$\tau(k) \propto \begin{cases} k_c^{-(1+H)} = \text{const} & \text{for } k \leq k_c \\ k^{-(1+H)} & \text{for } k > k_c. \end{cases} \quad (3.1)$$

Particular random realizations are constructed in the Fourier domain by specifying the amplitude according to equation (3.1) and adding phase values consisting of random numbers uniformly distributed between  $[0, 2\pi]$ . After performing the two-dimensional inverse Fourier transform under the constraint of Hermitian symmetry, the resulting distributions  $\tau(x, z)$  in the space-domain (Figure 3.2) have an approximately Gaussian distribution of amplitude values. The stress distributions are then scaled to a given standard deviation  $std$  controlling the absolute amplitude variations. Thus, apart from the probability density function (pdf), the random stress fields are controlled by the three parameters  $H$ ,  $a_c$  and  $std$ , where  $a_c$  denotes the correlation length  $a_c = 2\pi/k_c$ . This parameter also appears in the spectral description of von Karman fields adopted in *Mai and Beroza* [2002] and *Ampuero et al.* [2006]. Variations of these three parameters will be studied in the main part of this paper.

Recent work by *Lavallée and Archuleta* [2003] and *Lavallée et al.* [2006] suggests that slip and stress distributions on real faults may follow a non-Gaussian pdf with a broader range of values. A more general class of pdf's allowing for the occurrence of extreme values is provided by the Levy pdf [*Lavallée et al.*, 2006]. However, the Levy distributions are characterized by four parameters instead of the two needed for a Gaussian distribution, thus constituting a higher degree of complexity. Considering the other simplifying assumptions outlined above, we do not consider it necessary to go beyond the simpler case of Gaussian pdf's in this study. In particular the assumption of uniform strength drop limits the admissible range for extreme stress drop values. Accordingly, initial tests with heavy tailed Levy distributions yield either extremely large preslip values (larger than  $D_c$ ) due to very narrow stress peaks and/or regions

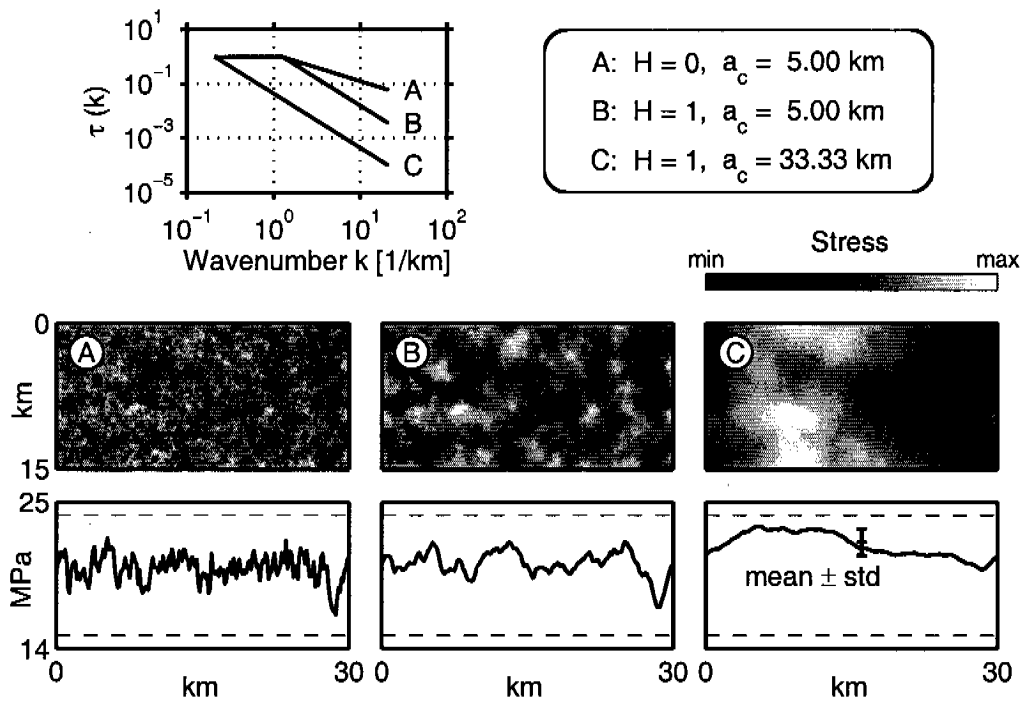


**Figure 3.2:** Illustration of random stress field generation. **(top)** Prescribed Fourier amplitude spectra for three different combinations of Hurst exponent  $H$  and correlation length  $a_c$ . Shown are one-dimensional slices (at  $k_z=0$ ) of the two-dimensional spectra  $\tau(k_x, k_z)$ , normalized to  $\max(\tau)=1$ . **(middle)** Example random realizations of initial stress for the wave number spectra given above. **(bottom)** Along-strike profiles of the stress fields above. Profiles are taken at the center of the fault. Upper and lower dashed lines indicate the yield and frictional stress level, respectively.

where stress is far below the frictional sliding strength. Both cases are rather unlikely to appear on real faults. Additional tests considering uniformly distributed random stress values indicated no significant differences in the model response compared to the case of Gaussian distributions.

### 3.2.2 Loading and Nucleation

In our modeling approach, we assume that tectonic loading occurs as uniformly increasing shear stress on the fault plane, raising the initial stress field to a critical state, i.e., to a stress state where any further loading leads to dynamic rupture propagation. In this context “dynamic” refers to propagation not driven by tectonic loading anymore, but by the stress changes induced by the propagating rupture itself. We further assume that nucleation can be accurately described as a quasi-static process, also governed by linear slip-weakening. This case has been studied analytically for two-dimensional (2-D) in-plane and antiplane ruptures by several researchers [e.g., *Campillo and Ionescu*, 1997; *Uenishi and Rice*, 2003]. One remarkable result of the analysis by *Uenishi and Rice* [2003] is the existence of a critical nucleation length, which depends only on the material properties and the slope of the friction law, but not on the particular shape of the stress function. For the in-plane fracture mode this length is given by

$$a_\nu = 1.158 \frac{\mu}{1 - \nu} \frac{1}{W}. \quad (3.2)$$

where  $\mu$  and  $\nu$  are the shear modulus and Poisson ratio of the medium, respectively. For the antiplane fracture mode the term  $1 - \nu$  has to be dropped. The slope of the slip-weakening friction law is defined as  $W = (\tau_s - \tau_d)/D_c$ , where  $\tau_s$  and  $\tau_d$  are the static and dynamic frictional strength, respectively. Some results for special cases of 3-D ruptures were given by *Uenishi and Rice* [2004], but there is no analytical solution available for the general 3-D case. Here, we approximate the loading process by finding the critical state of stress (i.e., the last stable stress state just prior to dynamic instability) through an iterative procedure. It involves dynamic rupture calculations for small subsections of the fault plane and is described and discussed in detail in Appendix 3.8.1. It is important to note that the procedure employed neglects the effects of quasi-static preslip and therefore tends to underestimate the size of the nucleation zone while overestimating the critical load (i.e., the increase in stress necessary to reach the critical stress state), affecting therefore also the actual values of stress in our numerical results. We have recently developed an improved algorithm to correctly solve the quasi-static problem associated with uniform tectonic loading, including preslip and the resulting stress redistribution (to be presented in a forthcoming paper). Initial results show that our general conclusions are not affected by the bias introduced by the approximating procedure used throughout the present paper.

Parameter	Symbol	Value
Density	$\rho$	2800 kg/m <sup>3</sup>
P-wave velocity	$v_p$	6000 m/s
S-wave velocity	$v_s$	3464 m/s
Critical slip-weakening distance	$D_c$	0.2 m
Yield strength	$\tau_s$	24 MPa
Frictional sliding strength	$\tau_d$	15 MPa
Grid spacing	$\Delta x$	150 m
Time sampling	$\Delta t$	0.013 s
Fault dimensions		15 × 30 km

**Table 3.1:** General modeling parameters used in all dynamic rupture simulations presented in this paper. The only exception being Figure 3.3, where some results for  $D_c = 0.4$  m have been added.

### 3.3 Parameters and Non-dimensional Quantities

To characterize and generalize the properties of the dynamic rupturing process, we explore the space of parameters quantifying the stochastic shear stress, while the frictional parameters and the fault geometry are kept constant. The general parameters which are not varied in this study are listed in Table 3.1. We will discuss our results in terms of the following nondimensional quantities: First of all, the Hurst exponent  $H$  controls the high wave number falloff of the stress spectrum. It is related to the fractal dimension  $D$  by  $D = E + 1 - H$ , where  $E$  is the Euclidean dimension, and hence for our 2-D distributions  $D = 3 - H$ . We consider  $H = 0, 0.5, 1$ , equivalent to

$$|\tau(k > k_c)| \propto k^{-1}, k^{-1.5}, k^{-2}. \quad (3.3)$$

This is the same range as discussed by *Andrews* [1980] for his static stochastic fault model, where  $|\tau(k)| \propto k^{-1}$  is required for strict geometrical self-similarity of the ruptures with stress drop being independent of rupture size. By fitting focal mechanism data of earthquakes in Southern California, *Smith* [2006] estimated a 1-D falloff exponent of  $\sim 0.8$  for stress, equal to a 2-D falloff  $|\tau(k)| \propto k^{-1.3}$  or a Hurst exponent of  $H \approx 0.3$ , which lies within the range of our parameterization.

The second quantity is given by the ratio  $a_\nu/a_c$  of the nucleation length  $a_\nu$  to the correlation length  $a_c$  of the stress field. As a proxy for the nucleation length we use the critical length for 2-D in-plane rupture as given by equation (3.2). For the parameters listed in Table 3.1 the nucleation length is therefore  $a_\nu \approx 1153$  m. For the correlation length  $a_c = 2\pi/k_c$  we choose one value on the



order of the whole fault length ( $a_c = 33.33$  km) and one where the correlation length is substantially shorter than the fault dimensions ( $a_c = 5$  km), thereby yielding  $a_\nu/a_c \approx 0.035$  and  $0.231$ , respectively.

The ratio  $std/(\tau_s - \tau_d)$  of the standard deviation of the stress field to the total strength drop constitutes the third nondimensional quantity. From the viewpoint adopted here stress heterogeneity arises from previous seismicity. The amplitude of stress concentrations at the edges of previous ruptures is on the order of  $\tau_s - \tau_d$  and the amplitude of troughs due to dynamic stress overshoot are expected to be less than 30% of  $\tau_s - \tau_d$ . Then, with a fixed value of  $\tau_s - \tau_d$  and an approximately Gaussian distribution of stress values, this would imply a value of  $std/(\tau_s - \tau_d)$  smaller than approximately 0.16. We cover a wider range by varying this ratio from roughly 0.11 to 0.33 ( $\tau_s - \tau_d = 9$  MPa,  $std = 1, 2, 3$  MPa), where the last case may lead to stress troughs unrealistically far below the frictional strength.

In addition, it proves insightful to consider a quantity describing the average stress level at the critical stress state in relation to the total strength drop. We use the nondimensional ratio of average available stress drop to total strength drop

$$\bar{\tau}_0 = \left\langle \frac{\tau_0 - \tau_d}{\tau_s - \tau_d} \right\rangle, \quad (3.4)$$

where the angle brackets denote averaging across the fault plane.

### 3.4 Properties of the Dynamic Rupture Process

Let us now examine the characteristics of nucleation, propagation and arrest for more than 400 dynamic rupture models with variable degrees of stress heterogeneity. We will first investigate the conditions of the critical load and the associated stress levels. The size and shape of the triggering patch, the initiation of rupture, its propagation style and the stress-dependent size transition will be discussed. All these parameters are generally only accessible in numerical simulations, and cannot be easily inferred from observational data.

#### 3.4.1 Critical Load

The critical load  $\Delta\tau_c^\infty$  is defined as the amount of stress which has to be added uniformly to reach the critical stress state (see section 3.2.2 and Appendix 3.8.1), starting from a stress state at which the maximum of the shear stress coincides with the yield strength. We expect to see a dependence of the critical load on the ratio  $a_\nu/a_c$ . The smaller the nucleation length  $a_\nu$  is in relation to the correlation length  $a_c$ , the less loading is expected to be necessary. For  $a_\nu \leq a_c$  we empirically find the critical load  $\Delta\tau_c^\infty$  to depend on the ratio  $a_\nu/a_c$

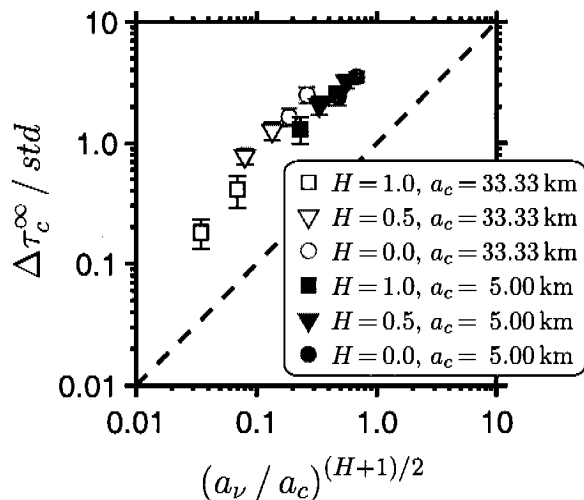


**Figure 3.3:** Scaling of critical load  $\Delta\tau_c^\infty$  with ratio  $a_v/a_c$  and  $H$ . Each symbol and its error bars represent the mean and the standard deviation of 30 random realizations. Since  $\Delta\tau_c^\infty$  is normalized by the standard deviation of the stress field  $std$ , results for different  $std$  would plot almost exactly on top of each other. Hence only the results for  $std = 1$  MPa are shown to improve clarity. Two data points appear for each parameter set because results for  $D_c = 0.2$  m and  $D_c = 0.4$  m are displayed.

as:

$$\Delta\tau_c^\infty \propto std \left( \frac{a_v}{a_c} \right)^{(H+1)/2} \quad (3.5)$$

Note that the critical load scales linearly with the standard deviation of the stress field  $std$ , a result that follows from dimensional analysis when slip is smaller than  $D_c$ , a typical situation during nucleation. These relationships are depicted in Figure 3.3, where results for a larger value of  $D_c$  ( $D_c = 0.4$  m) and thus a larger  $a_v$  are included to better illustrate the scaling over a broad range. So if the statistical properties of the stress field and the friction law are known or can be approximately inferred from independent observations, these relationships provide a good estimate of the amount of tectonic loading necessary to initiate dynamic rupture and of the duration of precursory aseismic slip.

### 3.4.2 Stress Level

After the tectonic load is applied, stress on the fault is in a critical state, where any additional loading will trigger dynamic rupture. As mentioned in section 3.3, the average stress level at this critical stress state is expressed by  $\bar{\tau}_0$ , defined as the average ratio between stress drop and total strength drop.

Figure 3.4 depicts the dependency of this measure on the statistical stress parameters. Two main features can be identified: (1) Stress levels are higher for smaller values of  $std/(\tau_s - \tau_d)$ , which is the expected behavior, because at the

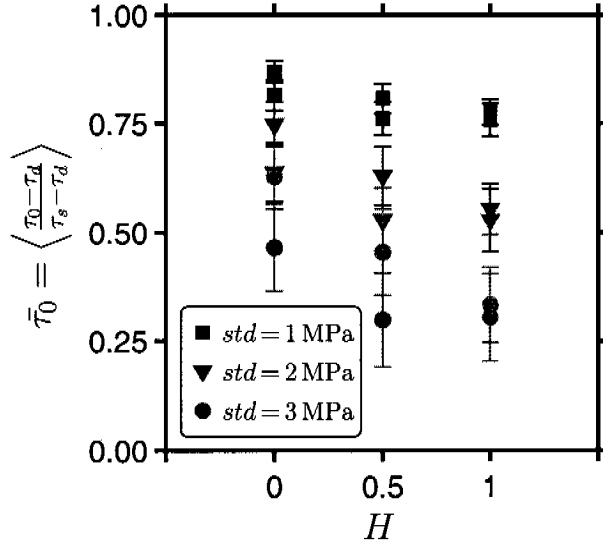


**Figure 3.4:** Average stress level  $\bar{\tau}_0$  versus Hurst exponent  $H$  for three different standard deviations. Each symbol and its error bars represent the mean and the standard deviation of 30 random realizations. Note the strong influence of the standard deviation.

critical stress state, for smaller  $std$  all points on the fault will on average be closer to the yield stress than for larger  $std$ . (2) Stress levels increase slightly with decreasing Hurst exponent  $H$ . Stress levels from a reference 2-D analysis, however, do not exhibit the latter dependency, so probably the stress levels are biased towards higher values by our approximative procedure of finding the critical stress state (see section 3.2.2 and Appendix 3.8.1).

In either case, the average stress level at the critical stress state is most strongly influenced by the quantity  $std/(\tau_s - \tau_d)$ , i.e., by the amplitude of the stress heterogeneity. In the following, the stress level will be shown to be a key parameter in our model, controlling the propagation and final size of the ruptures.

### 3.4.3 Triggering Patch

As mentioned in section 3.2.2, the ruptures in our simulations are triggered by a patch of the fault with stress slightly above the yield level of the material. The individual triggering patches are found through the iterative procedure described in Appendix 3.8.1 and are ultimately determined by the shape of each particular random realization of the initial stress function. As a first-order characterization of triggering patch size we use the radii of circumscribed and inscribed circles (Figure 3.5). We find that the inner radius is an approximately constant property over all the parameter variations of the stress field. This confirms that nucleation takes place on a common length scale, depending only on the friction law and the material parameters, similar to what has been shown for the 2-D cases [Uenishi and Rice, 2003]. The critical half lengths for

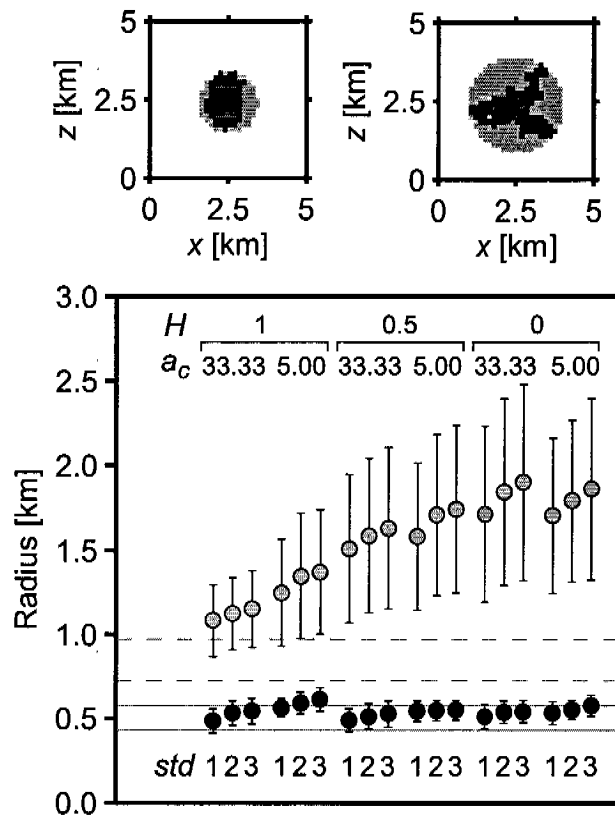


**Figure 3.5:** (top) Examples of obtained triggering patches (black) and their circumscribed (light gray) and inscribed (dark gray) circles. (bottom) Radii of circumscribed and inscribed circles. Plotted are the mean radii for 30 random realizations of each parameter set (x axis) with error bars of one standard deviation. Solid lines indicate the two 2-D nucleation half lengths for the mode II and mode III cases given in equation (3.2) and the following discussion, while dashed lines mark the critical elliptic radii of equation (3.13). The inner radius is not strongly dependent on the stress field parameterization.

the 2-D cases from equation (3.2), as well as the critical elliptical radii from equation (3.13) are shown in Figure 3.5 for reference. It can be seen that the radii of the inner fitting circles are coinciding roughly with the critical half length of the in-plane case.

In general, the outer radii show a larger variability within each parameter set, and an increase with decreasing Hurst exponent  $H$ . The latter reflects the transition from close to circular to more complex patch shapes due to the increase in small-scale complexity in the stress distributions.

### 3.4.4 Initiation of Rupture

After triggering by the “initial kick” of the stress increment in the triggering patch (see Appendix 3.8.1), slip velocities remain at rather low levels ( $< 0.001$  m/s) for some time during which the size of the slipping region does not change much. Eventually an exponential increase in slip velocity marks the transition to fast dynamic propagation. Figure 3.6 (top) illustrates this exponential seismic nucleation phase (moment rate  $\dot{M}_0(t) \propto \exp(s_m t)$ ) predicted by *Campillo and Ionescu* [1997] and *Ampuero et al.* [2002] and discussed in 2-D by *Ampuero and Vilotte* [2003]. The characteristic frequency  $s_m$  of this phase is a robust and observable attribute directly related to a frictional property: It is proportional to the slip weakening rate  $W$ :

$$s_m = W / \left( \frac{\mu}{2 v_S} \right) \approx 9.3 \text{ Hz.} \quad (3.6)$$

This attribute can be measured from the initial stages of the waveforms in the same way as the dominant frequency  $\omega_i$  defined by *Allen and Kanamori* [2003] or *Olson and Allen* [2005] for their early warning system strategy (Figure 3.6, bottom). The dominant frequency  $\omega_i$  at time step  $i$  of our numerical simulation can be defined by

$$\omega_i = \sqrt{\frac{A_i}{V_i}}, \quad (3.7)$$

where  $V_i$  and  $A_i$  are the squared moment rate and moment acceleration smoothed by a first-order Butterworth filter with cut-off frequency  $f^*$ . In recursive form,

$$\begin{aligned} V_i &= \alpha V_{i-1} + \left( \dot{M}_0 \right)_i^2, \\ A_i &= \alpha A_{i-1} + \left( \ddot{M}_0 \right)_i^2, \end{aligned} \quad (3.8)$$

where  $\alpha = 1 - f^* \Delta t$  and  $\Delta t$  is the time stepping interval. We take  $f^* = 1$  Hz after *Allen and Kanamori* [2003]. Shortly after slip has reached  $D_c$ , the dominant frequency reaches a maximum. As shown by the histogram in Figure 3.6 (bottom), measuring  $s_m$  as the frequency at these local maxima yields a distribution of  $s_m$  values spanning approximately 4-9 Hz with a peak around

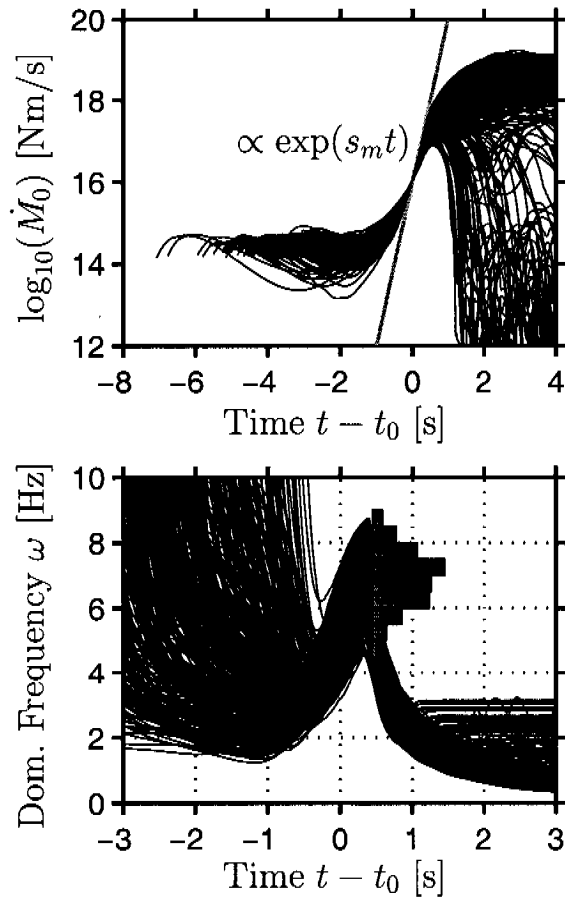


**Figure 3.6:** (top) Moment rate functions for all simulations aligned at the time  $t_0=0$  where moment rate first reaches  $10^{16}$  Nm/s. The gray line represents scaling  $\propto \exp(s_m t)$  for reference. (bottom) Dominant frequency of the moment rate functions over time. The histogram illustrates its distribution at the (local) maxima.

7 Hz. These values are lower than the value given by equation (3.6), which would be asymptotically reached for rupture sizes many times larger than the initial nucleation size. In our case, slip reaches  $D_c$  and nucleation ends before the dominant frequency has reached its asymptotic value, at slipping zone sizes of roughly 2-3 times the size of the triggering patch. According to *Favreau et al.* [2002] (in particular their Figure 10), for a quasi-elliptical slipping patch 2-3 times larger than the critical size the dominant frequency is expected to be roughly 0.6-0.7 times the asymptotic value  $s_m$ , which is in agreement with our numerical observations.

### 3.4.5 Rupture Propagation Style

One important constraint on the rupture behavior is the choice of the fixed fault size. Since the fault is surrounded by unbreakable barriers, rupture is forced to stop once it hits the fault boundaries. This imposes upper limits on the final size and seismic moment of the events, but also affects rupture propagation: If the rupture nucleates close to one of the boundaries, it will encounter the barrier much earlier on one side than on the other. This effectively leads to unidirectional, occasionally pulse-like, rupture propagation as illustrated in Figure 3.7. Crack-like propagation prevails for small events not reaching the fault borders and for large events with hypocenters at the center of the fault plane. Conceptually, the propagation style of the pulse-like events can be placed somewhere between classical cracks and self-healing slip pulses. This has been previously recognized by *Johnson* [1990] as a possible mechanism of creating the short slip rise times that have been inferred for real earthquakes [*Heaton*, 1990]. Interestingly, all seven earthquake source models cited by *Heaton* [1990] exhibit a distance of the hypocenter from the fault boundary of only about 10-30% of the total fault dimension, hence favoring unidirectional propagation. In our simulations, the width of the slipping zone (i.e., "pulse width") and the rise time of slip are still large compared to the examples given by *Heaton* [1990]. However, the largest part of pulse width and rise time is related to very slow slip velocities, so it might be difficult for waveform inversions to distinguish our pulse-like ruptures from self-healing pulses.

The hypocenter position with respect to the fault boundaries is the controlling factor regarding unidirectional or bidirectional propagation. This is in good agreement with results obtained by *McGuire et al.* [2002], who found that unidirectional propagation dominates for crustal strike-slip events and who were able to explain this observation by a model with hypocenters uniformly distributed over a fault with fixed size, comparable to our simulation setup.

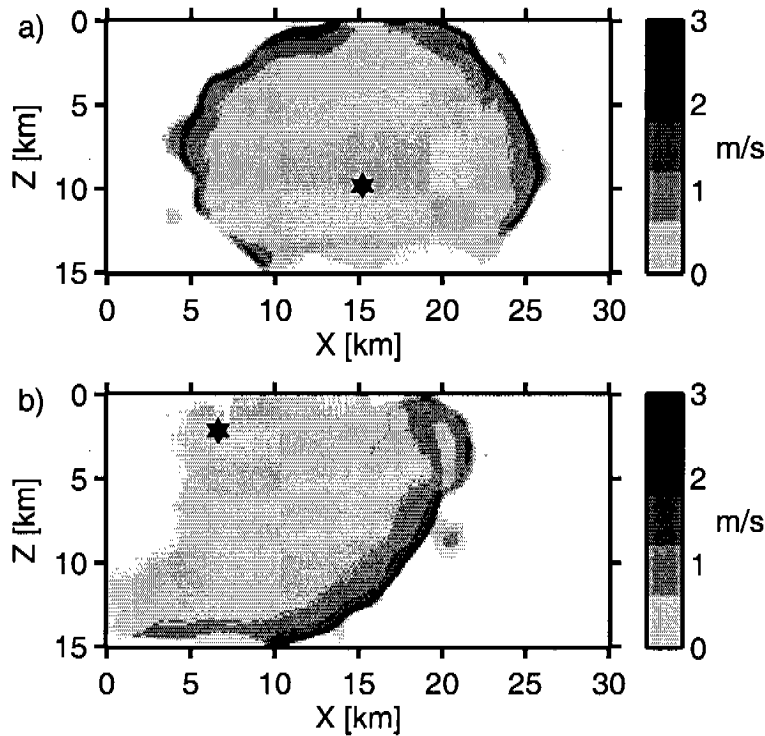


**Figure 3.7:** Snapshots of slip velocity on the fault plane for typical examples of (a) crack-like and (b) pulse-like propagation styles. Black stars indicate hypocenters; white areas are not slipping.

### 3.4.6 Stress-dependent Size Transition

For all values of the average stress level  $\bar{\tau}_0$  higher than a threshold value, the dynamic rupture cannot be stopped by the stress fluctuations and results in a system-wide event. For lower average stress levels we observe a transition to smaller event sizes. This is illustrated in Figure 3.8, where the average stress level was varied by changing the standard deviation of the initial stress distribution. On average, this transition occurs at average stress levels of 0.3, as shown in Figure 3.9, in which rupture area is plotted as a function of  $\bar{\tau}_0$  for  $H = 1$  and  $a_c = 5$  km. For other values of  $H$  we obtain similar plots, whereas for the cases with  $a_c = 33.33$  km the transition is less clearly visible, because the size of the “smaller” events below the transition is still comparable to the whole fault size. To stop propagating ruptures in our simulations the stress amplitude variations have to be so large that some areas of the fault have initial stress below the frictional strength. On real faults such areas can result from dynamic overshoot of previous events or from aseismic creep. However, this appears to be plausible only, if these areas constitute a minor fraction of the total fault area and overshoot is less than about 30 % of the total strength drop. The threshold value of  $\bar{\tau}_0 = 0.3$  translates to roughly 20 % of the fault area being below frictional strength.



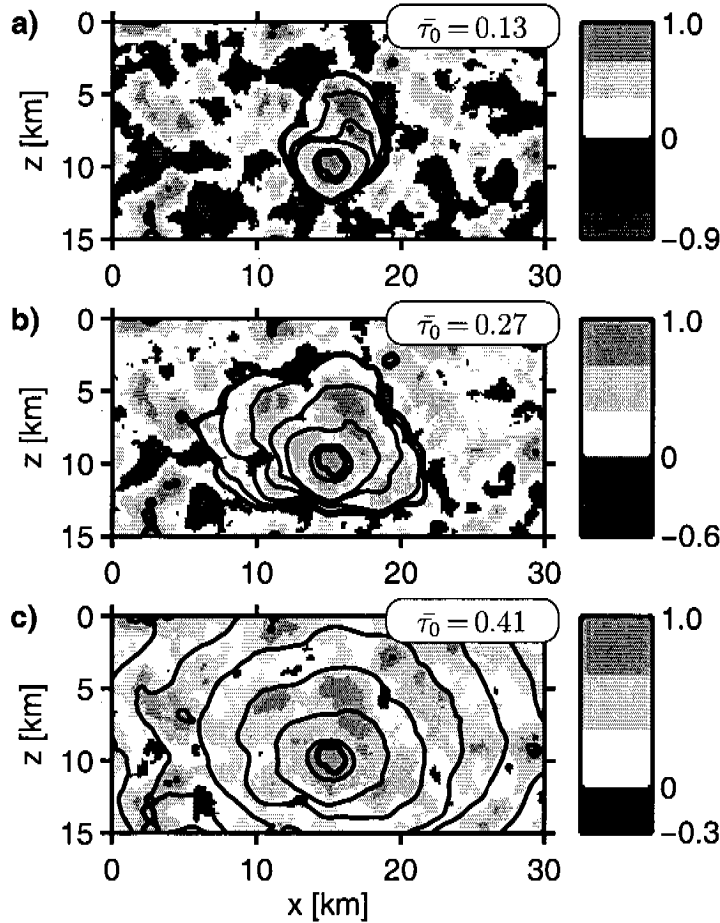


**Figure 3.8:** Contours of rupture front (black lines) plotted every second, superimposed on a gray scale map of  $(\tau_0 - \tau_d)/(\tau_s - \tau_d)$  across the fault. In these three simulations the average stress level  $\bar{\tau}_0$  was varied by using different values for the standard deviation of the initial stress ( $std = 3, 2.5$  and  $2$  MPa in Figures 3.8a, 3.8b, and 3.8c, respectively). All other parameters are the same in these three examples.

Let us explore how final event size is related to the statistical stress parameters averaged over a large ensemble of simulations. We start with an analysis of a mean stress field obtained by averaging over 10,000 random realizations, aligned at their individual maxima. This mean stress field basically consists of a single peak, the shape of which depends on the autocorrelation function of the individual random realizations. The height of the peak is determined by the standard deviation. The results for this mean field can serve as a reference for the single realizations. The results are overlain in Figure 3.9 and labeled as “mean field”. They highlight the sharpness of the transition to system-wide events.

However, not all events seem to follow the trend outlined by the reference field. A closer look reveals that near the transition additional effects like dynamic triggering and crack interaction become important. These can lead to complex

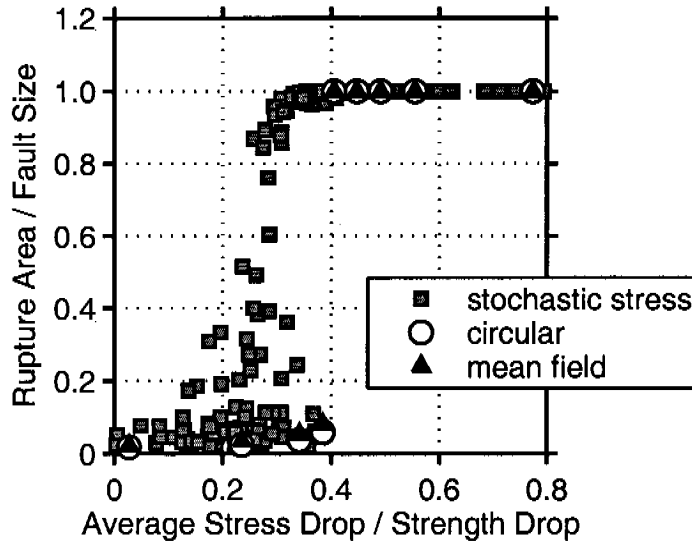


**Figure 3.9:** Ruptured area for all simulations with  $H = 1$  and  $a_c = 5$  km, plotted versus average stress level  $\bar{\tau}_0$ , which was varied by changing the standard deviation of the initial stress. Rupture area is normalized by fault size. Black triangles represent runs where the initial stress is the mean of 10,000 individual realizations, aligned at their stress maximum. For these averaged stress functions the sharp transition from small to system-wide ruptures is clearly visible. White circles indicate predictions for the mean stress fields of a simplified model assuming circular mode I cracks.

rupture patterns, disconnected slip patches and larger final rupture sizes than predicted by the mean field analysis.

Furthermore, we evaluate the rupture size predictions of a static crack model, based on expressions for circular mode I cracks (see Appendix 3.8.2). This simplified model is an extension of similar 2-D models discussed by *Ampuero et al.* [2006], who highlighted the role of the stress heterogeneity amplitude for the transition from moderate to system-wide events. The results of the current simplified 3-D model are included in Figure 3.9 (labeled “circular”). The model slightly underpredicts the rupture area below the transition but in general the transition itself is well captured.

### 3.5 Implications for Observable Macroscopic Properties

Previously, we have analyzed the properties of the dynamic rupture process using quantities that are in general only accessible in numerical simulations. However, our approach also allows us to calculate earthquake source parameters that can be inferred from seismic observations. We therefore investigate these macroscopic source parameters, computed for the large number of dy-

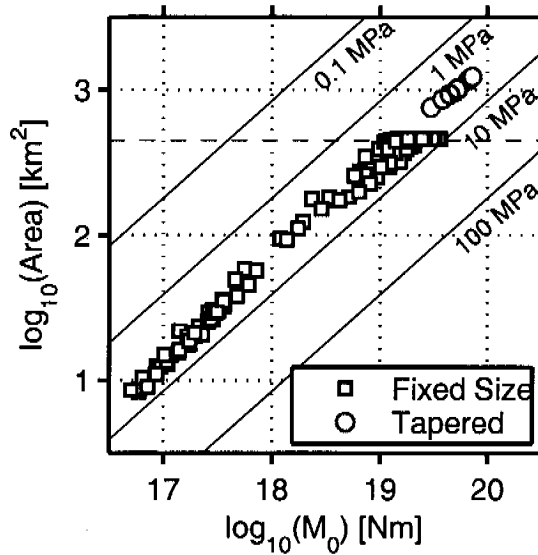


**Figure 3.10:** Plot of rupture area versus seismic moment. Note the saturation in the scaling relation at the fixed size of the fault plane at  $15 \times 30 \text{ km} = 450 \text{ km}^2$  (dashed line). A few simulations were performed on a larger fault plane (gray circles). Reference lines are drawn for a scaling of area  $\propto M_0^{2/3}$ .

dynamic rupture models and relate them to observations. For the source-scaling analysis of small and large events, recall that the model constraints on fracture energy limit the possible range of rupture behaviors and seismic radiation, decreasing in particular the generation and emission of high-frequency energy.

### 3.5.1 Seismic Moment and Radiated Energy

The events in our simulations span a range of seismic moments of roughly 2.5 orders of magnitude ( $\sim 7 \times 10^{16} - 4 \times 10^{19} \text{ Nm}$ ). Figure 3.10 displays the scaling of rupture area with seismic moment. Rupture area  $S$  here is defined as all the fault area with slip larger than 1% of the maximum slip. We observe a scaling given approximately by  $S \propto M_0^{2/3}$ , comparable to the constant stress drop scaling of observed seismicity [e.g., *Kanamori and Anderson, 1975; Wells and Coppersmith, 1994*]. At the upper end, the rupture area saturates at the fixed fault size. For a few simulations the assumption of the fixed fault size is relaxed. The fault is enlarged by 9 km in each direction (i.e., from  $15 \times 30$  to  $33 \times 48 \text{ km}$  in total) and the unbreakable boundaries are replaced by stress functions slowly decreasing (over 1.5 km) to a negative stress drop value of 10% of the total strength drop. In these cases (gray circles in Figure 3.10) the  $M_0^{2/3}$  scaling persists.

The total energy  $E_r$  radiated by the rupture process can be calculated

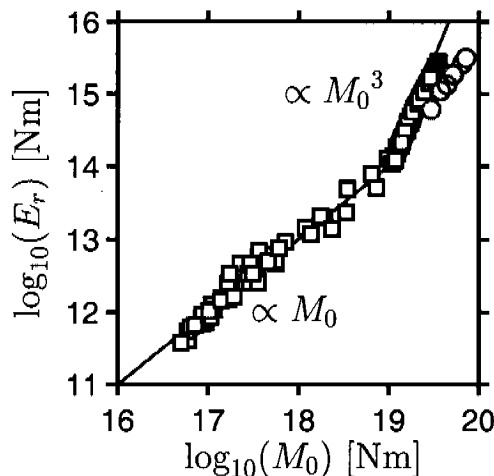


**Figure 3.11:** Scaling of radiated energy with seismic moment for all simulations with  $a_c = 5$  km. Reference lines are drawn in gray to highlight the change from  $E_r \propto M_0$  to  $E_r \propto M_0^3$  when the fixed fault size is reached at around  $M_0 = 10^{19}$  Nm. This change in scaling is partially due to enhanced radiation, when rupture is stopped abruptly at the fixed fault boundaries.

during our simulations in a straightforward manner (see Appendix 3.8.3). As can be seen in Figure 3.11, we find that radiated energy scales approximately linearly with seismic moment for all events smaller than the whole fault, thus implying constant apparent stress  $\Delta\sigma_a$  (the ratio of radiated energy to seismic moment, multiplied by the shear-modulus  $\Delta\sigma_a = \mu E_r/M_0$ ). For events spanning the entire fault, radiated energy scales roughly as  $E_r \propto M_0^3$ , which translates into strongly increasing apparent stress for increasing magnitude. This is generally not observed in real data, and is an effect of the increased radiation due to the abrupt stopping at the unbreakable boundaries (see section 3.5.2 for further discussion).

### 3.5.2 Moment Rate Spectra

From our simulations we can readily extract time histories of the total moment release rate. Some examples of moment rate functions for different events are shown in Figure 3.12. We calculate Fourier amplitude spectra of the moment rate functions which were all zero-padded to  $2^{13} = 8192$  samples to enhance frequency resolution. From the spectra we obtain their corner frequency  $f_c$  and falloff exponent  $n$  using the expression [e.g., *Abercrombie, 1995*]

$$\Omega(f) = \frac{\Omega_0}{1 + (f/f_c)^n} \quad (3.9)$$

and solving for the best fitting set of  $\Omega_0$ ,  $f_c$  and  $n$ . For  $n = 2$  this expression is the spectral shape proposed by *Brune [1970]*. Fitting is performed in a least squares sense on the logarithm values of the spectrum to reduce biasing by the

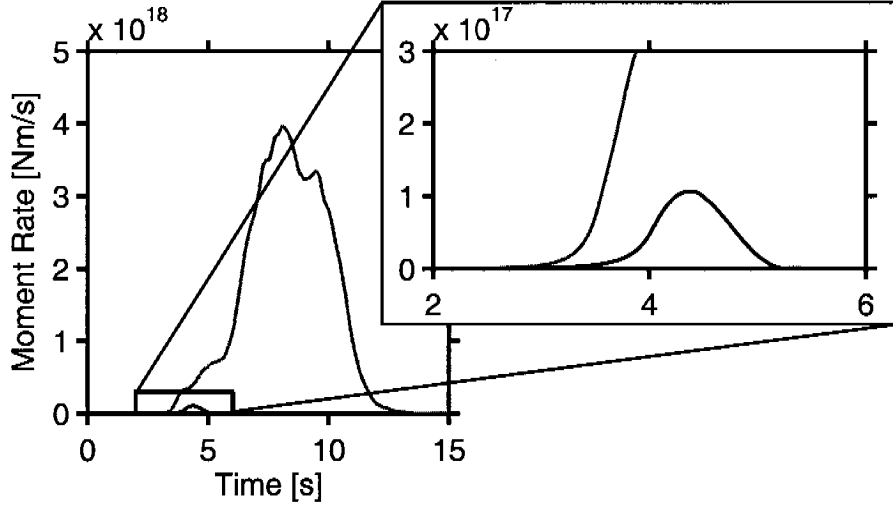


**Figure 3.12:** Typical examples of moment rate functions for one of the smallest and one of the largest events.

large values at low frequencies. The fitting range was restricted to frequencies between zero and

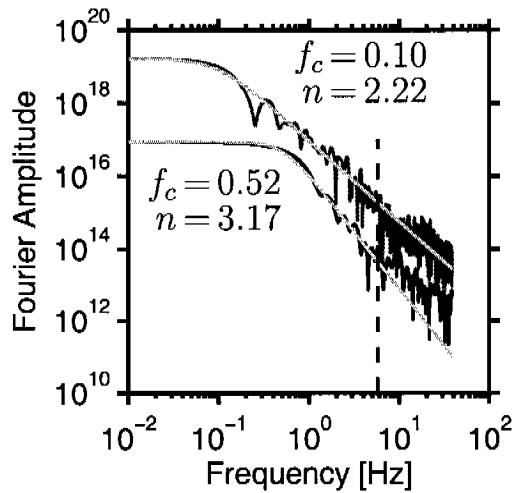
$$f_{\max} = \frac{v_s}{4\Delta x} = \frac{3464 \text{ m/s}}{4 \times 150 \text{ m}} \approx 5.77 \text{ Hz}, \quad (3.10)$$

where  $\Delta x$  is the spatial grid sampling and  $v_s$  is the shear wave velocity of the medium. Numerical noise is clearly observed in most cases for frequencies larger than 9 Hz, so we are confident that the fitting procedure is not biased by these high-frequency oscillations. Figure 3.13 shows amplitude spectra of the example moment rate functions from Figure 3.12 plus the corresponding fitted spectra.

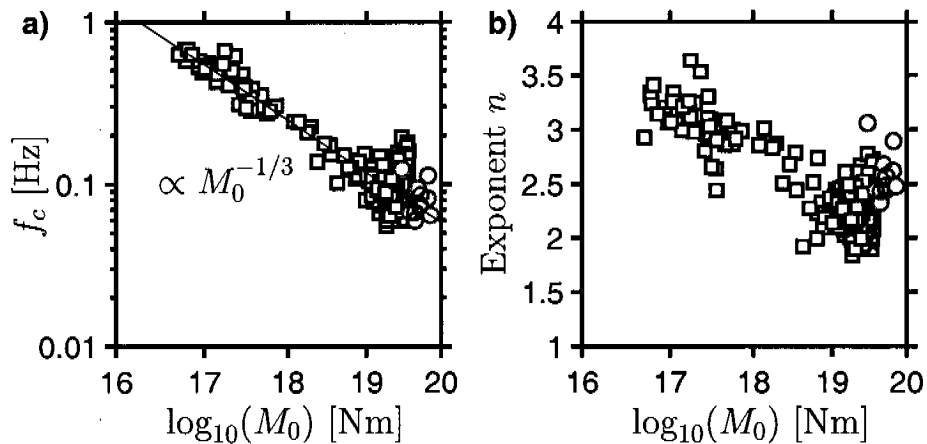
In all cases the plateau value  $\Omega_0$  of the spectrum obtained in the fitting process exactly reproduces the seismic moment  $M_0$  computed from the final slip distribution. The estimated corner frequencies for all events are plotted as a function of seismic moment in Figure 3.14a. They scale with seismic moment approximately as  $f_c \propto M_0^{-1/3}$  as expected for crack models of rupture. We cannot find a systematic deviation from this scaling for the pulse-like ruptures, in accordance with the interpretation that these events are not self-healing pulses. An alternative explanation could be, as mentioned above, that the width of the “pulse” is too large to yield a corner frequency significantly different from that of a crack-like rupture.

Figure 3.14b displays the results for the spectral falloff exponents. For all the events spanning the whole fault size, the exponent  $n$  is roughly 2-2.5. For smaller events, however, we find significantly higher exponents, clustering around  $n=3$ , corresponding to a steeper high-frequency falloff.

As pointed out by *Madariaga* [1977], high-frequency radiation is dominated by strong changes in rupture velocity and a lower bound for the spectral falloff



**Figure 3.13:** Spectra of moment rate functions for the examples in Figure 3.12. Their best fitting model spectra are overlain in light gray, along with the corresponding values of corner frequency and spectral falloff. The vertical dashed line marks the upper limit of the spectral fitting procedure of roughly 5.8 Hz.



**Figure 3.14:** Spectral parameters of moment rate functions for all simulations plotted against seismic moment: (a) Corner frequencies. They show the expected scaling with seismic moment of  $f_c \propto M_0^{-1/3}$  indicated by the black reference scaling line. (b) Spectral falloff. Note that the small events and the smoother stopping large events with stress tapered at the edges (gray circles) show falloff exponents  $n$  clearly higher than 2.

exponent is given by  $n = 2$  for sudden jumps in rupture velocity, e.g., instantaneous stopping of a crack occurring simultaneously along its front. *Madariaga* [1977] also notes that for abrupt, but not simultaneous stopping, the exponent  $n$  will become higher. In addition, *Dahlen* [1974] considered a crack model including self-similar nucleation and smooth stopping for which he derived a high-frequency asymptotic limit with  $n = 3$ .

These findings offer a consistent explanation for the different spectral falloffs of our simulated ruptures. Nucleation in our model is similar for small and large events and it is a slow and smooth process, not expected to generate significant high-frequency radiation. The small events are strongly affected by our simplistic assumption of constant fracture energy. Their fracture energy is relatively high compared to the energy available to drive the rupture and the events are therefore characterized by unusually low average rupture velocities of roughly 20% of the shear wave velocity. In addition, they stop early and smoothly by propagating into regions of the fault with low initial stress. Thus, overall the small events experience no strong changes in rupture velocity and little high-frequency radiation is excited. In contrast, the large events accelerate to higher average rupture velocities before they are abruptly stopped by hitting the unbreakable boundaries, exciting strong stopping phases that increase the high-frequency radiation.

We have repeated a number of simulations in which the unbreakable boundaries are replaced by a slowly decaying stress field. These tapered stress fields also stop the ruptures, but over a broader zone and thus more gently. Compared to their untapered counterparts, these events show increased spectral exponents of 2.5-3 (gray circles in Figure 3.14b). This confirms that a large part of the high-frequency radiation in our dynamic simulations originates from abrupt stopping of the ruptures at the fault boundaries.

In addition, the larger ruptures might generate radiation by repeated acceleration and deceleration due to the heterogeneity in initial stress. However, we do not observe systematic changes of the exponent  $n$  with the parameters describing the stress distribution. Probably because most of the ruptures hit the unbreakable boundaries and the resulting stopping phases mask differences in radiation during propagation.

Also, the abrupt fluctuations of rupture velocity required for sustained high-frequency radiation ( $n = 2$ ) are less efficiently generated by stress heterogeneities than by heterogeneities of fracture energy, which are not included here. The reason is that, whereas  $G_c$  enters the "crack tip equation of motion" by its local value, stress drop contributes as a weighted spatial average through the integral defining the stress intensity factor. More singular stress distributions than the ones considered here, such as stress concentrations at the edges of previous events, might be required to generate high-frequency radiation [*Madariaga*, 1983].

### 3.5.3 Hypocenter Location and Slip Distribution

In general, the distributions of final slip in our simulations reflect the heterogeneity of the initial shear stress. In particular, stress fields with high Hurst exponent, long correlation length and small standard deviation yield “smoother” distributions, while “roughness” of slip increases with lower Hurst exponent, shorter correlation length and larger standard deviation of stress. All events not reaching the fault boundaries consist of a single slip patch with the hypocenter located within the region of highest slip (i.e., within the zone of slip  $d$  larger than  $2/3$  of the maximum slip  $d_{\max}$ ), often directly coinciding with the location of  $d_{\max}$ . For the larger events the artificially imposed fault boundaries become important. If ruptures nucleate in the central part of the fault (more than 5 km distance from any boundary), the hypocenters are still close to the region of highest slip and in more than 95 % of the events hypocentral slip is larger than  $2/3 d_{\max}$ . In contrast, hypocenters located very close to the boundaries (distance to boundary  $< 2$  km) are in general more remote from the location of largest slip and only  $\sim 7\%$  of these events have hypocentral slip  $d > 2/3 d_{\max}$ . However, for most of these events hypocentral slip is still large (88 % have  $1/3 d_{\max} < d < 2/3 d_{\max}$ ). So overall the stress load determined hypocenter positions in our simulations are compatible with the hypocenter locations in imaged finite source rupture models [Mai *et al.*, 2005], where it is found that hypocenters are located within or close to regions of large slip.

## 3.6 Discussion

Let us investigate how our numerical simulations compare against analytical predictions and observations of real earthquakes.

### 3.6.1 Nucleation

In this study we have assumed that linear slip-weakening friction is also the governing process during quasi-static nucleation. Our results on nucleation agree well with and extend earlier studies based on the same assumption [e.g., Campillo and Ionescu, 1997; Favreau *et al.*, 2002; Uenishi and Rice, 2003; Ampuero and Vilotte, 2003]. In particular the common length scale of the nucleation zone (section 3.4.3) and the exponential growth during the nucleation phase (section 3.4.4) match well the expectation.

Olson and Allen [2005] observed a magnitude dependency of the dominant frequency measured from the first three seconds of seismograms, which cannot be explained by our assumed constant  $W$ . It may require a power law nonlinear slip-weakening model [Cochard *et al.*, 2006] or a fault with heterogeneous  $D_c$  where larger events show some tendency to nucleate in regions of longer critical slip distance (as defined in rate-and-state friction models [Hillers *et al.*, 2006,



Figure 14]).

### 3.6.2 Rupture Arrest

We find that the average final sizes of the ruptures are predicted reasonably well by a simplified model based on fracture mechanical considerations of circular mode I cracks (section 3.4.6 and Appendix 3.8.2), constituting a three-dimensional extension of the 2-D model by *Ampuero et al.* [2006]. This simplified model may serve as a guide in choosing stress parameterizations for future scenario calculations, e.g., for a given target event size.

### 3.6.3 Fracture Energy

In our present approach, both strength drop and  $D_c$  are constant and hence fracture energy (i.e., the energy dissipated at the tip of the rupture) is also uniform across the fault plane and independent of rupture size. However, several studies have indicated a scale dependence of fracture energy [e.g., *Ohnaka*, 2003; *McGarr et al.*, 2004; *Mai et al.*, 2006]. Though the origin and the details of this scale dependence are still a subject of ongoing debate, it is clear that the assumption of homogeneous fracture energy is a strong simplification. We consider it justified from the viewpoint that an integral aspect of our work is to explore and demonstrate ways of dealing with stochastic descriptions of stress in a generic sense and to estimate the first-order response of a complex system. The simulations presented in this paper should thus be understood as a starting point for more refined and complex modeling to be guided by and to be built on the current results.

Several ways of including scale-dependent fracture into numerical simulations have been suggested: *Aochi and Ide* [2004] proposed a renormalization approach, while *Andrews* [2005] demonstrated that the scale-dependent nonelastic behavior off the fault plane can be mimicked by simply limiting the slip velocity in an elastic medium. Other ways to include scale-dependent fracture energy in our simulations could be a parameterization of  $D_c$  depending on hypocentral distance and/or stress heterogeneity or the use of a slip-weakening friction law in which strength continues to drop as a small power of slip as suggested by *Abercrombie and Rice* [2005].

We expect the following changes to our results for scale dependent fracture energy. The rupture velocity and the seismic radiation properties of the smaller events will better match observational data. Moreover, we expect it to become easier for ruptures to stop with smaller amplitude variations in initial stress and fewer areas (or none) of initial stress below  $\tau_d$ .

Finally we would like to point out that including systematic scale dependencies of  $G_c$  into the analysis of Appendix 3.8.2 is straightforward. The scale dependencies discussed in recent literature [e.g., *Abercrombie and Rice*, 2005;

*Andrews*, 2005] would yield a transition in event size similar to the one described above, but at a different average stress level (see Appendix 3.8.2).

### 3.6.4 Slip Pulses

*Heaton* [1990] pointed out that in many source inversions of real earthquakes slip rise times have to be significantly shorter than the overall event duration to obtain an acceptable fit to the recorded seismograms. As an explanation, *Heaton* [1990] proposed a model in which velocity-weakening friction results in self-healing pulses of slip propagating over the rupture plane. As discussed in section 3.4.5, despite crack-like rupture propagation modes are prevailing in our simulations, some of the events show pulse-like features resulting from nucleation close to the fault boundaries. Assuming that because of their limited resolution, waveform inversions might not be able to distinguish between these pulse-like ruptures and self-healing pulses, this mechanism could offer an alternative explanation for the short rise times of slip inferred for real earthquakes. Alternatively, extending our current model with some healing mechanism is expected to enhance the generation of rupture pulses, probably with even shorter rise times.

### 3.6.5 High-Frequency Radiation

Our results on the spectral falloff underline the importance of the stopping of earthquake ruptures. Do they just slow down gently, or come to a halt abruptly? Our simulations document how these different mechanisms lead to variations in the high-frequency falloff. The spectral falloff with  $n = 3$  of the smallest simulated events is generally not observed for real earthquakes in this magnitude range, but is probably a result of the assumed scale independence of fracture energy. However, this case (fracture energy being large compared to the strain energy driving the rupture) may in some cases occur at a much lower magnitude level. Studies on microearthquakes recorded at borehole stations do indeed show a certain variability in the spectral falloff exponents. *Abercrombie* [1995] states that  $n = 2$  represents a good average, but also notes that the individual falloff exponents show a significant scatter up to around  $n = 3.5$ . A similar range of values for  $n$  was reported by *Venkataraman et al.* [2006]. In one area they even found a systematic increase in falloff exponents with decreasing event size.

### 3.6.6 Fault Boundary

In general, all our simulated events yield macroscopic rupture properties in a physically reasonable range. However, the scaling relations of these proper-

ties are only compatible with observational data for events smaller than the whole fault size. For the whole fault events the unbreakable fault boundary has been shown to strongly affect the scaling of area, moment and radiated energy. Hence replacing this strong discontinuity in strength by a more gradual change will improve the match of observed scaling relations.

### 3.6.7 Plausible Stress Characterization

For stress distributions with the lowest standard deviation ( $std/(\tau_s - \tau_d) \approx 0.1$ ) we always obtain whole fault events with supershear rupture propagation over much of the fault plane. Such an abundance of supershear propagation is not observed in real earthquakes, rendering these stress models implausible in conjunction with the assumption of homogeneous fracture energy. If fracture energy is heterogeneous, however, a stress distribution with small-amplitude variations or even homogeneous stress also can produce globally subshear ruptures, as demonstrated by *Ide and Aochi* [2005]. On the other hand, extremely high values of the standard deviation ( $std/(\tau_s - \tau_d) > 0.4$ ) always lead to the rupture of a single high-stress patch, not being able to propagate to a neighboring patch. These single asperity ruptures generate a single isolated slip patch, not comparable to many of the imaged slip distributions of large earthquakes. Our results therefore suggest that (at least in the simplistic case of homogeneous fracture energy) a standard deviation of stress in the intermediate range is most plausible. As shown in section 3.4.6, the most complex rupture behavior (including dynamic triggering and rupture jumping) is observed close to the stress-dependent transition in event size.

The stress distributions with correlation length on the order of the total fault dimension also yield slip distributions with a single high-slip patch only. Therefore correlation lengths substantially smaller than the fault size are needed to generate the complexity in imaged slip distributions with multiple high-slip patches [e.g., *Mai and Beroza*, 2002].

## 3.7 Conclusions

We have investigated the effects of correlated random initial stress on dynamic earthquake rupture. This work establishes links between statistical properties of these stress fields, the governing friction law on the fault and macroscopic rupture properties. Although the details of the actual stress field on a real fault are not accessible to direct measurement, its statistical properties might be reasonably well estimated. Our results provide insights into how these statistical characterizations of fault stress affect the overall rupture behavior and seismic observables. In this context, not only the average macroscopic rupture properties, but also their variability, will be important input to scenario calculations for improved seismic hazard estimates in the near-fault region.

## 3.8 Appendix

### 3.8.1 Approximation of Tectonic Loading

As noted in section 3.2.2, we approximate tectonic loading and quasi-static nucleation by an iterative procedure. We start with a heterogeneous stress distribution  $\tau(x, z)$ , where the maximum of the stress distribution has just reached the static yield level  $\tau_s$  of the material. The main task is to find the critical load  $\Delta\tau_c^\infty$ , which is the amount of tectonic stress increase  $\Delta\tau^\infty$  necessary to bring the fault to the critical stress state at the onset of dynamic instability. Our method of finding  $\Delta\tau_c^\infty$  consists of the following steps:

1. A starting value for  $\Delta\tau^\infty$  is chosen.
2. The set of grid points is determined for which the original stress  $\tau(x, z)$  plus the tectonic load exceeds the static yield stress level of the material; that is, we find all grid coordinates  $x, z$  for which  $\tau(x, z) + \Delta\tau^\infty \geq \tau_s$ .
3. Within the set of grid points found in step 2 we search for connected clusters of points. Two grid points are defined as connected if they are direct neighbors either in the  $x$  or  $z$  directions. The largest cluster is defined as the one containing the most grid points and will be termed the “triggering patch”. At all points belonging to the triggering patch, shear stress will be set to a small value  $\tau_{\text{trig}}$  above the yield stress to initiate rupture in the dynamic simulation. The value of  $\tau_{\text{trig}}$  should be sufficiently small to still be in accord with the notion of nucleation originating from quasi-statically growing slipping zones. On the other hand it does not have to be smaller than daily variations of stress superimposed on the tectonic load, where Coulomb stresses from Earth tides can be of the order of a few kPa [Cochran *et al.*, 2004]. Still, the choice of  $\tau_{\text{trig}}$  is somewhat arbitrary and we have experimented with different values between 0.1 and 10 kPa. Since results only varied slightly, we have chosen  $\tau_{\text{trig}} = 10$  kPa for all the results presented in this paper.
4. To avoid simultaneous triggering at multiple locations, stress is set to a small value  $\tau_{\text{reduce}}$  below yield stress at all remaining points found in step 2 which do not belong to the triggering patch. Since preslip at those points is expected to be small, stress should not have dropped very much at those points and we use a value of  $\tau_{\text{reduce}} = 10$  kPa for all our simulations. However, we do not expect a strong influence for variations of this value.
5. We carry out a dynamic simulation with the resulting shear stress. To save computation time, the simulation is restricted to a small subsection

(9 km  $\times$  9 km) of the fault surrounding the triggering patch and to  $\sim 5$  s simulated time. After this duration, in all our simulations either slip has stopped completely on the whole fault or a slip velocity threshold of 0.001 m/s has been exceeded, indicating continued rupture expansion.

6. If slip velocity during this simulation has not reached the threshold value of 0.001 m/s, we start over at step 1 with an increased value of  $\Delta\tau^\infty$ . If the slip velocity threshold has been exceeded, we start over at step 1 with a decreased value of  $\Delta\tau^\infty$ .

Employing this procedure iteratively, we finally obtain the smallest load that still leads to sustained rupture, i.e., an approximated value of the critical load  $\Delta\tau_c^\infty$ . Using this critical load, we go through steps 2-4 of the above procedure to obtain the critical state of the stress field. This stress distribution is used as the initial stress  $\tau_0(x, z)$  in the dynamic rupture computation on the entire fault. Rupture in this whole fault dynamic simulation is triggered by the small increment  $\tau_{\text{trig}}$  above yield stress inside the triggering patch.

We test the scheme described above, first for one of the 3-D cases treated analytically by *Uenishi and Rice* [2004]. The stress function is pure shear in the in-plane direction ( $x$ ) and is given by

$$\tau(x, z) = \tau_s - \frac{1}{2} \left[ x^2 + \left( \frac{1}{1-\nu} \right)^2 z^2 \right]. \quad (3.11)$$

According to *Uenishi and Rice* [2004], for homogeneous loading of this stress function, the slipping patch always has an elliptical shape with constant aspect ratio. For  $\nu = 0.25$  they provide the following approximate values of the critical elliptical radii  $a_e$  and  $b_e$ :

$$\begin{aligned} 2a_e &\approx 2.598 \frac{\mu}{W}, \\ 2b_e &\approx 1.951 \frac{\mu}{W}, \end{aligned} \quad (3.12)$$

Applying our loading procedure (with grid spacing  $\Delta x = 150$  m and triggering stress  $\tau_{\text{trig}} = 10$  kPa) to this stress function, we compare the obtained results with the theoretical prediction, as shown in Figure 3.15. The size of the triggering patch is smaller than predicted (elliptical radii of approximately  $0.8a_e$  and  $0.8b_e$ ), whereas the critical load  $\Delta\tau_c^\infty$  is overestimated by a factor of about 2. This is due to the fact that our approximation neglects the effect of quasi-static preslip. Stress starts to decrease at the location of this quasi-static preslip, but at the same time stress is increased in the surrounding regions, effectively leading to earlier nucleation (i.e., with less loading necessary). If successively smaller increments  $\tau_{\text{trig}}$  inside the triggering patch are used, its size tends asymptotically toward the theoretical prediction, but the overestimation of the critical load is increased. So in choosing the triggering stress  $\tau_{\text{trig}}$  there is a trade-off between the errors of the approximation of nucleation

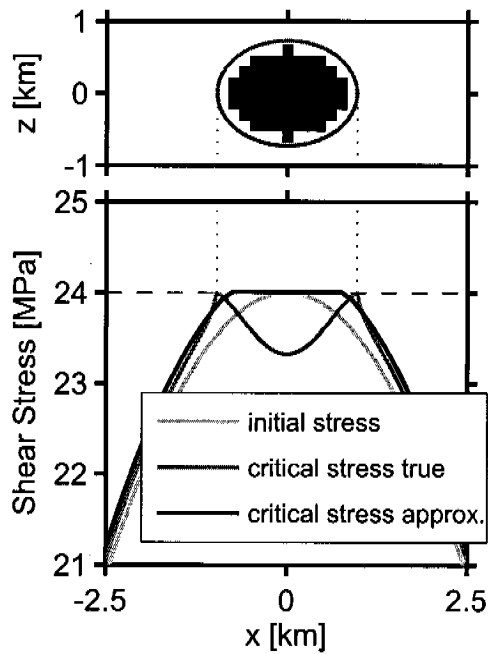


**Figure 3.15:** (top) Triggering patch (black) obtained through the approximative loading procedure for the stress function of equation (3.11) compared to the theoretical prediction (dark gray ellipse) for a grid spacing of 150 m. (bottom) Stress profiles along the in-plane direction. Shown are the initial stress (light gray), the correct critical stress state including the drop of stress in the center due to quasi-static preslip (dark gray) and the approximation of the critical stress state (black). Dotted lines indicate theoretical 3-D nucleation length. Horizontal dashed line indicates yield strength.

size and critical load.

As mentioned in section 3.2.2 we have developed an improved algorithm (to be presented in a forthcoming paper) to compute the critical load. This enabled us to perform a similar comparison also for the heterogeneous stress distributions, where no analytical solution is available. We find that the critical load is overestimated by our approximation procedure by factors ranging from 1.4 to 1.8 with an average of 1.6. This affects the ratio between stress standard deviation  $std$  and average stress level  $\bar{\tau}_0$  and therefore the values in Figure 3.4 are slightly shifted upward with respect to their true value. However, the scaling relation of the critical load given by equation (3.5) remains valid, as do the general results obtained in this paper.

### 3.8.2 Analysis of the Transition to Runaway Ruptures

We propose here a mechanical interpretation of the transition from small to fault-wide earthquake sizes illustrated in Figures 3.8 and 3.9. This explanation is based on fracture mechanics concepts and is largely inspired by the work of *Dyskin* [1999]. It extends the discussion presented by *Ampuero et al.* [2006] to 3-D cases. A number of approximations are made that are ultimately tested by comparison to the average properties of our dynamic simulations (Figure 3.9). The evolution of a slip-weakening crack with a relatively small process zone can be fairly well described by the Griffith criterion and small-scale-yielding fracture mechanics. Upon arrest, the dynamic stress intensity factor  $K$  shows damped oscillations around its static value, generated by multiple wave diffractions along the rupture front. In a rough approximation, the final earthquake size is given by the following arrest criterion (e.g., in the mode II direction):

$$\frac{1-\nu}{2\mu} K_0^2 = G_c \quad (3.13)$$

where  $K_0$  is the static stress intensity factor and fracture energy is given by  $G_c = (\tau_s - \tau_d) D_c/2$ . Realistic rupture fronts have complicated geometry, but for the sake of mathematical tractability we employ the expression of  $K_0$  for circular mode I cracks. This approximation is justified by our interest in statistically averaged properties arising from isotropic stress drop distributions, and by considering the anisotropy of the shear modes as a second-order effect. For a crack of radius  $a$  and a heterogeneous stress drop  $\Delta\tau$ , it is given in cylindrical coordinates  $(r, \theta)$  by *Lai et al.* [2002], after *Fabrikant* [1989], as

$$K_0(a, \theta) = \frac{1}{\pi\sqrt{\pi a}} \int_0^{2\pi} \int_0^a \frac{\Delta\tau(r, \phi) \sqrt{a^2 - r^2}}{a^2 + r^2 - 2ar \cos(\theta - \phi)} r dr d\phi. \quad (3.14)$$

Clearly,  $K_0$  fluctuates along the crack rim, but we will assume that the arrest condition can be applied to the average stress intensity factor

$$K_0(a) = \frac{1}{2\pi} \int_0^{2\pi} K(\theta) d\theta, \quad (3.15)$$

which can be simplified to:

$$K_0(a) = \frac{1}{\pi\sqrt{\pi a}} \int_0^{2\pi} \int_0^a \frac{\Delta\tau(r, \phi)}{\sqrt{a^2 - r^2}} r dr d\phi. \quad (3.16)$$

To estimate the average event-size we first compute  $K_0(a)$  by numerical integration of equation (3.16) with an ensemble-averaged  $\Delta\tau(\rho, \theta)$  obtained by averaging 10,000 realizations of the stress field aligned on their nucleation point (or, approximately, on their maxima). We then apply the arrest criterion (3.13) to estimate the final radius  $a$ . Figure 3.9 shows a satisfactory comparison between this approach (open circles), the dynamic simulations based on the ensemble-averaged stress (black triangles) and the average trends of the dynamic simulations based on individual realizations of the stress field. In the remainder of this appendix we quantify analytically the conditions for the earthquake size transition.

A crack that has grown considerably larger than the correlation length of the heterogeneous stress field can be modeled by a crack subjected to uniform loading by the average stress drop  $\langle\Delta\tau\rangle$  plus a pair of concentrated forces  $F$  representing the excess of stress drop in the nucleation area. We can obtain  $F$  numerically from our ensemble-averaged stress field (average of 10,000 realizations, aligned at maxima) as

$$F = \iint (\Delta\tau - \langle\Delta\tau\rangle) dS. \quad (3.17)$$

Alternatively, if we assume  $a_c \gg a_\nu$ , the shape of the mean stress field can be approximated by the autocorrelation function of stress  $C$ , normalized by  $std^2$ , and we can write:

$$F = (\Delta\tau(0) - \langle\Delta\tau\rangle) \iint C(x, z) dS, \quad (3.18)$$

where  $\Delta\tau(0)$  is the stress drop at the hypocenter. Defining the integral above as  $c(H) a_c^2$ , with  $c(H)$  being dimensionless, and again using  $a_c \gg a_\nu$  to assume  $\Delta\tau(0) \approx \tau_s - \tau_d$ , we can write

$$F = (\tau_s - \tau_d - \langle\Delta\tau\rangle) c(H) a_c^2. \quad (3.19)$$

For the circular mode I crack with radius  $a$  the average stress intensity factor resulting from  $F$  and  $\langle\Delta\tau\rangle$  is:

$$K_0 = \frac{F}{(\pi a)^{3/2}} + 2 \langle\Delta\tau\rangle \sqrt{\frac{a}{\pi}} \quad (3.20)$$

The two terms in (3.20) have competing contributions, the first decreases whereas the second increases as a function of  $a$ . We find that  $K_0$  reaches a minimum

$$K_{\min} = 8 \cdot \left( \frac{F \langle\Delta\tau\rangle^3}{2(3\pi)^3} \right)^{1/4}, \quad (3.21)$$



at the radius

$$a_{\min} = \sqrt{\frac{3F}{2\pi \langle \Delta\tau \rangle}}. \quad (3.22)$$

For a stable equilibrium crack to exist we need

$$K_{\min} \leq K_c = \sqrt{2\mu G_c / (1 - \nu)}, \quad (3.23)$$

which yields the following condition:

$$F \langle \Delta\tau \rangle^3 \leq \frac{(3\pi)^3}{2^{11}} K_c^4 \approx 0.41 K_c^4 \quad (3.24)$$

Combining with (3.19) the condition above can be written in terms of  $\langle \Delta\tau \rangle$  as

$$(\tau_s - \tau_d - \langle \Delta\tau \rangle) \langle \Delta\tau \rangle^3 \leq \frac{(3\pi)^3}{2^{11}} \frac{K_c^4}{c(H) a_c^2}. \quad (3.25)$$

When (3.25) is violated the fault tends to generate runaway ruptures. Introducing the nucleation half length of an in-plane rupture

$$a_\nu = \frac{1.158}{2} \frac{\mu}{1 - \nu} \frac{D_c}{\tau_s - \tau_d}, \quad (3.26)$$

it can then be shown that the critical  $\langle \Delta\tau \rangle_c$  and  $a_{\min}$  are given by

$$\langle \Delta\tau \rangle_c \approx (\tau_s - \tau_d) \left[ \frac{(3\pi)^3}{2^9 1.158^2 c(H)} \frac{a_\nu^2}{a_c^2} \right]^{1/3} \quad (3.27)$$

and

$$a_{\min,c} \approx \frac{2}{\pi} a_c \left[ \frac{1.158 c(H)^2 a_c}{a_\nu} \right]^{1/3}, \quad (3.28)$$

respectively. Considering the amount of simplifying assumptions involved in the derivations above, these estimates are in fair agreement with the results of our dynamic simulations.

If fracture energy scales with crack size as  $G_c \approx G_c^0 + \gamma a$ , it can be shown, by similar arguments to those above, that a sharp transition to runaway rupture exists at average stresses of order  $\sqrt{(\pi\mu\gamma)/(2(1-\nu))}$ , which can be higher than in the constant  $G_c$  case.

### 3.8.3 Estimation of Radiated Energy

As shown by *Kostrov* [1974] and recently summarized by *Rivera and Kanamori* [2005], the radiated energy  $E_r$  can be expressed through surface integrals over the fault plane:

$$E_r = \frac{1}{2} \int_{\Sigma} (\tau_{ij}^1 - \tau_{ij}^0) \Delta u_i \nu_j dS - \int_{\Sigma} 2\gamma_{\text{eff}} dS - \int_{t_0}^{t_1} dt \int_{\Sigma(t)} (\tau_{ij} - \tau_{ij}^0) \Delta \dot{u}_i \nu_j dS. \quad (3.29)$$

Here,  $\Sigma$  is the fault plane and  $\Sigma(t)$  is the ruptured fault surface at time  $t$  up to the trailing edge of the process zone. The unit normal vector to the fault plane is  $\nu_j$ . Initial and final stress states are denoted by  $\tau_{ij}^0$  and  $\tau_{ij}^1$ , respectively; and  $\Delta u$  and  $\Delta \dot{u}$  are slip and slip velocity. The effective fracture energy is  $\gamma_{\text{eff}}$  and  $t_0$  and  $t_1$  are times before and after the earthquake.

Since the slip velocity  $\Delta \dot{u}$  is zero outside the currently rupturing zone  $\Sigma(t)$ , we can evaluate the last integral over the whole fault plane. By doing this, we also include the process zone and thus the second term in equation (3.29). So what we are actually evaluating is the following equation:

$$E_r = \frac{1}{2} \int_{\Sigma} (\tau_{ij}^1 - \tau_{ij}^0) \Delta u_i \nu_j dS - \int_{t_0}^{t_1} dt \int_{\Sigma} (\tau_{ij} - \tau_{ij}^0) \Delta \dot{u}_i \nu_j dS. \quad (3.30)$$

This form is more convenient for numerical evaluation than the one proposed by *Favreau and Archuleta* [2003], which is obtained from 3.30 by integration by parts of the second term. Because we are only simulating pure strike-slip events, we further neglect the down dip slip components. We therefore obtain the following simplified expression for  $E_r$ , which can be conveniently evaluated numerically from the quantities available during our simulations:

$$E_r = \frac{1}{2} \iint_{x,z} (\tau^1 - \tau^0) \Delta u^1 dx dz - \int_t dt \iint_{x,z} (\tau - \tau^0) \Delta \dot{u} dx dz. \quad (3.31)$$

## Acknowledgments

We thank S. Ide and R. Archuleta for their detailed and constructive reviews. They also provided challenging comments, some of which require future improvements and research beyond the present paper. We also wish to thank the Associate Editor J. Townend for carefully inspecting the manuscript and providing additional suggestions for improvement. We thank E. Dunham for providing us his spectral boundary integral code ‘‘MDSBI’’. J.-P. Ampuero is supported by SPICE, a Marie Curie Research Training Network in the 6th Framework Program of the European Commission. This is contribution No. 1448 of the Institute of Geophysics, ETH Zurich.



## Chapter 4

# Near-Field Ground Motion from Dynamic Earthquake Rupture Simulations

J. Ripperger, P. M. Mai and J.-P. Ampuero

Submitted to Bulletin of the Seismological Society of America as:  
Ripperger, J., P. M. Mai, and J.-P. Ampuero, Near-field ground motion from  
dynamic earthquake rupture simulations.

## Abstract

This study investigates the near-field ground motion resulting from dynamic rupture models with heterogeneity in the initial shear stress parameterized in a stochastic manner. The ground velocity seismograms are synthesized by convolving the time histories of slip velocity obtained from spontaneous dynamic rupture models with Green's functions of the medium response calculated with a discrete wavenumber / finite element method. Peak ground velocity (PGV) estimated on the synthetics generally matches well with an empirically derived attenuation relation, whereas spectral acceleration (SA) only shows an acceptable match at periods longer than 1 s. Usage of the geometric mean to average the two orthogonal components leads to a systematic bias for the synthetics, in particular at the stations closest to the fault. This bias is avoided by using measures of ground motion that are independent of the sensor orientation.

The contribution from stress heterogeneity to the overall ground motion variability is found to be strongest close to the fault and in the backward directivity region of unilaterally propagating ruptures. In general, the intra-event variability originating from the radiation pattern and the effect of directivity is on the same order or larger than the inter-event variability. The inter-event ground-motion variability itself originates to a large extent from the hypocenter-station configuration and to a lesser extent from the differences in the dynamic rupture process due to the stress heterogeneity.

Compared to the peak ground motion recorded during the 2004 Parkfield, California earthquake our simulated seismograms show enhanced spatial correlation which may be attributed to the simplicity of the assumed crustal model. Nevertheless, the intra-event PGV variability in the near-fault region determined for the Parkfield dataset is of the same order of magnitude as for our simulations.

## 4.1 Introduction

Recent, well instrumented earthquakes generated a large number of ground motion recordings from sites close to the active fault (e.g., 1999 Chi-Chi, Taiwan, 2000 Tottori, Japan and 2004 Parkfield, California). In these datasets, the observed variability of ground motion intensity measures such as peak ground acceleration (PGA) or peak ground velocity (PGV) in the near-field is large [e.g., *Shakal et al.*, 2006]. This variability potentially originates from differences in the local site conditions close to the recording stations, from varying path effects such as focusing or scattering of the seismic waves and finally from properties of the seismic source itself. This contribution of earthquake source complexity to the ground-motion variability is generally thought to be significant, especially in the region of less than one or two fault lengths distance.

Early studies on near-source ground motion employed simple theoretical and

numerical models to understand its first order characteristics [e.g., *Aki*, 1968; *Haskell*, 1969; *Archuleta and Frazier*, 1978]. With increasing computational power and larger number of recordings available, many studies have inverted observed data to construct models of the source process (For a collection of inverted source models see *Mai* [2004]). These models are kinematic, i. e. they provide a spatio-temporal distribution of the displacements taking place on an earthquake fault that is compatible with the observed ground motion, but not necessarily obeys the physical principles of rock fracturing. In contrast, dynamic models attempt to simulate the physical rupture process and the frictional sliding of the rock interfaces past each other. They are typically controlled by initial conditions and a constitutive law relating displacements and stresses on the fault plane. They have been successfully used to model ground motion of recent earthquakes [e.g., *Olsen et al.*, 1997; *Peyrat and Olsen*, 2004]. Each of these source inversions, kinematic or dynamic, provides an image of the rupture process of one particular past event.

To estimate seismic hazard in a given region it is required to anticipate the ground motion due to a future earthquake. To this end, scenario simulations have been performed [e.g., *Graves*, 1998; *Graves and Pitarka*, 2004; *Olsen et al.*, 2006] to evaluate ground shaking for specific regions. Only a few studies systematically investigated the influence of different source parameters on the resulting near-source ground motion [e.g., *Inoue and Miyatake*, 1998; *Aagaard et al.*, 2001, 2004] and even less attempt to quantify the uncertainty in the employed source parameters and the associated variability in ground motion. One way to account for the uncertainty in the initial conditions is to parameterize one or more input variables in a stochastic sense [e.g., *Oglesby and Day*, 2002], perform an ensemble of statistically similar simulations and evaluate the average prediction and its variability. This approach is expected to play an increasingly important role, in particular due to the advance in computing capabilities [e.g., *Olsen et al.*, 2006].

Recent studies by *Ampuero et al.* [2006] and *Ripperger et al.* [2007] explored the stochastic parameterization of initial shear stress for simulations of dynamic earthquake rupture. These papers mainly investigated the modeled rupture process on the fault plane, but since the approach ultimately aims at improving seismic hazard assessment, it is mandatory to verify the ground motions predicted by these simulations against observations.

Rather than trying to model particular seismograms of an individual event, we are interested in the general characteristics of the ground motion, e.g., its peak amplitude and the spatial distribution and variability of these parameters. For observed ground motion large datasets of these general characteristics have been distilled into empirical attenuation relations. These are essentially equations describing how a measured quantity like peak ground velocity is expected to vary with magnitude of an event and observer distance. Often these equations also contain several additional factors to account for different faulting mechanism and local site response. In the present study we investigate

how the ground motion intensities of the synthetic seismograms for a subset of the dynamic rupture simulations described in *Ripperger et al.* [2007] compare with recent empirical attenuation relations. An example for such a comparison is provided by *Aochi and Douglas* [2006], who performed a similar analysis for dynamic rupture models with homogeneous initial stress.

Our study is laid out as follows: In the next section we briefly summarize the approach and the main results of *Ripperger et al.* [2007] and describe the selection of the dynamic rupture simulations. The following part describes the setup of the study and the techniques used to compute the synthetic seismograms. The fourth and main part of the paper is concerned with the estimation of ground motion characteristics of engineering interest from these synthetic seismograms and their comparison with empirically derived attenuation relations. In the fifth part we finally investigate how the variability in peak ground motion compares with that of a real event, using the large strong-motion dataset available for the 2004 Parkfield, California earthquake.

## 4.2 Dynamic Earthquake Rupture Simulations

The study of *Ripperger et al.* [2007] focused on exploring statistical descriptions of the initial stress heterogeneity on a fault and understanding how the stochastic stress parameters control the rupture behavior. Shear stress  $\tau_0(x, z)$  on the fault plane was modeled as a random field with a normal distribution of values and a given standard deviation. The wave-number spectra of the stress distributions were constrained to follow a power-law decay at high wave numbers, similar to the parameterization in the stochastic fault model of *Andrews* [1980]. Based on the spectral characterization of fault slip in kinematic source models [*Mai and Beroza*, 2002] the wave-number spectra were set to a constant level below a given corner wave number associated with the autocorrelation length  $a_c$  of the stress field. The Hurst parameter  $H$  controlling the fall-off at high wave numbers was systematically varied, as well as the correlation length  $a_c$  and the standard deviation  $std$  of stress.

Apart from the shear stress, the model setup was chosen rather simple. Friction on the fault is governed by a linear slip-weakening constitutive relation, where the yield strength  $\tau_s$ , frictional sliding strength  $\tau_d$  as well as the critical slip-weakening distance  $D_c$  are uniform. Thus also the fracture energy  $G_c = 1/2 D_c (\tau_s - \tau_d)$  is uniform. The fault itself is planar and is embedded in a homogeneous elastic full space. This setup is well suited to be treated numerically by a boundary integral method. The simulations were performed using the code MDSBI developed by *Dunham* [2005] using the methodology of *Geubelle and Rice* [1995]. The detailed model parameters are listed in Table 4.1.

The standard deviation  $std$  of the stress field was found to exert the strongest influence on the overall characteristics of the rupture because it mainly controls the average level of stress  $\bar{\tau}_0$  at the beginning of the rupture. The dimension-

Parameter	Symbol	Value
Density	$\rho$	2800 kg/m <sup>3</sup>
P-wave velocity	$v_p$	6000 m/s
S-wave velocity	$v_s$	3464 m/s
Critical slip-weakening distance	$D_c$	0.2 m
Yield strength	$\tau_s$	24 MPa
Frictional sliding strength	$\tau_d$	15 MPa
Grid spacing	$\Delta x$	150 m
Time sampling	$\Delta t$	0.013 s
Fault dimensions		15×30 km

**Table 4.1:** Model parameters of all dynamic rupture simulations of *Ripperger et al.* [2007] studied in this paper.

less  $\bar{\tau}_0$  is defined as  $\bar{\tau}_0 = \langle (\tau_0 - \tau_d) / (\tau_s - \tau_d) \rangle$ , where angle brackets denote averaging across the fault plane. A threshold in the average stress level was identified, above which ruptures tend to become unstoppable by the stress heterogeneity itself.

For the computation of ground motion we selected a subset of the large collection of dynamic rupture simulations of *Ripperger et al.* [2007]. First of all, we restrict the analysis to a range of seismic moment  $M_W = 6.7 - 6.9$ , where the chosen value of the fracture energy is appropriate. Secondly, only events are considered which do not exhibit wide-spread super-shear rupture velocity. This was achieved by excluding events with average rupture velocity above 0.8 times the shear-wave velocity. In total these criteria yielded 61 events out of a suite of more than 400 simulated ruptures. Their final slip distributions and rupture front contours are displayed in Figure 4.1 and their average macroscopic rupture properties are summarized in Table 4.2 for each set of stress field parameters  $H$ ,  $a_c$  and  $std$ . The properties of the selected dynamic events are consistent with empirically derived macroscopic source scaling laws [e.g., *Wells and Coppersmith*, 1994]. While this is also true for the ratio  $E_r/M_0$  of radiated energy to seismic moment, we note that  $E_r/M_0 \approx 1 - 4 \times 10^{-5}$  as obtained for our simulations is in the lower range of values estimated for similar sized real earthquakes [e.g., *Kanamori and Brodsky*, 2004]. This likely indicates that real events can exhibit large-scale fluctuations in their rupture propagation velocity that are more pronounced than the variations present in our dynamic simulations (Figure 4.1).

All selected rupture models have the same correlation length  $a_c = 5$  km of the stress field. Due to the differences in the Hurst exponent  $H$  the initial stress fields have different contents of high-wavenumber variability. However, as noted by *Ripperger et al.* [2007], this does not strongly influence the overall rupture behavior, which is mainly determined by the average stress level



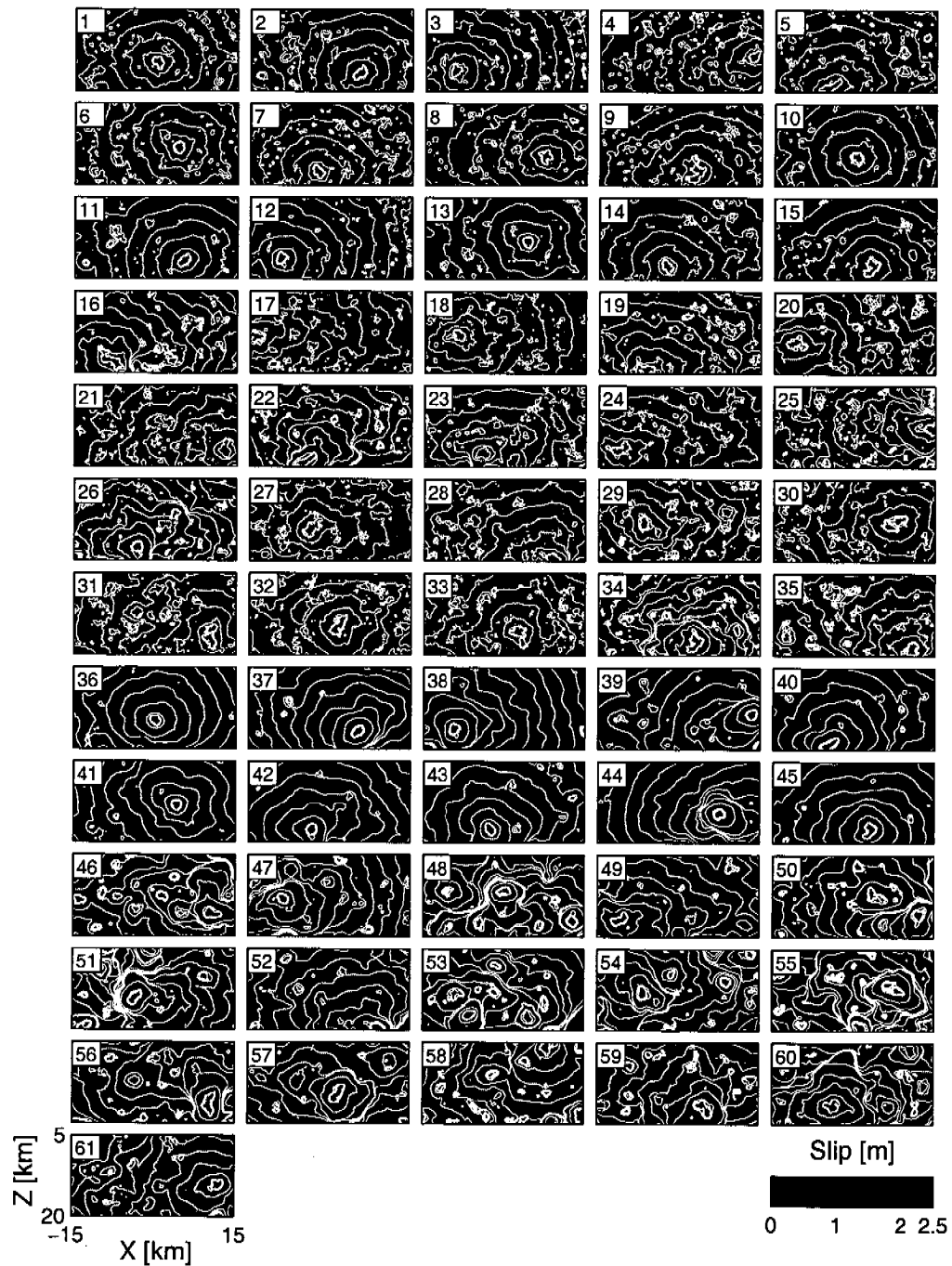


Figure 4.1: Final slip distributions of all runs and contours of the rupture front every second.

$H$	$a_c$ [km]	$std$ [MPa]	$\bar{\tau}_0$	$M_W$	Area [km <sup>2</sup> ]	No.	$N$
61 events with variable hypocenters:							
0.0	5.0	3.0	0.54	6.87	450	1-9	9
0.5	5.0	2.0	0.53	6.87	450	10-15	6
0.5	5.0	3.0	0.48	6.83	450	16-35	20
1.0	5.0	2.0	0.44	6.81	450	36-45	10
1.0	5.0	3.0	0.38	6.76	447	46-61	16
30 events with fixed hypocenter:							
0.5	5.0	2.0	0.45	6.80	450	Fig. 4.2	30

**Table 4.2:** Stress field parameters and averaged macroscopic properties of the dynamic rupture simulations selected from *Ripperger et al.* [2007] and the 30 new ones from this study. “No.” refers to the event numbers in Figure 4.1 and  $N$  gives the total number of selected simulations with the given parameter set  $H$ ,  $a_c$  and  $std$ .

$\bar{\tau}_0$ . With average stress levels of  $\bar{\tau}_0 = 0.35$ - $0.60$  all selected events are located above the size transition discussed in *Ripperger et al.* [2007], i. e. their final size is mainly determined by the fault extensions as reflected in the very similar rupture area. The differences in the average stress level result in differences in the amount of slip on the fault and therefore in the moment magnitudes  $M_W$ . The above mentioned selection criteria ensure that these variations in the macroscopic rupture properties remain within certain limits that allow all the selected models to be reasonably well considered as realizations of the same earthquake. Furthermore, in the comparison to empirical attenuation relations in the main part of this study, we will mainly analyze the residuals, i. e. the differences between each model and the corresponding empirical estimate for its particular moment magnitude. Since this effectively evens out the differences of average stress level, the main differences between the models is their hypocenter location and the relative distribution of the high- and low stress patches.

The hypocenter-station configuration is expected to be responsible for a significant part of the ground motion variability [e.g., *Aagaard et al.*, 2001]. Therefore, in addition to the simulations selected from *Ripperger et al.* [2007], we performed 30 new simulations in which the initial stress field was shifted to make the hypocenters coincide at the same point at  $z = 15$  km and  $x = -10$  km (Figure 4.2). Hence the ground-motion variability of these 30 rupture models originates solely from the different random phases of their initial stress fields, which will allow us to separately study this source of variability. The 30 new simulations were performed for only one set of stress field parameters ( $H = 0.5$ ,  $a_c = 5$  km and  $std = 2$  MPa) with their average macroscopic source properties listed in Table 4.2. They differ from the previous simulations in the

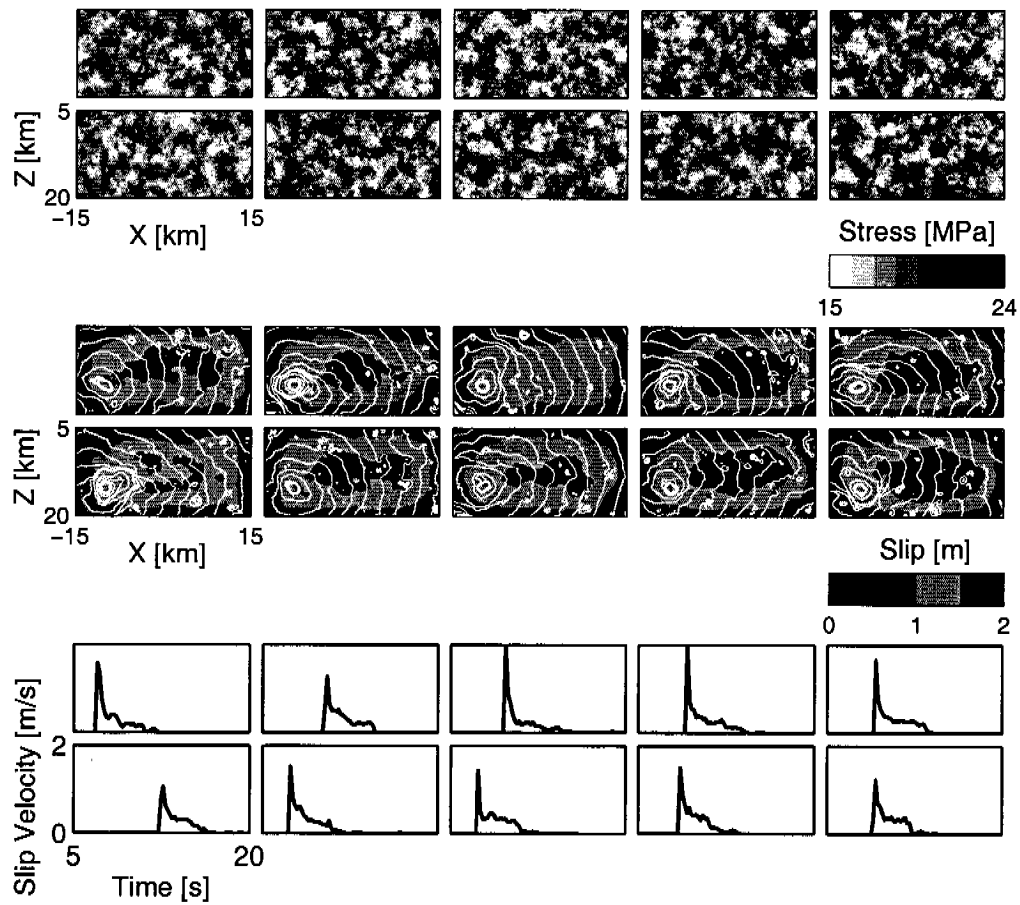


**Figure 4.2:** Initial stress distributions and resulting final slip distributions of 10 examples out of the 30 runs with hypocenter fixed at  $x = -10$  km,  $z = 15$  km. Overlain on the slip distributions are the contours of the rupture front every second. The lowermost panels show slip-velocity functions at the center of the fault.

way the static stress loading and nucleation is computed. In contrast to the approximate nucleation scheme employed in *Ripperger et al.* [2007] the new procedure [*Ampuero and Vilotte, 2007*] includes the effect of quasi-static pre-slip inside the nucleation zone. However, the differences during the nucleation phase are not expected to significantly alter the results in terms of the peak ground motions.

### 4.3 Computation of Synthetic Ground Motion

During the simulations of dynamic rupture propagation described above the time histories of slip-velocity have been stored for each grid point of the fault. These slip-velocity traces are then convolved with Green's functions of the medium response for a desired fault-receiver geometry to obtain synthetic seismograms of ground velocity.

#### 4.3.1 Fault and Receiver Geometry

Our synthetic ruptures are assumed to be strike-slip events taking place on a vertical fault plane. Since the dynamic rupture simulations were performed for a homogeneous full space, we place the top of the fault at a depth of 5 km. For more shallow faulting the influence of the free surface on the dynamic propagation might become significant, but for depths larger than 5 km this effect is thought to be negligible.

Seismograms were computed for a set of 50 hypothetical stations surrounding the fault at various azimuths and distances. The particular receiver configuration was chosen to sample the distance range between 1 and 60 km in terms of the closest distance to the surface projection of the fault (commonly denoted as "Joyner-Boore distance"  $r_{jb}$ ) with approximately equal azimuthal coverage. Within the fault extensions we positioned receivers along lines running parallel to the fault at various distances. In addition, beyond the ends of the fault receiver profiles extend radially outward with azimuths of  $0^\circ$ ,  $30^\circ$  and  $60^\circ$ . The receiver locations are specified in Table 4.3 and illustrated in Figure 4.3. Note that the empirical attenuation relations we compare our results against are provided as functions of distance to the rupture plane  $r_{rup}$  and distance to the seismogenic part of the rupture plane  $r_{seis}$ . With our chosen setup, these two distance metrics are identical and can be simply expressed as

$$r_{rup} = r_{seis} = \sqrt{r_{jb}^2 + (5 \text{ km})^2}. \quad (4.1)$$

Since large earthquakes are more likely to nucleate in the deeper part of the seismogenic zone [e.g., *Mai et al., 2005*], we only allow hypocenters to be located in the lower half of the fault plane, i. e. between 12.5 km and 20 km

$r_{jb} \approx 1$ km		$r_{jb} \approx 3$ km		$r_{jb} \approx 10$ km		$r_{jb} \approx 30$ km		$r_{jb} \approx 60$ km	
$x$	$y$	$x$	$y$	$x$	$y$	$x$	$y$	$x$	$y$
16.0	0.3	18.0	0.3	25.0	0.3	45.0	0.3	75.0	0.3
15.9	0.5	17.6	1.5	23.5	5.0	41.0	15.0	67.0	30.0
15.5	0.9	16.5	2.6	20.0	8.5	30.0	26.0	45.0	52.0
15.0	1.0	15.0	3.0	15.0	10.0	15.0	30.0	15.0	60.0
7.5	1.0	7.5	3.0	7.5	10.0				
0.0	1.0	0.0	3.0	0.0	10.0	0.0	30.0		
-7.5	1.0	-7.5	3.0	-7.5	10.0				
-15.0	1.0	-15.0	3.0	-15.0	10.0	-15.0	30.0	-15.0	60.0
-15.5	0.9	-16.5	2.6	-20.0	8.5	-30.0	26.0	-45.0	52.0
-15.9	0.5	-17.6	1.5	-23.5	5.0	-41.0	15.0	-67.0	30.0
-16.0	0.3	-18.0	0.3	-25.0	0.3	-45.0	0.3	-75.0	0.3

**Table 4.3:** Coordinates of receiver locations (in km) at which ground motions are computed, sorted by the closest distance to surface projection of fault plane, commonly known as Joyner-Boore distance  $r_{jb}$ . Also see Figure 4.3 for a map of the receivers.

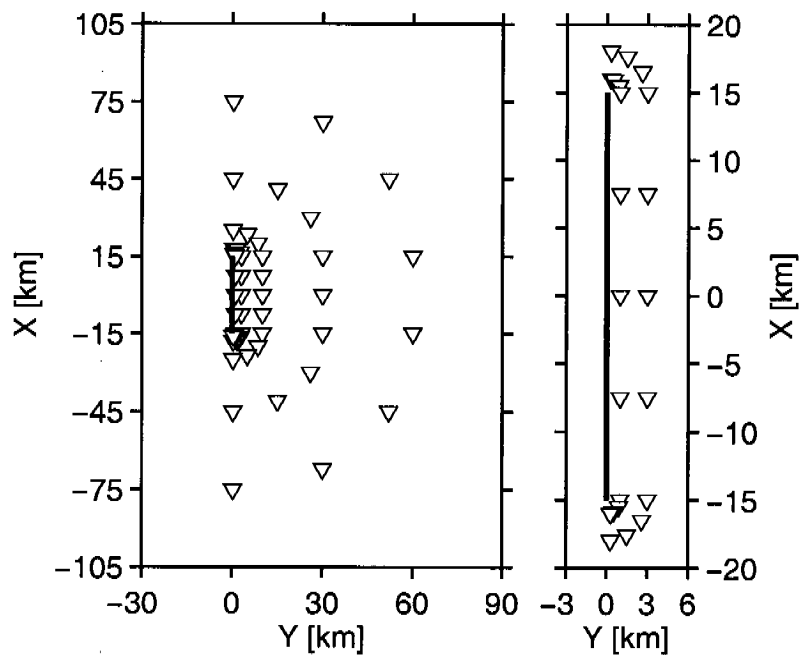


**Figure 4.3:** Map-view of station configuration. Thick line indicates the surface projection of the fault. The distances from the surface projection of the fault are 1, 3, 10, 30 and 60 km. Receiver coordinates are specified in Table 4.3.

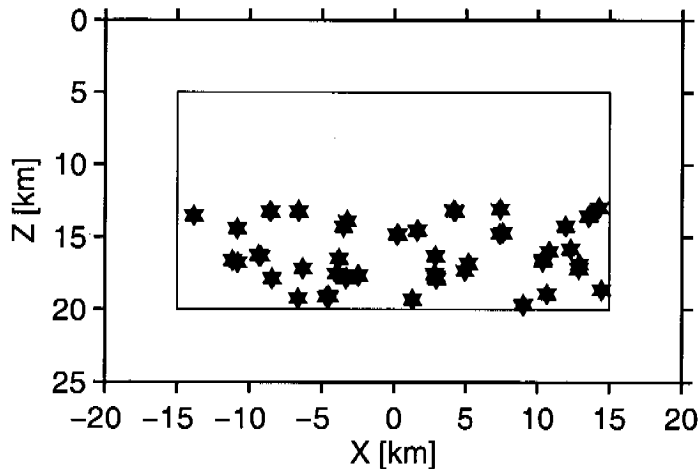


**Figure 4.4:** Side-view of the fault plane (black rectangle) and the locations of the hypocenters (black stars).

depth. For all events that originally had shallower hypocenters, we flipped the whole event upside down, which is possible because the dynamic rupture simulation was performed for a full space. The obtained hypocenter distribution is illustrated in fault-plane view in Figure 4.4.

As mentioned above, to single out the ground motion variability due to the initial stress heterogeneity only, we computed 30 additional models, where the hypocenter was fixed at  $z = 15$  km and  $x = -10$  km, which makes the ruptures propagate primarily unilateral.

### 4.3.2 Green's Functions

To calculate the Green's functions we utilize the discrete wavenumber / finite element method (DWFE) by *Olson et al.* [1984] as implemented in the COMP-SYN package by *Spudich and Xu* [2003]. The codes in this package make use of the reciprocity theorem and provide the Green's functions in form of tractions on a fault plane resulting from a delta pulse at the receiver location. These tractions  $\tau_{xx}$ ,  $\tau_{xy}$  and  $\tau_{xz}$  are specified in the frequency domain and on an irregular spatial grid that varies for different frequencies. We therefore interpolate the traction values on a rectangular grid and subsequently perform the inverse Fourier transform to retrieve traction time histories at the same points of the fault, where the slip-velocity traces are available from the dynamic simulations.

The three components of ground velocity  $v_x$ ,  $v_y$ ,  $v_z$  at each receiver site are obtained by convolving the slip velocity signal  $\Delta\dot{u}(t)$  with the corresponding traction time history at each point  $(i, j)$  of the fault and finally summing the

contribution of all grid points:

$$\begin{aligned}
 v_x(t) &= \sum_{ij} \Delta \dot{u}(t, i, j) * \tau_{xx}(t, i, j) \\
 v_y(t) &= \sum_{ij} \Delta \dot{u}(t, i, j) * \tau_{xy}(t, i, j) \\
 v_z(t) &= \sum_{ij} \Delta \dot{u}(t, i, j) * \tau_{xz}(t, i, j)
 \end{aligned} \tag{4.2}$$

The COMPSYN package allows for computing Green's functions for an arbitrary 1D velocity-density structure. However, we restrict the comparison to the simplest case of a homogeneous half-space. The Green's functions are designed to be accurate up to a frequency of 4 Hz. The time series are computed for a maximum duration of 45 s with a time sampling of 0.0216 s. The convolution of slip velocity and traction time series is performed utilizing the Fast Fourier Transform.

One disadvantage of the COMPSYN package is that the Green's functions are computed assuming a fully elastic medium, therefore not including any kind of inelastic attenuation. One way to approximately account for attenuation is to subsequently filter the seismograms with a so called  $t^*$ -operator [Futterman, 1962], which is dependent on travel time and the  $Q$ -value of the medium. We have performed this filtering for a number of  $Q$  values, taking  $r_{jb}/v_s$  as a proxy for the direct shear-wave travel time. We will show some results in the section on PGV, but where not explicitly noted otherwise the results presented in this paper are obtained without this filtering.

## 4.4 Ground Motion Characteristics

For seismic hazard assessment and engineering purposes many different attributes of ground motion records have been measured to express their intensity and damage potential. The most commonly used are peak ground acceleration (PGA) and spectral acceleration (SA) at different periods. But recently the destructive potential of velocity pulses has been acknowledged more widely [e.g., Wald *et al.*, 1999; Boatwright *et al.*, 2001] and peak ground velocity (PGV) has received increased attention. For all these measures of ground motion intensity large datasets have been compiled from recorded seismograms and researchers derived empirical attenuation relations that essentially describe the decay of shaking level with distance from the earthquake source.

In the following sections we will present examples of our synthetic waveforms and compare the measures of ground-motion intensity and their variability to recent empirical attenuation relations.

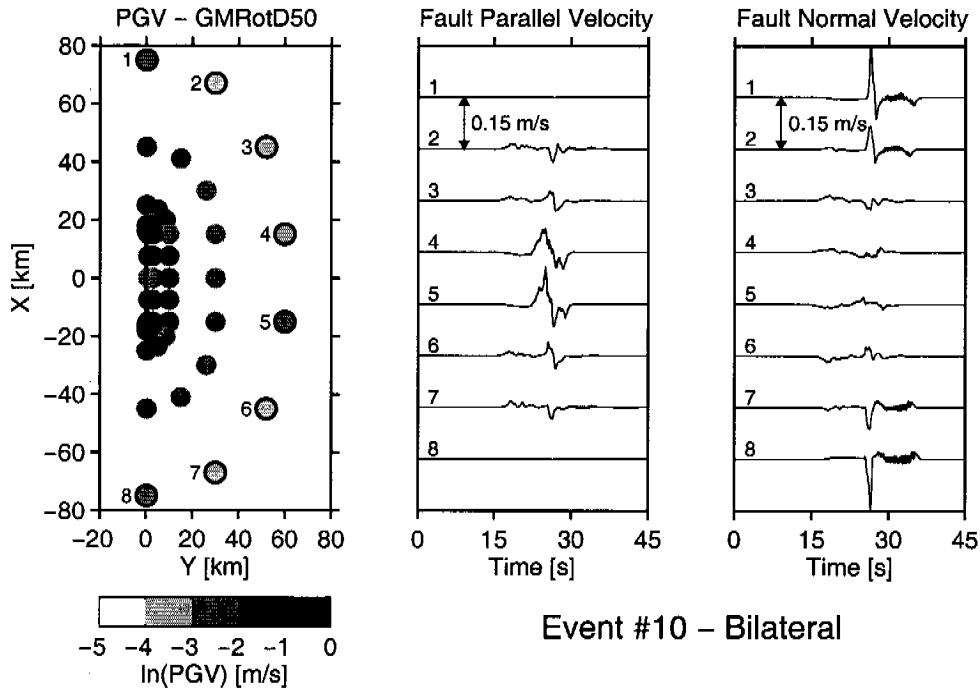


Figure 4.5: Map of horizontal PGV values (GMRotD50) for a single bilateral event (No. 10 in Figure 4.1), along with seismograms of the receiver ring at  $r_{jb} \approx 60$  km.

#### 4.4.1 Example Waveforms

Two typical examples of simulations and their associated synthetic velocity seismograms are presented in Figures 4.5 and 4.6. Figure 4.5 shows a bilateral event (No. 10 in Figure 4.1) starting approximately at the center of the fault. Accordingly, the seismograms in both rupture propagation directions are very similar in shape and amplitude. The fault-parallel component is largest at the receivers located in the direction perpendicular to the fault while the fault-normal component exhibits the largest amplitudes at stations in both directions along the fault strike. Both features are expected from the S-wave radiation pattern of a double-couple source [e.g., *Aki and Richards, 2002, p. 81*].

The predominantly unilateral rupture propagation of event no. 12 is illustrated in Figure 4.6. The signature of the unilateral propagation [e.g., *Somerville et al., 1997*] can clearly be seen in the seismograms. A strong velocity pulse is visible in the fault normal component in the forward directivity direction, its amplitude exceeding that of the bilateral case. No such pulse is apparent in the backward directivity direction, where the amplitudes are generally lower than in the bilateral case.



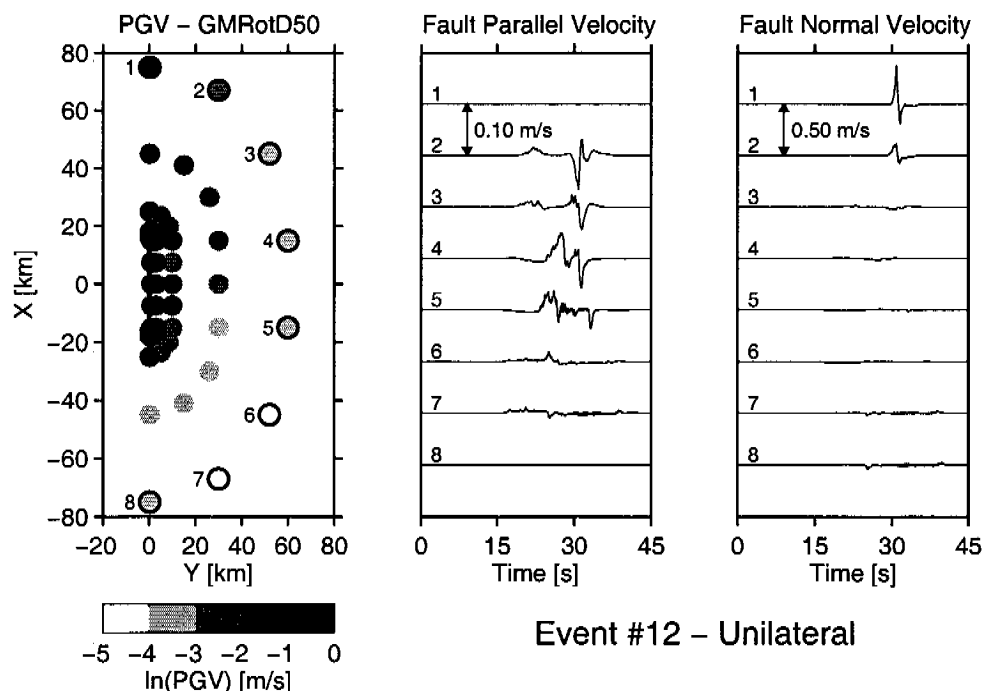


**Figure 4.6:** Map of horizontal PGV values (GMRotD50) for a single unilateral event, along with seismograms of the receiver ring at  $r_{jb} \approx 60$  km.

#### 4.4.2 Peak Ground Velocity

Peak ground velocity (PGV) is the most preferable measure to estimate on our synthetic seismograms, because it is sensitive to the frequency range that is covered by the rupture simulations. In contrast, peak ground acceleration (PGA) in real data is typically associated with higher frequencies that are not accurately resolved in the synthetics which are limited to a maximum frequency of 4 Hz.

We compare our results to the attenuation relations for PGV derived by *Campbell* [1997, 2000, 2001]). These relations give PGV as a function of distance of the receiver to the seismogenic rupture plane  $r_{\text{seis}}$ , which we simply take as the distance to the top of the fault plane at 5 km. Furthermore the relations are parameterized in terms of moment magnitude  $M_W$ , style of faulting and local site geology. For a first comparison we set  $M_W = 6.8$  and set the appropriate factors for pure strike-slip faulting and a “hard rock” site condition, since this site class comes closest to our assumed homogeneous half-space.

One issue that deserves careful consideration for the comparison of horizontal PGV is the way the two horizontal components of ground velocity are treated. This is illustrated in Figure 4.7. Separate PGV estimates of the fault-parallel and fault-normal component are presented in panels (a) and (b) of Figure 4.7. The fault-parallel component shows a large variability, mainly resulting from the receivers in approximately nodal positions of the radiation pattern, i. e.

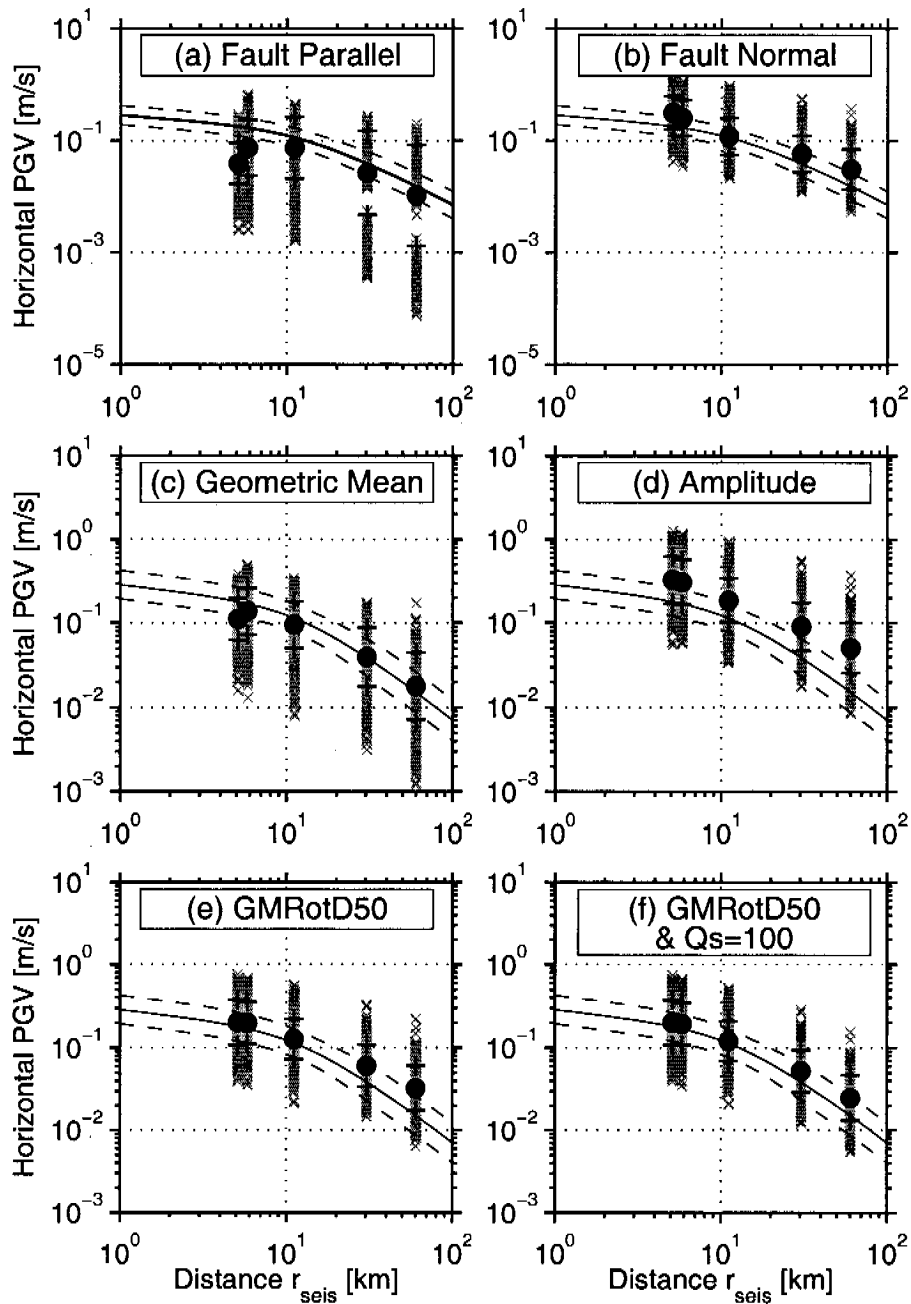


**Figure 4.7:** Comparison of PGV values of all 61 events of Fig. 4.1 with empirical attenuation relation. The individual PGV values are plotted in gray, their mean and standard deviation are indicated by the black circles and “+” signs, respectively. Solid and dashed lines display the attenuation relation of *Campbell* [1997] and its one sigma bounds for a  $M_W = 6.8$  event on a hard rock site. (a) Fault parallel component (b) Fault normal component (c) Geometric mean of both horizontal PGV values. (d) PGV values of vector sum of the two horizontal components. (e) Rotation independent geometric mean of PGV values as defined by *Boore et al.* [2006]. (f) Same as (e) with  $Q_S = 100$

close to the continuation of the fault trace along strike. For his regression analysis *Campbell* [1997] used the geometric mean of the separately derived PGV values as depicted in Figure 4.7c. At larger distances, the average PGV values agree very well with the empirical attenuation curve. At the shortest distance the average PGV value seems to decrease. This feature is only an effect of the orientation of the two components of the receiver. It vanishes for other estimates of horizontal PGV that are independent of receiver orientation such as the maximum amplitude  $\max(\sqrt{v_x^2 + v_y^2})$  displayed in Figure 4.7d. This is a physically more reasonable measure, since it represents a peak in horizontal velocity occurring at a single point in time. In contrast, the geometric mean of the two PGV components can originate from two separate wave arrivals in the two components at different times and is generally strongly dependent on the particular receiver orientation. Since the maximum amplitude as defined above is always equal to or larger than the geometric mean of the separate PGV estimates, the obtained average PGV values are well above the empirical relation.

Very recently the issue of sensor orientation has also been addressed by *Boore et al.* [2006] and the authors propose the orientation-independent measure GMrotD50. It comprises a rotation of the two orthogonal components from  $1^\circ$  to  $90^\circ$  in  $1^\circ$  steps and an evaluation of the geometric mean for each pair of rotated time series. The final measure is the median value of all 90 values of the geometric mean. The resulting PGV values are depicted in Figure 4.7e. An empirical attenuation relation of this measure is not yet available, but *Beyer and Bommer* [2006] investigated the relationship between GMrotD50 and empirical attenuation curves based on the geometric mean definition, finding only minor differences. Thus GMrotD50 constitutes a better measure than the geometric mean to compare the empirical data (with typically random sensor orientation) and our simulations (with components oriented exactly parallel and normal to the fault plane) and will be used throughout the remainder of the paper.

A difference observable in Figure 4.7e is the lower fall-off rate with distance of our PGV estimates compared to the empirical relation, which is potentially caused by the omission of inelastic attenuation. The effect of applying the attenuation correction via the  $t^*$ -operator [*Futterman*, 1962] is shown in Figures 4.7d for  $Q = 100$ . For assumed values of  $Q = 200$  or larger (not shown), appropriate for average crustal rocks, the difference compared to the purely elastic case is very small. A slight reduction of PGV values is observed for  $Q = 100$ , where the fall-off with distance of our synthetic PGV values is comparable with the empirical attenuation relation and the mean PGV value is within the 1-sigma bounds of the empirical attenuation relation.

PGV				
$r_{jb}$ [km]	$\mu_r$	$\sigma_r$	$\sigma_e$	$\sigma_a$
61 events, variable hypocenters:				
1	0.12	0.62	0.60	0.44
10	0.10	0.54	0.50	0.41
30	0.43	0.55	0.48	0.48
60	0.74	0.60	0.51	0.54
30 events, fixed hypocenter:				
1	-0.08	0.81	0.48	0.74
10	-0.03	0.67	0.31	0.65
30	0.30	0.72	0.24	0.74
60	0.61	0.80	0.24	0.83

**Table 4.4:** PGV Residuals.  $\mu_r$ ,  $\sigma_r$ : mean and standard deviation of residuals for all receivers at the given distance.  $\sigma_e$  and  $\sigma_a$ : average inter- and intra-event standard deviations, respectively.  $\sigma_e$  is the average over all receivers at a given distance while  $\sigma_a$  is the average over all events.

### 4.4.3 PGV-Variability

Having confirmed the overall agreement of our PGV estimates with the empirical attenuation relation, we now proceed to a closer inspection of the variabilities. Part of the variability in the PGV values plotted in Figure 4.7 is due to the differences in moment magnitude  $M_W = 6.7-6.9$  of the events compared to the assumed  $M_W = 6.8$  for the attenuation relation. To compare each PGV value with the appropriate value predicted from the attenuation relations, we define the residual  $r$  as

$$r = \ln(PGV_{\text{syn}}) - \ln(PGV_{\text{emp}}) = \ln\left(\frac{PGV_{\text{syn}}}{PGV_{\text{emp}}}\right), \quad (4.3)$$

where  $PGV_{\text{syn}}$  and  $PGV_{\text{emp}}$  are the PGV values from the synthetic seismograms and the empirical prediction, respectively. Figure 4.8 presents the distribution of these residuals separated for each distance range. The mean value of the residuals is always positive and generally increasing with distance. This reflects the slight overprediction of PGV values with increasing distance as noted above. The standard deviation  $\sigma_r$  of the residuals remains approximately constant at  $\sigma_r = 0.54-0.62$  for all distances. This variability is somewhat larger than the standard deviations of 0.39-0.55 specified for the empirical attenuation equation, but still of the same order of magnitude.

The origin of the variability in the PGV residuals is further investigated by looking at the residuals for each station separately. Figure 4.9 illustrates how the variability at each distance range is composed by the inter-event variability  $\sigma_e$  (i. e. variability at single receivers due to different events) and the intra-event

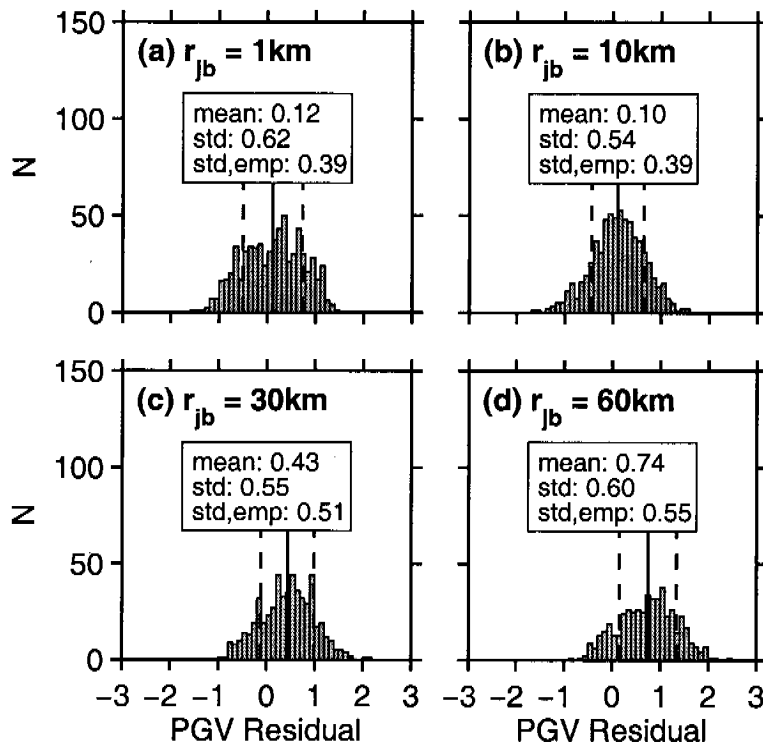


**Figure 4.8:** Distribution of residuals  $\ln(PGV_{syn}/PGV_{emp})$  of horizontal PGV (GM-RotD50) at each distance range for all 61 events of Fig. 4.1. Mean and standard deviation of the residuals are indicated by solid and dashed black lines, respectively. For comparison, the corresponding standard error estimate of the empirical attenuation relation by *Campbell* [1997] is specified as “std,emp”.

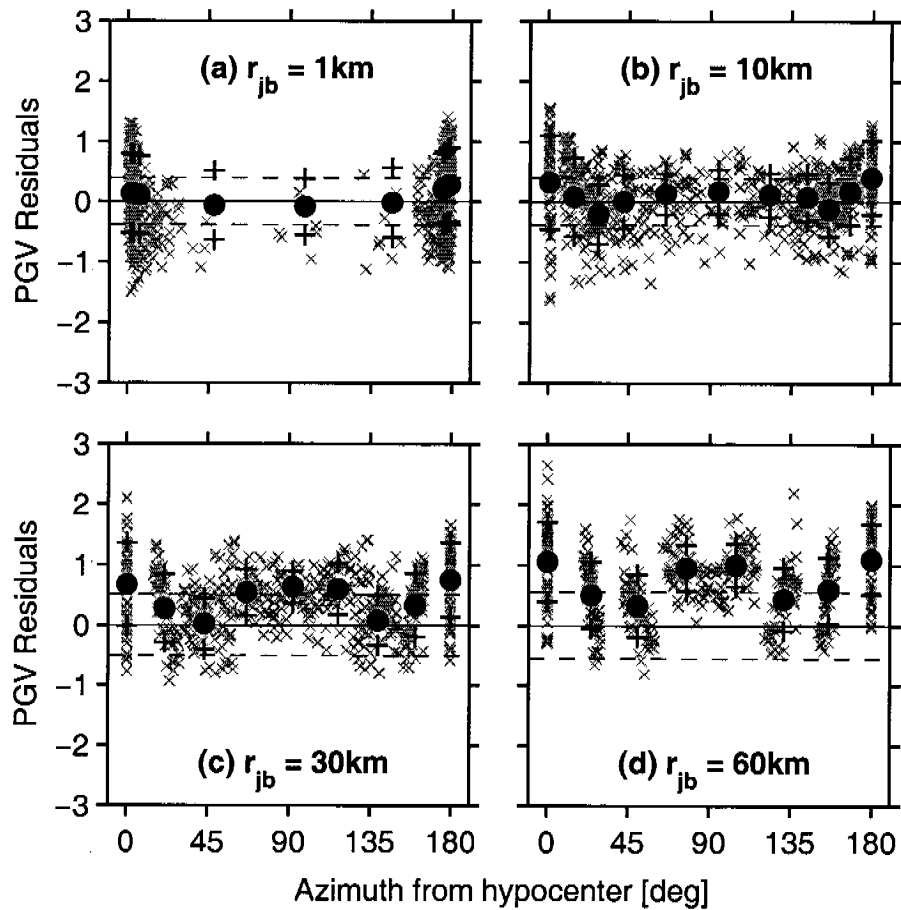


Figure 4.9: PGV residuals for single stations along receiver rings ( $r_{jb} \approx 1, 10, 30$  and  $60\text{ km}$ ) for all 61 events of Fig. 4.1. Residual values are plotted in gray, their mean and standard deviation are indicated by the black circles and “+” signs, respectively. Dashed horizontal lines specify the average standard deviation of the empirical relation for each distance range.

variability  $\sigma_a$  (i. e. variability within all the recordings of a single event at different receivers). As a general trend, the inter-event standard deviation  $\sigma_e$  of the residuals is lowest in the azimuthal range around  $90^\circ$ , i. e. perpendicular to the fault plane from the hypocenter. This is the region where directivity does not play a role and thus the variability here is thought to represent only the differences in the rupture process due to the stress heterogeneity and the average stress level. Apart from the distance range of 1 km, where the standard deviation of the residuals is poorly defined at the central azimuthal range, the inter-event variability shows values of roughly  $\sigma_e \approx 0.30$ . This is lower than the total standard deviation  $\sigma_r$  for each distance range as estimated above. As can be seen in Figure 4.9, the higher total  $\sigma_r$  originates from two sources. First of all, the inter-event variabilities are higher ( $\sigma_e \approx 0.6-0.7$ ) at the lower and upper ends of the azimuthal range, i. e. in the region, where a receiver may either be situated in a forward or backward directivity position. Secondly, the S-wave radiation pattern leads to intra-event variabilities  $\sigma_a \approx 0.5$  in the same range as the average inter-event variability. This is reflected by the differences in the mean PGV value along a receiver ring, showing up in Figure 4.9 as the distinct “W-shape” of the average residual curve (higher residuals in the regions of  $0^\circ$ ,  $90^\circ$  and  $180^\circ$  and lower values in between), especially at larger distances.

We can further focus on the variability originating from the stress heterogeneity by analyzing the 30 model runs with fixed hypocenter. They have absolutely identical stochastic stress parameters ( $H = 0.5$ ,  $a_c = 5$  km and  $std = 2$  MPa) and with the hypocenter fixed at  $x = -10$ ,  $z = 15$  they are forced to have approximately the same unilateral rupture propagation. The remaining inter-event variability of the ground motion estimates is therefore thought to originate purely from the random nature of the stress field.

Figure 4.10 presents the PGV residuals at each receiver ring for these 30 simulations. Several observations can be made. First of all, the inter-event variability  $\sigma_e$  at each single receiver is lower than the total standard deviation for the whole suite of simulations, which is expected because of the forced similarity of the rupture process.

Secondly, the average inter-event variability of the residuals decreases from  $\sigma_e \approx 0.48$  at  $r_{jb} = 1$  km towards  $\sigma_e \approx 0.24$  at  $r_{jb} = 60$  km. This demonstrates that the influence of the random fault stress on the ground motion gets weaker with distance from the source. This is again the expected behavior, since the distant stations experience more an integrated effect of the rupture process, while the near-fault stations are sensitive to local rupture complexities.

Thirdly, the largest variability for a single station within a given distance range is always observed in the backward directivity region whereas the smallest variability is always observed in the forward directivity region. This indicates that the directivity pulse due to the forced unilateral rupture propagation dominates the PGV estimate in the forward direction, while the differences in the rupture process are more likely to show up in the PGV measure in the back-

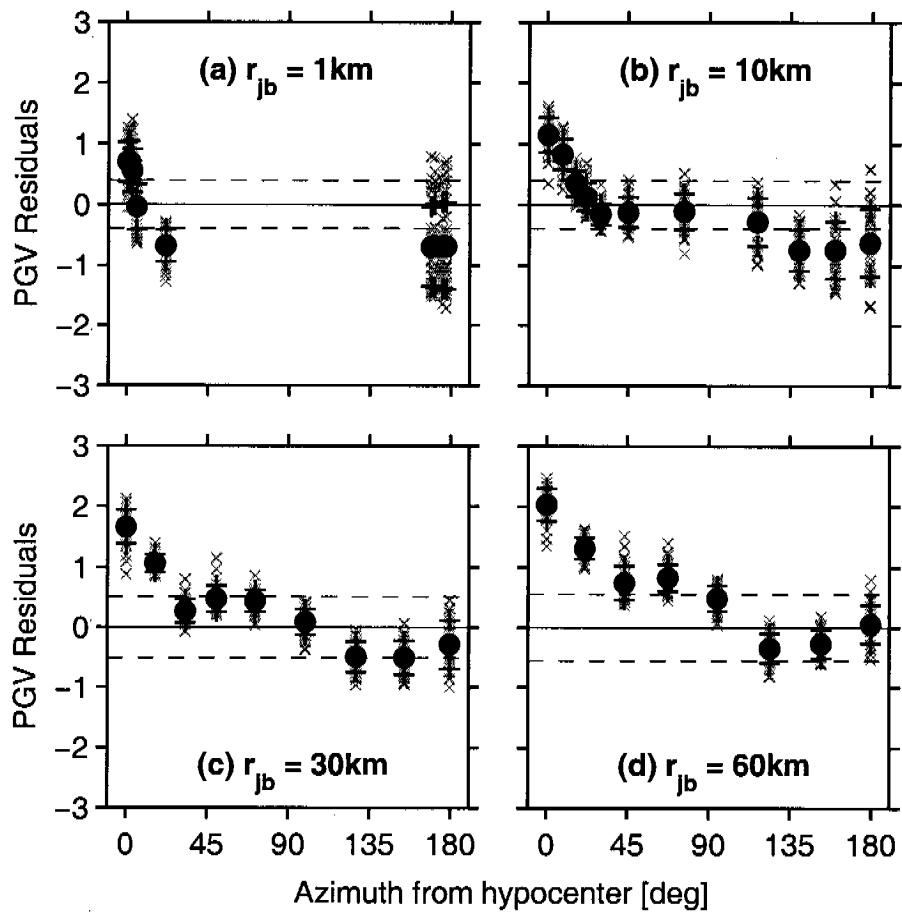


**Figure 4.10:** Same as Figure 4.9, but for the 30 simulations with fixed hypocenter. The directivity effect clearly shows up as high positive residuals at small azimuths (i. e. in the forward directivity region) and negative residuals at large azimuths (i. e. in the backward directivity region). The inter-event variability at each station is smaller compared to Figure 4.9.



ward direction.

Finally, the average residuals vary strongly with azimuth, clearly reflecting the directivity pattern. The resulting intra-event variability of  $\sigma_a \approx 0.7-0.8$  is dominating the overall variability of a distance range ( $\sigma_r \approx 0.7-0.8$ ).

#### 4.4.4 Spectral Acceleration

Spectral acceleration (SA) at different periods is a widely used parameter to quantify ground motion intensity in seismic hazard analysis and engineering seismology. In the following we compare SA estimates of our synthetic ground motions with empirical attenuation relations derived by *Campbell and Bozorgnia* [2003]. The choice of this particular set among other published attenuation relations [e.g., *Abrahamson and Silva*, 1997; *Ambraseys et al.*, 2005] was motivated by the separate treatment of the “firm rock” site class (same as “hard rock” in *Campbell* [1997]), which we consider more appropriate to compare with our assumed homogeneous half-space than the generic “rock” class used by most other attenuation relations.

At short distances, the spectral acceleration relation for “firm rock” by *Campbell and Bozorgnia* [2003] is similar to the relation by *Abrahamson and Silva* [1997] for generic “rock”, but it decays faster at larger distances. Detailed comparisons between different spectral acceleration attenuation relations can be found for example in *Campbell and Bozorgnia* [2003].

The computation of SA values for our synthetic seismograms is done by differentiating the ground velocity time histories to obtain acceleration traces and subsequently using the method of Newmark [e.g., see *Chopra*, 2001] to compute SA values for periods of  $T = 0.25, 0.5, 1$  and  $4$  s with a damping coefficient of  $\zeta = 5\%$ . The empirical attenuation relations by *Campbell and Bozorgnia* [2003] provide SA as a function of distance to the seismogenic rupture plane  $r_{\text{seis}}$ . As additional parameters for the attenuation equation we assume a  $M_W = 6.8$  strike-slip event and set the appropriate factors for the “firm rock” site conditions. The comparison for the four different periods is shown in Figure 4.11.

Our SA values are consistently lower than predicted by the empirical relation. The differences are largest for  $T = 0.25$  s, and decrease towards longer periods until at  $T = 4$  s the empirical relation is well matched at the farthest receivers. The fall-off rate with distance is generally in good agreement with the empirical relation, the exception being the nearest receivers (1 km and 3 km distance to the surface projection of the fault) at the longest period of  $T = 4$  s.

We analyzed the variability in the spectral acceleration (SA) residuals in the same way as for the PGV-variability. In analogy to eq. (4.3) we define the SA residuals as  $r^{\text{SA}} = \ln(SA_{\text{syn}}) - \ln(SA_{\text{emp}})$ . For the period of  $T = 1$  s Figure 4.12 illustrates the distribution of the residuals for different distances and Table 4.5 summarizes their variabilities. In general, the spatial distribution of

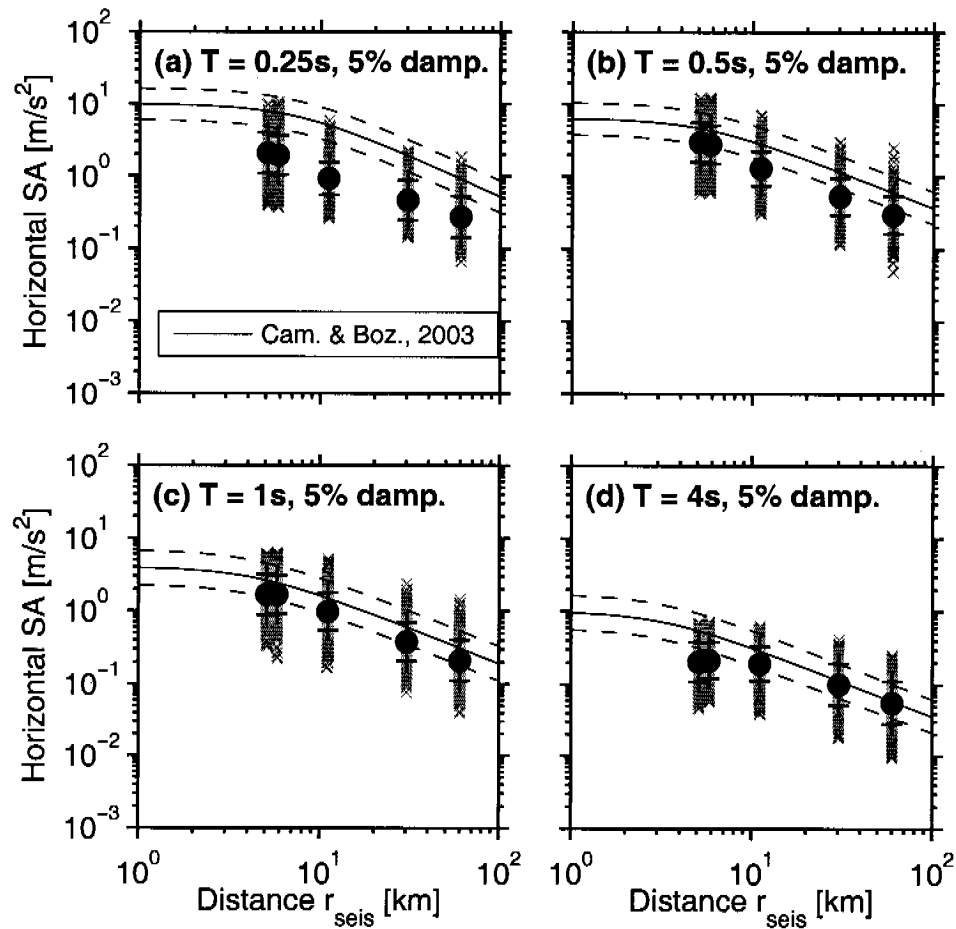


**Figure 4.11:** Comparison of horizontal spectral acceleration for all 61 events of Fig. 4.1 with empirical attenuation relation for periods of 0.25, 0.5, 1 and 4 s. The individual SA values (GMRotD50, see text) are plotted in gray, their mean and standard deviation are indicated by the black circles and “+” signs, respectively. Solid and dashed lines display the attenuation relation of *Campbell and Bozorgnia* [2003] and its one sigma bounds for a  $M_W = 6.8$  event on a firm rock site.

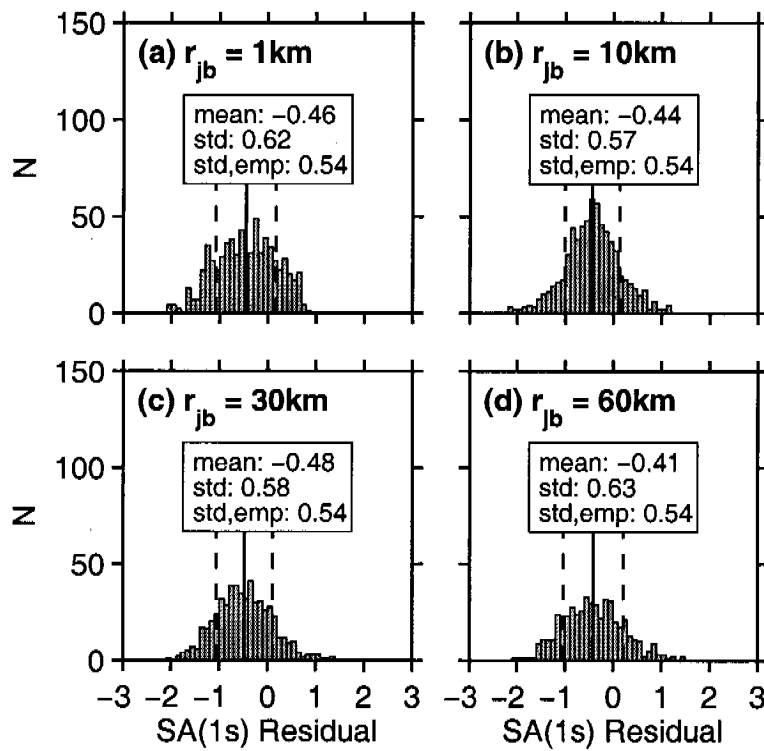


**Figure 4.12:** Distribution of residuals  $\ln(SA_{\text{syn}}/SA_{\text{cmp}})$  for horizontal spectral acceleration (GMRotD50,  $T = 1$  s, 5% damping) at each distance range for all 61 events of Fig. 4.1. Mean and standard deviation of the residuals are indicated by solid and dashed black lines, respectively. For comparison, the corresponding standard error estimate of the empirical attenuation relation by *Campbell and Bozorgnia* [2003] is specified as “std,emp”.

SA				
$r_{jb}$ [km]	$\mu_r$	$\sigma_r$	$\sigma_e$	$\sigma_a$
61 events, variable hypocenters:				
1	-0.46	0.62	0.61	0.44
10	-0.44	0.57	0.52	0.46
30	-0.48	0.58	0.50	0.54
60	-0.41	0.63	0.53	0.59
30 events, fixed hypocenter:				
1	-0.57	0.80	0.53	0.71
10	-0.62	0.69	0.40	0.67
30	-0.62	0.79	0.37	0.80
60	-0.57	0.81	0.37	0.83

**Table 4.5:** SA Residuals for period  $T = 1$  s.  $\mu_r$ ,  $\sigma_r$ : mean and standard deviation of residuals for all receivers at the given distance.  $\sigma_e$ ,  $\sigma_a$ : inter-event and intra-event standard deviations for each distance range.  $\sigma_e$  is averaged over the receivers while  $\sigma_a$  is the average value over all events.

the variability and its inter- and intra-event components are very similar to the values obtained for PGV.

## 4.5 PGV Variability of the 2004, Parkfield Earthquake

### 4.5.1 Intra-event Variability

The large number of ground-motion histories recorded close to the fault during the 2004, Parkfield, California earthquake make this event a prime candidate for an estimation of the intra-event variability. However, since most of the Parkfield stations have a local site geology classified as “soil” a direct comparison to our synthetics obtained for a homogeneous halfspace is not possible. Furthermore, rupture in the Parkfield event reached the surface, whereas our simulations assume a buried rupture. Nevertheless the Parkfield recordings currently provide the best available dataset for evaluating the intra-event variability in the near-fault region of a strike-slip earthquake.

In a first step we make use of the PGV and distance data provided in Table 1 of *Shakal et al.* [2006]. There, PGV is given for each station as the larger of the East-West or North-South components and distance is expressed as the closest distance to the fault surface trace. From the 95 stations listed in the table we selected all stations within the first 10 km from the fault, excluding the ones associated with buildings and also Fault Zone 16 for which no PGV value was

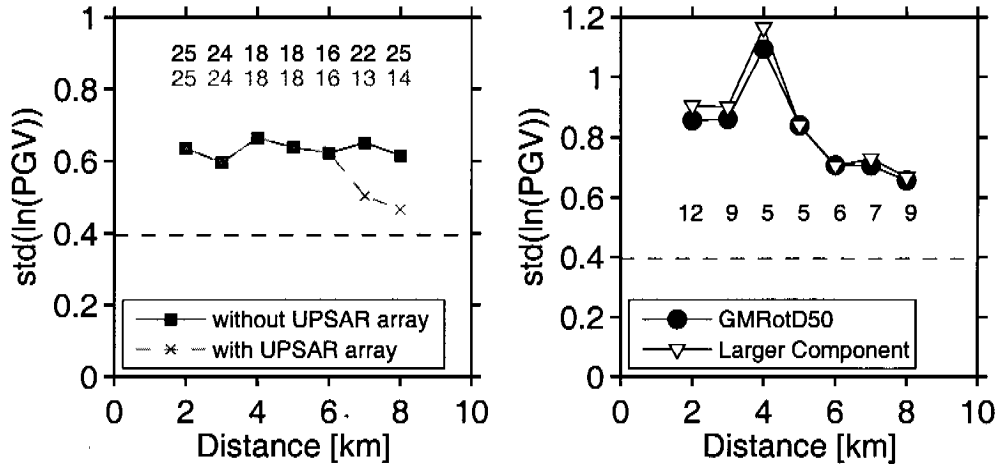


**Figure 4.13:** (left) Intra-event variability of PGV obtained from the data given in Table 1 of *Shakal et al.* [2006]. The values above the symbols denote the number of stations per distance bin. The black curve was obtained by excluding 11 of the 12 UPSAR array stations, which are located close to each other at roughly 9 km distance from the fault. (right) Similar analysis for stations with local geology classified as “soil”.

specified. These criteria yielded a set of 58 stations remaining for analysis. To make the estimation of the standard deviation more reliable, the variability at each given distance  $r$  from the fault is evaluated for all stations within a distance bin given by  $r \pm 2$  km. The PGV intra-event variability was calculated as the standard deviation of the logarithm of the PGV values in each distance bin and is displayed in Figure 4.13. From 0 to 7 km the variability is roughly constant at values between 0.60 and 0.65. The apparent strong decrease at distances larger than 7 km can be largely attributed to the 12 stations of the UPSAR array [Fletcher et al., 1992, 2006] which are located within a radius of about 1 km from each other at a distance of roughly 9 km from the fault. If all of the array stations apart from the central one are excluded (Fig. 4.13), the variability continues on the same level out to 10 km distance.

The analysis described above used data from all available stations, irrespective of their local site geology. In a second step we therefore estimate the variability of ground motion within a single site class. For a comparison to our synthetic results the “rock” site class would be the most interesting, but only the stations classified as “soil” are available in sufficiently large numbers for a statistical quantification. The geological classification for the stations of the California Strong Motion Instrumentation Program (CSMIP) was taken from the COSMOS web site (<http://www.cosmos-eq.org>) but was not available for the USGS stations. From the 58 stations of the previous analysis we again exclude the UPSAR array stations apart from the central one. Of the remaining 47 stations, 22 are classified as soil stations. Figure 4.13b shows the

intra-event variability for these stations. The number of stations per distance bin is of course much lower than before, making these estimates less reliable. One curve displays the variability for the larger horizontal component as before, while the other is obtained for the GMRotD50 of PGV *Boore et al.* [2006] calculated from the velocity waveforms. For this we used the corrected velocity traces as provided in the COSMOS database. To use the same frequency band as in our synthetics, the seismograms were additionally lowpass filtered (cutoff 4 Hz) with a 4th order causal Butterworth filter. Through filtering the PGV estimates are lowered by  $\sim 10\%$  on average, which results in an average increase of the variabilities by  $10\%$  in the case of GMRotD50 and  $14\%$  when using the larger horizontal component.

For our simulated velocity seismograms we found PGV intra-event variabilities within the first 10 km of  $\sim 0.4$  for variable hypocenter positions and roughly 0.7-0.8 for uni-laterally propagating ruptures (Table 4.4). Since the 2004 Parkfield, California earthquake propagated mainly unilaterally, the PGV intra-event variabilities determined for the Parkfield recordings are in the same range as the variabilities obtained for our simulated velocity seismograms.

### 4.5.2 Spatial Correlation of PGV

The spatial variability of peak ground velocity of the Parkfield earthquake was analyzed by *Shakal et al.* [2006] using the approach described by *Boore et al.* [2003], essentially characterizing the spatial correlation of peak ground motion by studying how its variability is changing with increasing interstation distance. In the following we will perform the same analysis for our synthetic data. It consists of the following steps:

1. For all possible station pairs (1225), the interstation distance  $\Delta$  is calculated.
2. For each pair, the difference between the logarithms of the PGV value is calculated, after accounting for the different fault distances. The latter correction is done using the PGV attenuation relation of *Campbell* [1997]. Thus the difference in  $\ln(PGV)$  is calculated as

$$\Delta \ln PGV = \left| \ln(PGV_1) - \ln(PGV_2) \frac{\ln(PGV_{\text{emp}}(r_1))}{\ln(PGV_{\text{emp}}(r_2))} \right|, \quad (4.4)$$

where  $PGV_{1,2}$  are the simulated PGV values at two stations and  $PGV_{\text{emp}}(r_{1,2})$  are the empirical PGV estimates of *Campbell* [1997] for the distances  $r_{1,2}$  of the two stations from the fault.

3. The station pairs are sorted by interstation distance in ascending order.

4. The standard deviation  $\sigma_{\Delta \ln \text{PGV}}$  of  $\Delta \ln \text{PGV}$  is calculated for each set of 15 consecutive station pairs.
5. The obtained value of the standard deviation is plotted versus the median value of the interstation distance of the 15 pairs.

To model the variation of  $\sigma_{\Delta \ln \text{PGV}}$  with interstation distance  $\Delta$  a relationship of the form

$$\sigma_{\Delta \ln \text{PGV}} = \sigma_{\text{indobs}} \cdot \sqrt{1 + \frac{1}{N} \cdot F(\Delta)} \quad (4.5)$$

was used by *Boore et al.* [2003], where  $\sigma_{\text{indobs}}$  denotes the standard deviation of an individual observation about a regression. As long as pairs of stations are considered,  $N = 1$  (*Boore, 2007, personal communication*) and  $\sigma_{\text{indobs}} \cdot \sqrt{2}$  is the variability reached asymptotically at large interstation distances. The function  $F(\Delta)$  defines the spatial correlation and is given by *Boore et al.* [2003] as

$$F(\Delta) = 1 - \exp(-\sqrt{C} \Delta) \quad (4.6)$$

where  $C$  is a constant inversely related to a spatial correlation length. The PGA data of the 1994, Northridge earthquake was approximately fit by using  $C = 0.6$  and  $\sigma_{\text{indobs}} = 0.188$  [*Boore et al., 2003*]. The PGV data of the 2004, Parkfield earthquake was shown to be consistent with  $C = 0.6$  and  $\sigma_{\text{indobs}} \approx 0.24$  (values estimated by graphically matching Figure 20 of *Shakal et al.* [2006]).

We computed regressions on our synthetic data (Figure 4.14) assuming a functional form of equation (4.5) with  $N = 1$ . The curves are least-square fits over the range from 0 to 30 km with the two free parameters  $\sigma_{\text{indobs}}$  and  $C$ . The obtained regression curves are displayed in Figure 4.14 for the 61 models with variable hypocenters and the 30 models with fixed hypocenter separately. Added to the plots in Figure 4.14 is a regression on the median values and the curves of *Boore et al.* [2003] and *Shakal et al.* [2006] with the values specified above.

For the 61 events with variable hypocenters the regression on the median values yields  $\sigma_{\text{indobs}} \approx 0.30$  and  $C = 0.089$ . For the 30 runs with fixed hypocenter we obtain values of  $\sigma_{\text{indobs}} \approx 0.73$  and  $C = 0.013$ . The obtained values for  $\sigma_{\text{indobs}}$  roughly match the average intra-event variabilities estimated in section 4.4.3 (Table 4.4), but are higher than the value found by *Shakal et al.* [2006] for the Parkfield earthquake. Our generally lower values of  $C$  indicate longer correlation lengths than estimated by *Boore et al.* [2003] and *Shakal et al.* [2006].

## 4.6 Discussion

Directivity is generally found to play an important role in the simulated ground motions. *Somerville et al.* [1997] proposed empirically derived modifications

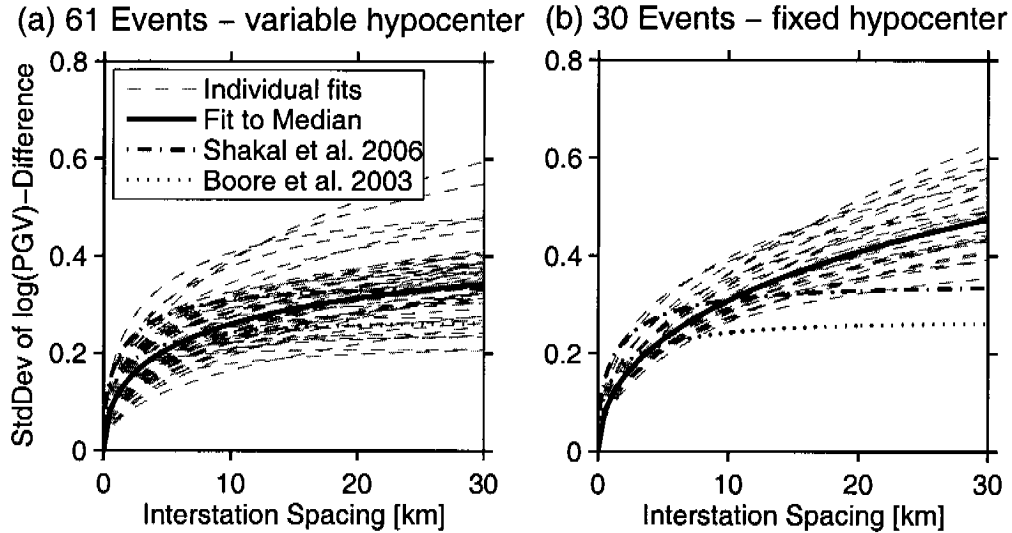


**Figure 4.14:** Regressions on standard deviation of the difference of  $\ln(\text{PGV})$  for all station pairs versus interstation distance (a) for the 61 events with variable hypocenters and (b) for the 30 events with fixed hypocenter. The solid black line represents the fit to the median values. The dash-dotted line reproduces the curve of *Shakal et al.* [2006, Fig. 20] fitting the PGV data of the 2004, Parkfield earthquake. Our analysis used the GMRotD50 value of PGV instead of the larger horizontal component as in *Shakal et al.* [2006]. Finally the stippled line reproduces the curve presented in *Boore et al.* [2003, Fig. A1] to fit the PGA data for the 1994, Northridge earthquake.

based on the hypocenter-receiver geometry to incorporate the effects of directivity into SA attenuation relations. We applied these modifications to the attenuation relationship of *Campbell and Bozorgnia* [2003] and repeated the calculation of the SA-residuals. The newly obtained residuals are smaller, i. e. the SA values are closer to the empirical relation and their overall variability is reduced, thus confirming that the modifications of *Somerville et al.* [1997] capture the basic features of rupture directivity correctly. However, the achieved improvements are generally minor (e.g., 0.01-0.04 log units for both  $\mu_r$  and  $\sigma_r$  at 1 s period) and cannot account for the total discrepancies between SA of simulated and empirical ground motion estimates.

The prominence of directivity effects in our simulations indicates that the seismic energy is radiated coherently despite some small-scale heterogeneity in the initial shear stress. As noted already by *Ripperger et al.* [2007], heterogeneity in fracture energy might be more efficient in changing the rupture velocity to be more variable and thus lead to less coherent radiation.

Nevertheless the random nature of the stress field leads to some variability in the ground motion, but this variability is in many cases superseded by the intra-event variability originating from the radiation pattern and directivity. Averaged over many events with different propagation directions, the total standard deviation of the residuals is on the order of  $\sigma_r \approx 0.55$ -0.65. This is in accord with the results by *Aochi and Douglas* [2006], who found a scatter



in the simulations of  $\sigma_r \approx 0.46 - 0.69$  (0.2-0.3 in  $\log_{10}$  units) irrespective of the chosen scenario. Their simulations model rupture dynamics, but with completely homogeneous stress and friction parameters and for only one event for each scenario, hence their scatter only represents the intra-event variability. These values of the intra-event variability and also some of those obtained for our simulations may appear high and are in fact sometimes larger than standard deviations given in empirical attenuation relations. However, a high PGV intra-event variability of  $\sigma_a \approx 0.6$  was obtained for the complete set of stations of the 2004 Parkfield earthquake. It is attributed to the mainly uni-directional nature of the rupture process. The even higher variabilities of  $\sigma_a \approx 0.7 - 0.9$  obtained for the subset of soil stations may be partially biased by the small number of stations used for the analysis, but may also reflect a true increase in the variability due to strong effects of local site geology. These local site effects along with the three-dimensional crustal structure of the Parkfield area are probably also responsible for the shorter spatial correlation lengths of the Parkfield ground motion compared to our synthetics for which a homogeneous half-space has been assumed.

The importance of the directivity effect has also been elucidated by studies involving kinematic source models [e.g., *Aggaard et al.*, 2001]. There the most important source parameters influencing the ground motion were found to be the depth of the fault, the rupture velocity and the hypocenter-station geometry, in particular the duration a rupture travels towards the observer.

Accordingly, one approach to predict the average ground motion level and its variability could be to construct many kinematic models with varying fault depths, hypocenter positions and rupture velocities. However, one would have to introduce some randomness in rupture velocity and the hypocenter position and possibly also in the slip and rise-time distribution to do so. Hence in the long run it may become the more natural and more physically constrained choice to quantify the uncertainty in the physical parameters such as stress and fracture energy as stochastic distributions on a given fault and do dynamic rupture simulations. These simulations will produce suites of models with varying hypocenters, rupture velocities etc. as a result rather than an a priori input. However, we also have to stress that at present there is no general consensus among scientists on the way dynamic models should be parameterized and in any of the models many of the input parameters are poorly constrained. Meanwhile, pseudo-dynamic modeling as proposed by *Guatteri et al.* [2004] is an intermediate approach which tries to improve the kinematic models by incorporating the most basic lessons learned from dynamic modeling.

## 4.7 Conclusions

We have computed synthetic near-field ground motion using a hybrid approach, where the rupture propagation is simulated by a boundary integral equation method (BIEM) and the wave-propagation is calculated using Green's functions from a discrete wavenumber / finite element method.

The horizontal peak ground velocity estimates obtained from this approach are generally in good agreement with the empirically derived attenuation relation by *Campbell* [1997]. Discrepancies are partially due to the computation method to obtain a single scalar PGV-estimate from the two horizontal components. The use of an orientation independent measure such as maximum vector amplitude or GMRotD50 as proposed by *Boore et al.* [2006] is therefore strongly suggested in future studies.

Compared to the empirical attenuation relation by *Campbell and Bozorgnia* [2003] the synthetic ground motions underestimate the spectral acceleration at short periods and show an acceptable agreement at periods longer than 1 s. We therefore conclude that at least for longer periods our modeling approach can be used to realistically simulate ground-motion characteristics of interest in engineering seismology and seismic hazard assessment.

The different factors contributing to ground-motion variability were separated by detailed analysis. We find that the ground-motion variability due to the stress heterogeneity is generally largest close to the fault and is largest in the backward directivity region for mostly unilateral rupture propagation. In all cases the intra-event variability due to directivity effects and the S-wave radiation pattern is on the order of or larger than the inter-event variability. When further separated, the part of the inter-event variability originating from the different hypocenter-station configuration is found to be larger than the part resulting from differences in the dynamic rupture process. In other words, in our current model the stress heterogeneity contributes more to ground-motion variability by determining the hypocenter location than it does by influencing the dynamic rupture process.

An analysis of the ground motion recordings of the 2004 Parkfield, California earthquake reveals that the PGV intra-event variability of this event is comparable to the intra-event variabilities of our synthetics. However, compared to the Parkfield dataset our simulations yield a spatial correlation of PGV values with a longer correlation length, which is likely due to the simplicity of the assumed crustal velocity model.

Overall, this study represents a step towards a physics-based estimation of future ground motion levels for purposes in seismic hazard assessment.

## Acknowledgments

We wish to thank E. Dunham, Harvard University, for providing his spectral boundary integral code. Banu Mena kindly supplied us with a script for the

computation of spectral acceleration. J.-P. Ampuero is supported by SPICE, a Marie Curie Research Training Network in the 6th Framework Program of the European Commission.

# Conclusions and Outlook

## Conclusions

Four analytical and numerical studies were presented that deal with the complexity of the earthquake source and its influence on the ground motion close to active faults. In particular we investigated the role of stress heterogeneity by changing the statistical characterization of the initial stress field in models of spontaneous earthquake rupture. In the following the main findings of the individual studies will be summarized.

In Chapter 1 we examine the validity of an efficient method to compute static stress changes from distributions of final slip using a Fourier spectral formulation of the relation between slip and stress [Andrews, 1980]. For multiple case studies we performed a comparison with the results obtained from analytical relations by Okada [1992]. The differences were found to be negligible for all practical purposes, while the computational efficiency was much higher for the spectral approach. Thus, the developed code constitutes a useful tool when efficiency is important, e. g. when performing static stress-change calculations for a large set of synthetic slip distributions.

In Chapter 2 we begin our investigation on the effect of spatially correlated random stress fields on the dynamic rupture process. Restricted to two-dimensional ruptures, this study provided tools and concepts guiding the interpretation of the three-dimensional rupture models in the following chapter. Based on concepts of fracture mechanics we developed a semi-dynamic model, which still contains all necessary ingredients to study the fundamental controls of stress heterogeneity on macroscopic source properties and frequency-size statistics of the events. In particular, we identified a transition in event size, driven by the amplitude of the stress heterogeneity. In terms of frequency-size statistics of seismicity, this transition corresponds to a change from Gutenberg-Richter type to characteristic earthquakes.

Chapter 3 is concerned with three-dimensional spontaneous ruptures in the presence of spatially correlated random stress fields. We observed a similar transition in event size controlled by the amplitude of the stress heterogeneity as in the 2D case. A distribution of different magnitudes could be obtained

within a narrow parameter range close to the transition. However, due to the increased computational demand of the 3D models the total number of simulated events was far less than for the 2D-ruptures and the frequency-size statistics could not be reliably determined.

Whereas the nucleation stage of the rupture in the heterogeneous stress field could be treated analytically in the 2D-case, it had to be solved for numerically in the 3D-case. We observed a common length scale of the nucleation patch irrespective of the chosen stress parameterization and an exponential growth of the moment-rate functions during the nucleation stage. Both observations are well in accord with other studies on nucleation under linear slip-weakening friction [e. g. *Campillo and Ionescu, 1997; Uenishi and Rice, 2003; Ampuero and Vilotte, 2007*].

Because of the increased complexity in 3D ruptures, further simplifying assumptions had to be made to construct a semi-dynamic model similar to the one in the previous chapter. Nevertheless, the final event size and the features of the transition were predicted reasonably well by the simplified 3D semi-dynamic model, making it a useful tool for the design of future scenario calculations.

Chapter 4 finally takes the important step from the rupture process to the resulting ground motions. We analyzed the characteristics of the synthesized seismograms and their variability in terms of different ground-motion parameters of engineering interest. We found that our synthetic seismograms are generally comparable to empirically derived attenuation relations, despite the simplifications in the model setup. However, the spectral acceleration at short periods is underestimated compared to empirical data.

A large part of the variability in the ground motion parameters is constituted by the intra-event variability due to the radiation pattern and strong directivity effects. Unless these sources of variability are accounted for explicitly, the total variability is likely to be dominated by the intra-event variability. The inter-event variability originates from the different hypocenter-station geometry and the complexity in the rupture process due to the stress heterogeneity. When the former source of variability is eliminated by fixing the hypocenter, the remaining variability is small compared to the other contributions. In the current modeling the stress heterogeneity therefore contributes more to the total ground-motion variability by determining the hypocenter position than by influencing the dynamic rupture process.

## Outlook

Through the different research stages we developed a profound understanding of the effects of stress heterogeneity on the properties of dynamic rupture and the resulting ground motion. Analytical descriptions and numerical tools have

been assembled which can guide future modeling of near-field ground motion scenarios for purposes in seismic hazard assessment.

However, the design of the current model aimed at unraveling fundamental principles rather than at delivering the most realistic scenario. Therefore there are aspects of the current dynamic model that can be made more realistic, before applying such modeling to real case studies.

The statistical parameters describing the stress heterogeneity in our dynamic models were chosen to coarsely sample the whole admissible parameter space. While some extreme parameter values yielding implausible results can probably be ruled out, it will become an important task to further constrain the statistical parameters from observations. Improved inversion techniques and good seismometer coverage in the near-field may enhance the resolution of static slip images, thus providing constraints on the static stress drop distribution. Small scale seismicity can provide estimates of stress heterogeneity, e. g. through studies of focal mechanisms [e. g. *Hardebeck, 2006; Smith, 2006*]. Heterogeneity of stress orientations can also be obtained from borehole breakouts, where recent deep research boreholes penetrating major fault systems will be of special importance [*Hickman and Zoback, 2004; Wu et al., 2007*].

As mentioned in Chapter 3, one of the major simplifications is the assumption of homogeneous friction properties and therefore homogenous fracture energy across the fault. It is now widely accepted that the fracture energy is scale-dependent, i. e. increases with the size of the rupture [e. g. *Ohnaka, 2003; McGarr et al., 2004; Mai et al., 2006*]. To consistently simulate earthquake ruptures over a broad range of magnitudes therefore requires an implementation of this scale-dependency. Several recently proposed approaches are outlined in the discussion section of Chapter 3 [*Aochi and Ide, 2004; Abercrombie and Rice, 2005; Andrews, 2005*]. However, as also noted in Chapter 3, the general result of the presence of a sharp, stress-dependent transition in event size is not expected to change with the inclusion of scale-dependent fracture energy. Irrespective of its scale dependency some random heterogeneity can be introduced into fracture energy. This is expected to increase the variability in rupture velocity and thus raise the ratio of radiated energy to moment, which in the present simulations has been found to be on the lower limit of values inferred for real events.

Another simplification is the use of a linear slip-weakening friction law. It lacks a description of fault healing, i. e. the regaining of strength of the material after the passing of the main rupture front. This behavior has been observed in laboratory friction experiments and has been shown to favor the generation of pulse-like rupture propagation. It has been proven practically impossible with our friction model to create pulses of rupture with the very short rise times proposed by *Heaton [1990]*. There is currently ongoing debate about the abundance of these pulses in observed earthquakes. In any case, an implementation of a healing mechanism is certainly expected to promote

pulse-like rupture propagation in the dynamic models.

Heterogeneity in the medium properties, which are neglected in the current model, may play an important role, both for the rupture process itself, but also for seismic wave propagation. In addition, for shallow ruptures the influence of the free surface can exert a feedback onto the rupture process through reflected waves. Both of the last two aspects may favor alternative numerical procedures like finite difference (FDM) or spectral element methods (SEM). Finally, it might be worth considering to replace the unbreakable barriers around the fault by more physical descriptions, such as low stress to resemble creeping regions or high (not infinite) fracture energy to mimic unruptured rock at a change in fault geometry.

Once the above mentioned aspects of the model have been addressed and the predicted ground motions have been validated against observations, the current approach is expected to show its full power in combination with the arising possibilities of high-performance computing. As a first line of research, specific scenarios for deterministic seismic hazard assessment can be envisioned, much like the current TERASHAKE efforts within the SCEC community [e. g. *Olsen et al.*, 2006], but with improved source models.

Apart from that, more generic scenarios can be designed to improve on the attenuation relations currently in use for seismic hazard assessment and engineering purposes. Many possible realizations of an earthquake with a given depth, size and faulting mechanism can be computed, enabling for example the study of the frequency- and magnitude-dependence of ground-motion variability. Increased insight is expected for the cases with few observational data, in particular the closest 10 km around the earthquake fault.

# Appendix A

## Static Loading Procedure

### A.1 Introduction

The question is to find the uniform increase in stress  $\tau_c^\infty$  (“critical load”), which drives a given heterogeneous stress distribution  $\tau_0(\underline{x})$  on a fault to the critical stage at the onset of dynamic instability. Once a point of the fault reaches the yield strength  $\tau_s$  of the material, it is allowed to slip. Since the rising of stress is assumed to occur slowly, slip on the fault is assumed to take place quasistatically, but nevertheless obeying the slip-weakening friction law. So for each infinitesimal increase in background stress, the effects of the uniform increase, the stress change due to slip and finally the strength drop due to slip have to be considered.

### A.2 Efficient Solution

The main idea for solving the task efficiently is to consider only the points of the numerical grid, which are currently slipping. Because then we can make use of the fact, that the problem is linear for a given set of slipping points  $I_\nu$  until  $\tau_s$  is reached by an additional point of the grid.

Inside the slipping zone  $I_\nu$  the stress is exactly balanced by friction:

$$\tau^\infty(t) + \tau_0(\underline{x}) + \mathcal{K}[\delta] = \tau_y - W\delta \quad (\text{A.1})$$

where  $\mathcal{K}[\delta]$  is the elastostatic stress distribution due to slip  $\delta(\underline{x}, t)$ . The operator  $\mathcal{K}[\cdot]$  is linear. The frictional sliding strength of the material is denoted  $\tau_y$  and  $W$  is the slip-weakening rate  $(\tau_s - \tau_y)/D_c$  with  $D_c$  being the critical slip-weakening distance. The incremental version is:

$$\Delta\tau^\infty + \mathcal{K}[\Delta\delta] = -W\Delta\delta \quad \text{inside } I_\nu \quad (\text{A.2})$$

After numerical discretization and rearranging we get

$$\Delta\tau^\infty + (K_\nu + W I_\nu) \Delta\delta_\nu = 0 \quad (\text{A.3})$$



where  $K_\nu$  and  $\Delta\delta_\nu$  denote the static stiffness matrix and the slip increment, respectively, for the  $N_\nu$  points belonging to  $I_\nu$ . As long as  $I_\nu$  is fixed, this is a linear system of  $N_\nu$  equations with  $N_\nu + 1$  unknowns,  $\Delta\tau^\infty$  and  $\Delta\delta_\nu$ . To obtain a well-defined (square) problem we must append an additional constraint. This can be done in various ways but the following choice leads to a symmetric square problem:

$$\Delta\delta_\nu \cdot \underline{1} = 1 \quad (\text{A.4})$$

In other terms we are prescribing the value of the increment of seismic potency ( $\Delta\text{potency} = \Delta x^2$ ). The complete linear problem is

$$\begin{pmatrix} K_\nu + W I_\nu & \underline{1} \\ \underline{1}^T & 0 \end{pmatrix} \begin{pmatrix} \Delta\delta_\nu^* \\ \Delta\tau_\infty^* \end{pmatrix} = \begin{pmatrix} 0 \\ 1 \end{pmatrix} \quad (\text{A.5})$$

We have added a \* superscript to highlight that the solution  $(\Delta\delta_\nu^*, \Delta\tau_\infty^*)$  corresponds to an arbitrarily prescribed value of potency increment. This solution can be rescaled by an arbitrary multiplicative factor  $\lambda$ . The physical value of  $\lambda$  is ultimately determined according to some additional constraint, in our case that the stress outside  $I_\nu$  remains below  $\tau_s$  for a positive  $\Delta\tau^\infty$ .

### A.3 The Algorithm

The algorithm is currently implemented as a Matlab function and consists of the following steps:

1. Find the set of points  $I_\nu$ , where either (a) stress has reached  $\tau_s$ :

$$\tau \geq \tau_s$$

and/or (b) slip is already taking place:

$$\delta > 0$$

2. Build  $K_\nu$ , the static stiffness matrix for the set of slipping points  $I_\nu$ . It is a  $N_\nu \times N_\nu$  matrix, where  $N_\nu$  is the number of elements of  $I_\nu$ . This step involves computation of the static stress change due to a unit increase in slip at a single grid point. Here the algorithm makes use of the efficient spectral formulation discussed earlier in Chapter 1.
3. Solve matrix equation (A.5) for  $\Delta\delta_\nu^*$  and  $\Delta\tau_\infty^*$
4. If  $\Delta\tau_\infty^* \leq 0$ , exit the algorithm and report the  $\tau^\infty$  reached so far as the critical value  $\tau_c^\infty$ . Else go on with steps 5-7
5. Compute the stress change  $\Delta\tau^*$  for the increment  $\Delta\tau_\infty^*$  of background stress, including the redistribution of stress due to slip:

$$\Delta\tau^* = \Delta\tau_\infty^* \underline{1} + K \Delta\delta^* \quad (\text{A.6})$$

where now  $\underline{1}$  is a  $N \times 1$  column vector of ones (with  $N$  being the total number of points in the grid),  $K$  is the total  $N \times N$  stiffness matrix and  $\Delta\delta^*$  is a  $N \times 1$  vector with the values of  $\Delta\delta_\nu^*$  at the points of  $I_\nu$  and zero everywhere else. Again we make use of the spectral formulation of Chapter 1 relating static stress changes to a slip distribution. This circumvents the need to construct the large matrix  $K$ , but allows to do the computation efficiently by employing the Fast Fourier Transform (FFT).

6. Determine the (scalar) multiplicative factor  $\lambda$  from two additional constraints: The first constraint is that the new traction values  $\tau_{\text{new}} = \tau + \lambda \cdot \Delta\tau^*$  outside  $I_\nu$  must not exceed  $\tau_s$ , i.e.  $\tau_{\text{new}} \leq \tau_s$ :

$$\lambda_{\text{stress}} = \min_{\oplus} \left[ \frac{\tau_s - \tau}{\Delta\tau^*} \right]_{\text{outside } I_\nu} \quad (\text{A.7})$$

Here the  $\oplus$  indicates that the minimum is taken only of the positive values of the expression in brackets, whereas the negative values are ignored.

The second constraint is that the new slip  $\delta_{\text{new}} = \delta + \lambda \cdot \Delta\delta^*$  should not exceed  $D_c$  in those points, that have slip  $\delta$  between  $0 < \delta < D_c$ , i.e.:

$$\lambda_{\text{slip}} = \min_{\oplus} \left[ \frac{D_c - \delta}{\Delta\delta_\nu^*} \right]_{\text{inside } I_\nu, \delta < D_c} \quad (\text{A.8})$$

And for the actual factor  $\lambda$  the minimum of the values given by equations (A.7) and (A.8) is taken.

7. (a) Update the values of stress and slip

$$\begin{aligned} \tau_{\text{new}} &= \tau + \lambda \cdot \Delta\tau^* \\ \delta_{\text{new}} &= \delta + \lambda \cdot \Delta\delta^*, \end{aligned} \quad (\text{A.9})$$

- (b) keep track of the total increase in background stress

$$\tau_{\text{new}}^\infty = \tau^\infty + \lambda \cdot \Delta\tau_\infty^*, \quad (\text{A.10})$$

(c) set the slip-weakening rate to  $W = 0$  for all points which now have  $\delta \geq D_c$  and (d) finally start over at step one with the newly obtained values.



# Appendix B

## Addendum to Chapter 3

This section contains some additional investigations, which are not part of the published manuscript *Ripperger et al.* [2007], but thematically belong to Chapter 3. Here I examine the consistency of slip and stress in simulations in terms of the spectral properties and previously published works.

### B.1 Spectra of Slip

Our quantification of stress heterogeneity was inspired by spectral analyzes of slip distributions inferred for real earthquakes [*Mai and Beroza, 2002*]. Therefore it is interesting to study the spectral characteristics of the final slip distributions resulting from our dynamic models.

To estimate the spectral decay at high wave numbers we do not attempt to fit the slip spectra with a specific auto-correlation function, but rather compare the spectra visually with reference lines of different slopes in a double logarithmic plot. The small events (i.e., those not reaching the boundaries) always show a steep spectral falloff of approximately  $\propto k^{-2.5}$  to  $\propto k^{-3}$  (Figure B.1), indicating smooth slip distributions. Note that in the stochastic source model of *Andrews* [1980] the coherent part of the slip distribution was also assumed to have a smooth shape and a falloff proportional to  $k^{-3}$ . For the stochastic part of slip, *Andrews* finds the spectral decay to be  $\propto k^{-\nu-1}$ , if the spectrum of initial stress decays as  $\propto k^{-\nu}$ .

At first glance, the final slip distributions of our whole-fault events seem to contradict this model prediction. For all large events spreading the whole fault, the slip spectra decay proportional to  $k^{-1.5}$ , irrespective of the imposed spectrum of the initial stress. This decay with  $k^{-1.5}$  is much gentler than for the small events and also gentler than for the analytical solution for a static circular crack ( $\propto k^{-2}$ ). At closer inspection, we found small discontinuities in slip at the fault edges, which are likely to cause the observed large high-wavenumber content of the spectra.

In a second analysis we estimate the spectra of the full-fault events only for

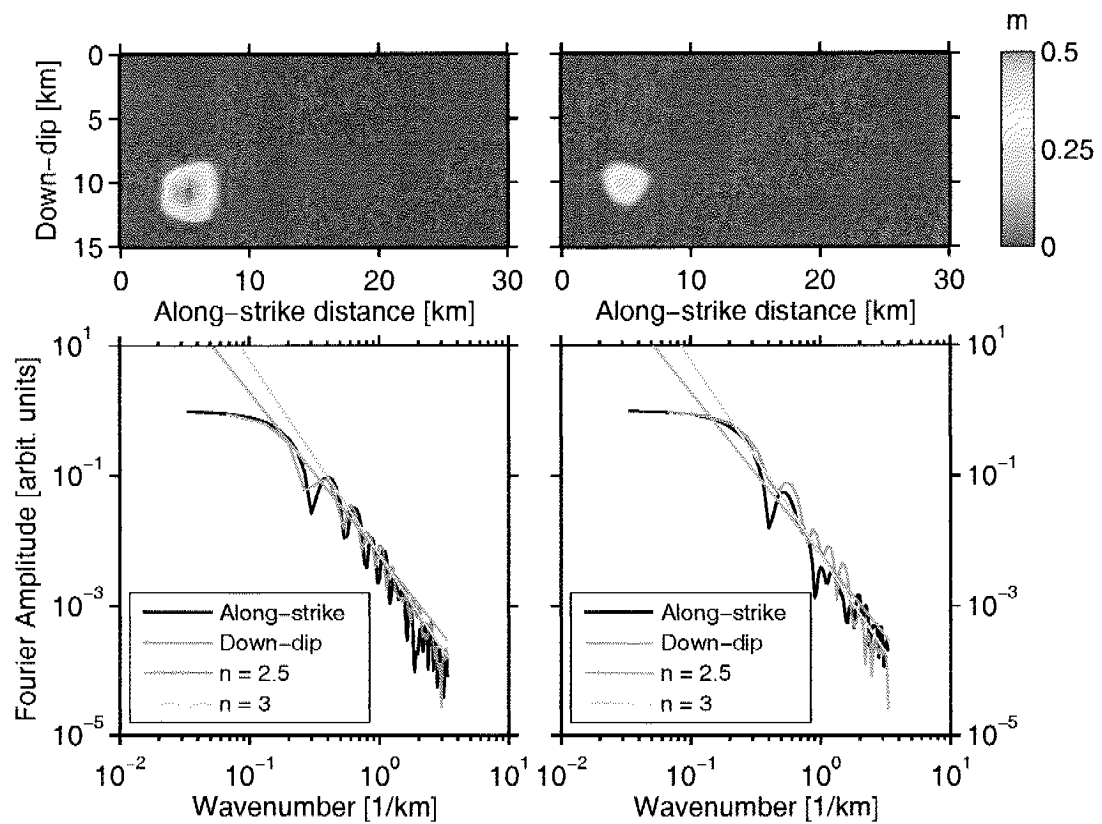


**Figure B.1:** Typical examples of slip distributions (upper panels) of small events and the associated amplitude spectra (lower panels). The reference lines are drawn for a decay of  $\propto k^{-2.5}$  and  $\propto k^{-3}$ .

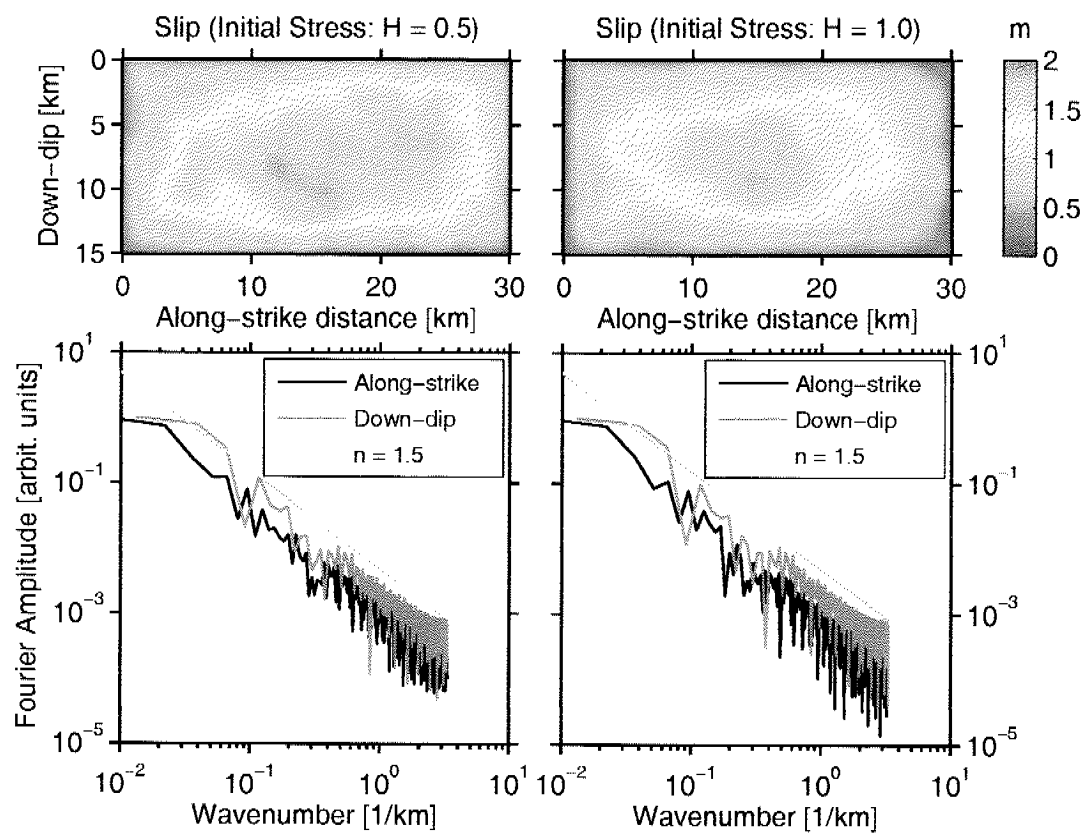


**Figure B.2:** Typical examples of slip distributions (upper panels) of whole fault events and their amplitude spectra (lower panels). Reference lines (in cyan) are drawn for a decay of  $\propto k^{-1.5}$ .

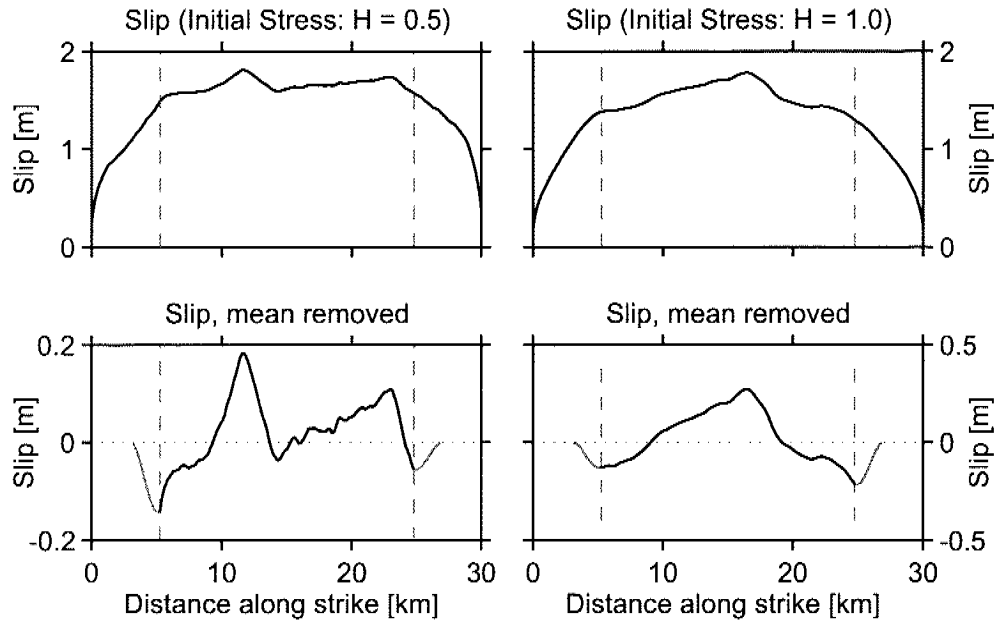


**Figure B.3:** Illustration of extraction of the interior of slip distributions. Shown are one-dimensional slices through the original slip distributions (upper panels) of whole fault events. Vertical dashed lines mark the points of truncation. The lower panels show the remaining interior of the slip distributions with its mean removed (black lines) and the added taper towards zero with a width of 14 grid points (gray lines).

the interior of the fault. This analysis aims at separating the stochastic part of the slip distribution from the coherent part that is mainly determined by the fixed fault size. As illustrated in Figure B.3, to retain the center of the slip distribution where the coherent part is approximately constant we have to remove the outermost grid points at each side of the fault plane where slip is dropping off steeply. We choose to remove 35 grid points on each side, but the results are similar for slightly larger or smaller values of roughly 30 to 40 points being cut off. From the remaining slip distribution we subtract its mean value and finally add a tapering towards zero (Hanning function) of 14 grid points width (Figure B.3). Testing shows that the particular choice of the width of this tapering zone does not have a strong influence on the general results as long as it is larger than 10 grid points. The resulting spectra are oscillating more than before, making it difficult to determine a unique slope of the spectral decay. Nevertheless, tentative spectral falloffs can be obtained that are clearly different from the previous analysis of the whole slip distributions. The spectral decay is generally steeper than  $k^{-1.5}$  and ranges roughly from  $k^{-2}$  to  $k^{-3}$  for initial stress distributions characterized by  $k^{-1}$  to  $k^{-2}$ . Thus the spectra of the interior of the slip distributions appear to be in accord with  $\propto k^{-\nu-1}$  as predicted by *Andrews* [1980]. In contrast, the spectra computed over the whole fault are dominated by the behavior of the slip distributions at

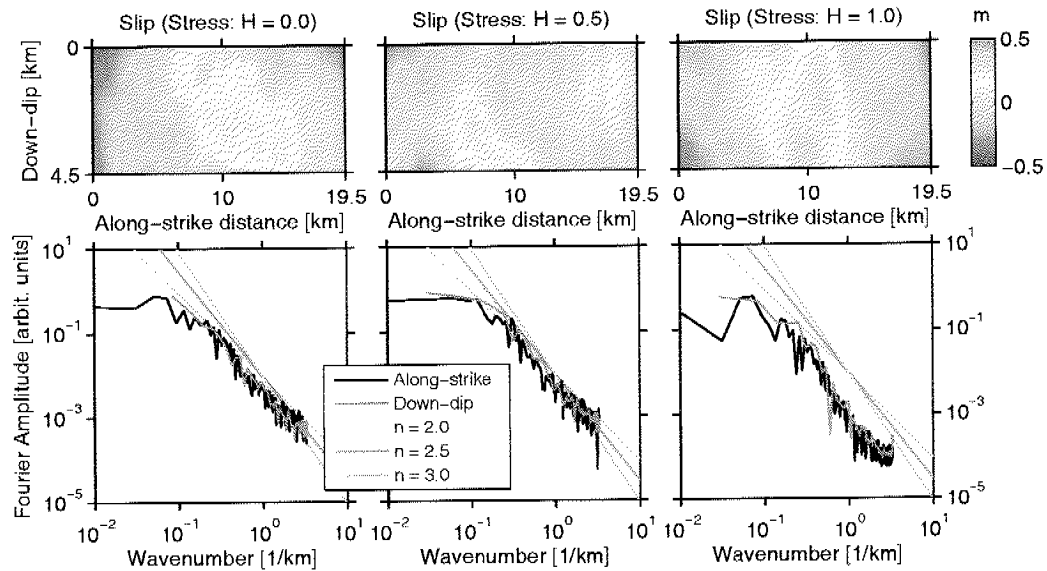


**Figure B.4:** Typical spectra of the interior of slip distributions of whole-fault events. The cut slip distributions are displayed in the top row for examples with varying Hurst exponent  $H$  of the initial stress distribution. Note that the mean of the slip distributions was removed, so the distributions contain both positive and negative values. The spectra for each example are shown in the bottom row along with reference lines for decays  $\propto k^{-2}$ ,  $\propto k^{-2.5}$  and  $\propto k^{-3}$ .

the artificial fault boundaries.

## B.2 Stress Change

The stress changes on the fault plane computed from the slip distributions using the spectral formulation of *Andrews* [1980] (see Chapter 1) are almost identical to the direct evaluation of stress changes by subtracting the initial stress distribution from the final stress distribution (Figure B.5). The following two patterns can be identified in the stress change differences: (a) The largest deviations (generally negative) occur at the fault boundaries. These differences most likely originate from the artificially imposed fault boundaries in the dynamic computation, because they do not appear for the simulations without the unbreakable boundaries. (b) In some cases (for example in the right column in Figure B.5) one can observe the effect of small stress waves travelling across the fault plane, even after all points stopped slipping. These stress waves typically show up as positive differences in Figure B.5. Overall, both absolute differences are generally less than 1.5 MPa, equal to less than 10% of the maximum change in stress. For most practical purposes, the differences in the stress change computations are therefore of minor importance.



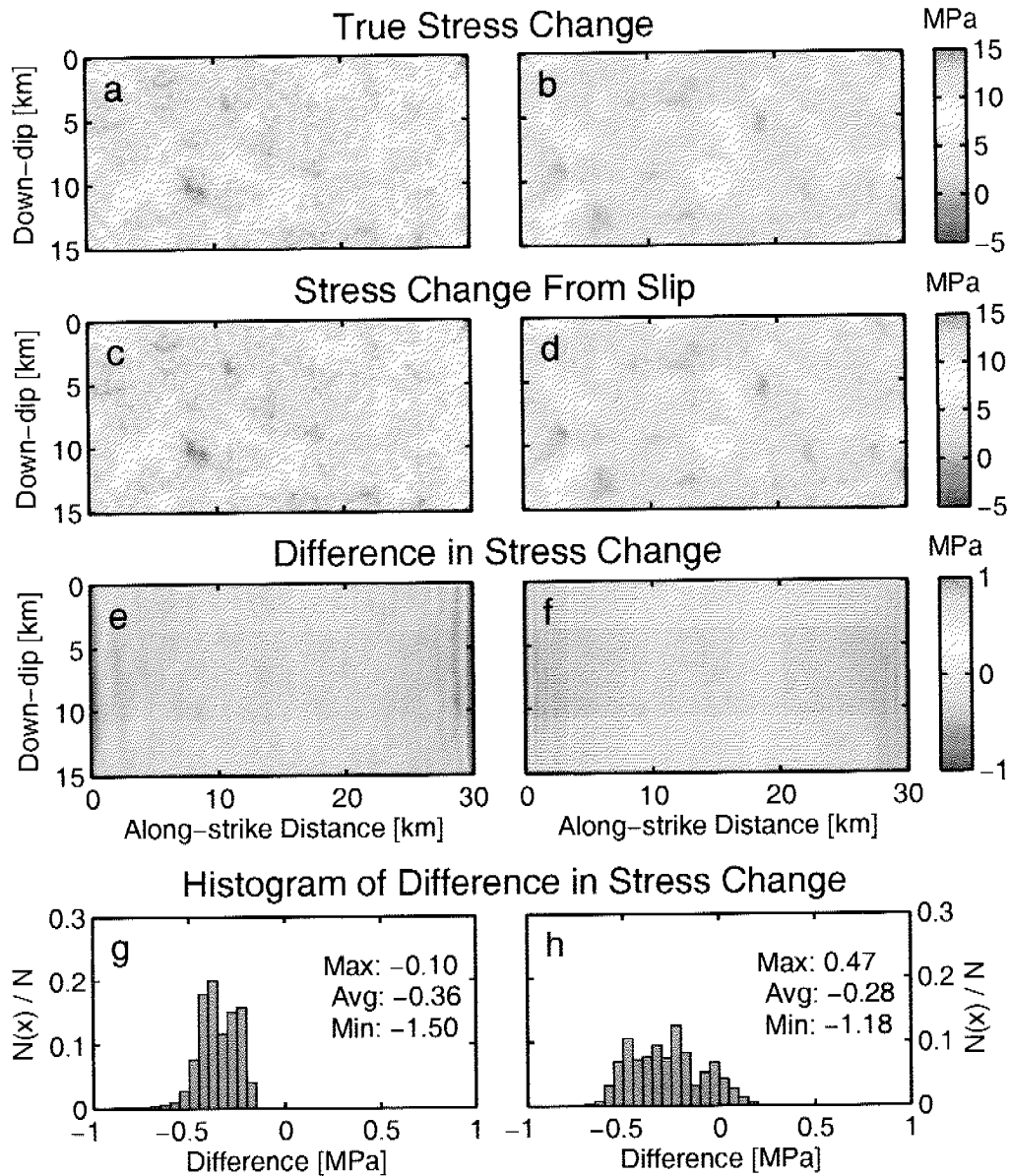


**Figure B.5:** Differences in stress change calculations for two examples with initial stress characterized by  $H = 0.5$  (left column) and  $H = 1$  (right column). Panels (a) and (b) show the stress change computed by subtracting the initial stress from the final stress distribution. Panels (c) and (d) show the stress change evaluated from the final slip distribution with the spectral formulation of *Andrews* [1980]. The difference between the two stress change results is always computed as the stress change estimated from slip minus the true stress change. It is mapped in panels (e) and (f) and histograms of it are plotted in panels (g) and (h). Overall, the plots illustrate that the stress change computed from the slip distribution consistently underestimate the true stress change, but generally by a small fraction of less than 10%.

# List of Tables

3.1	General modeling parameters used in all dynamic rupture simulations. . . . .	41
4.1	Model parameters of all dynamic rupture simulations of <i>Ripperger et al.</i> [2007]. . . . .	73
4.2	Stress field parameters and averaged macroscopic properties of the selected dynamic rupture simulations from <i>Ripperger et al.</i> [2007]. . . . .	75
4.3	Coordinates of receiver locations at which ground motions are computed. . . . .	78
4.4	Residuals of peak ground velocity, estimated on the synthetic seismograms. . . . .	85
4.5	Residuals of spectral acceleration at 1 s period estimated on the synthetic seismograms. . . . .	93

Seite Leer /  
Blank leaf

# List of Figures

1.1	Comparison of calculation time of static slip to stress conversion methods. . . . .	14
1.2	Slip distribution and computed stress changes for the 1984 Morgan Hill, California, earthquake. . . . .	17
1.3	Slip distribution and computed stress changes for the 1994 Northridge, California, earthquake. . . . .	18
1.4	Slip distribution and stress changes computed for the 1989 Loma Prieta, California, earthquake. . . . .	19
2.1	Frequency-size statistics in the semi-dynamic model. . . . .	26
2.2	Initial stress distribution, ensemble-averaged stress intensity factor, total energy change as a function of crack size and crack length corresponding to mean-field equilibria as a function of <i>std.</i> . . . . .	27
2.3	Apparent stress drop and apparent stress. . . . .	29
2.4	Example rupture models with different amplitude of the stress heterogeneity and dependence of rupture area on fault-average stress drop. . . . .	31
3.1	Geometry of the problem and linear slip-weakening law. . . . .	37
3.2	Illustration of random stress field generation. . . . .	39
3.3	Dependence of critical load on stochastic stress parameters. . . . .	43
3.4	Dependence of average stress level on Hurst exponent. . . . .	44
3.5	Characterization of triggering patches by circumscribed and inscribed circles. . . . .	45
3.6	Moment rate functions and their dominant frequency during seismic nucleation. . . . .	47
3.7	Snapshots of slip velocity on the fault plane for typical examples of crack-like and pulse-like propagation. . . . .	49
3.8	Rupture front contours for three examples with different average stress level. . . . .	50
3.9	Stress-dependent size transition. Shown is the dependence of rupture area on average stress level. . . . .	51
3.10	Scaling of rupture area with seismic moment. . . . .	52
3.11	Scaling of radiated energy with seismic moment. . . . .	53
3.12	Typical examples of moment rate functions. . . . .	54

3.13	Spectra of moment rate functions for the examples of Figure 3.12. . . . .	55
3.14	Corner frequency and falloff exponent of moment rate spectra. . . . .	55
3.15	Validation of loading procedure. . . . .	63
4.1	Final slip distributions and rupture front contours of the selected dynamic rupture simulations from <i>Ripperger et al.</i> [2007]. . . . .	74
4.2	Initial stress and final slip distributions, rupture front contours and slip-velocity functions of 10 out of the 30 additional runs with fixed hypocenter. . . . .	76
4.3	Map-view of station configuration specified in Table 4.3. . . . .	78
4.4	Side-view of the fault plane and the locations of the hypocenters. . . . .	79
4.5	Example of a bilateral event. Map of horizontal PGV values (GMRotD50) and seismograms of the receiver ring at $r_{jb} \approx 60$ km. . . . .	81
4.6	Example of a unilateral event. Map of horizontal PGV values (GMRotD50) and seismograms of the receiver ring at $r_{jb} \approx 60$ km. . . . .	82
4.7	Comparison of PGV values of all 61 events of Fig. 4.1 with the empirical attenuation relation of <i>Campbell</i> [1997]. . . . .	83
4.8	Distribution of residuals of horizontal PGV (GMRotD50) at each distance range. . . . .	86
4.9	PGV residuals for single stations along receiver rings for all 61 events of Fig. 4.1. . . . .	87
4.10	PGV residuals for single stations along receiver rings for the 30 simulations with fixed hypocenter. . . . .	89
4.11	Comparison of horizontal spectral acceleration with the empirical attenuation relation of <i>Campbell and Bozorgnia</i> [2003]. . . . .	91
4.12	Distribution of residuals for horizontal spectral acceleration. . . . .	92
4.13	PGV intra-event variability of the Parkfield event. . . . .	94
4.14	Standard deviation of the difference of $\ln(\text{PGV})$ for all station pairs versus interstation distance. . . . .	97
B.1	Typical examples of slip distributions of small events and their amplitude spectra. . . . .	110
B.2	Typical examples of slip distributions of whole fault events and their amplitude spectra. . . . .	111
B.3	Illustration of extraction of the interior of slip distributions for separate spectral analysis. . . . .	112
B.4	Spectra of the inner part of slip distributions of whole-fault events. . . . .	113
B.5	Differences in stress change calculations. . . . .	114

# Bibliography

- Aagaard, B. T., J. F. Hall, and T. H. Heaton (2001), Characterization of near-source ground motions with earthquake simulations, *Earthquake Spectra*, *17*(2), 177–207.
- Aagaard, B. T., J. F. Hall, and T. H. Heaton (2004), Effects of fault dip and slip rake angles on near-source ground motions: Why rupture directivity was minimal in the 1999 Chi-Chi, Taiwan, earthquake, *B. Seismol. Soc. Am.*, *94*(1), 155–170.
- Abercrombie, R. E. (1995), Earthquake source scaling relationships from -1 to 5  $M_L$  using seismograms recorded at 2.5-km depth, *J. Geophys. Res.*, *100*(B12), 24,015–24,036.
- Abercrombie, R. E., and J. R. Rice (2005), Can observations of earthquake scaling constrain slip-weakening?, *Geophys. J. Int.*, *162*, 406–424, doi:10.1111/j.1365-246X.2005.02579.x.
- Abrahamson, N. A., and W. J. Silva (1997), Empirical response spectral attenuation relations for shallow crustal earthquakes, *Seis. Res. Lett.*, *68*(1), 94–127.
- Aki, K. (1968), Seismic displacements near a fault, *J. Geophys. Res.*, *73*, 5359–5376.
- Aki, K., and P. G. Richards (2002), *Quantitative Seismology*, 2nd ed., University Science Books, Sausalito, California.
- Allen, R. M., and H. Kanamori (2003), The potential for earthquake early warning in Southern California, *Science*, *300*, 786–789.
- Ambraseys, N. N., J. Douglas, S. K. Sarma, and P. M. Smit (2005), Equations for the estimation of strong ground motions from shallow crustal earthquakes using data from Europe and the Middle East: Horizontal peak ground acceleration and spectral acceleration, *Bull. Earthquake Eng.*, doi: 10.1007/s10518-005-0183-0.
- Ampuero, J. P., and J. P. Vilotte (2003), Effective fault friction and seismic nucleation phase: Scale-dependent or non-linear friction?, *Geophysical Research Abstracts*, *5*, 11,288.

- Ampuero, J. P., and J. P. Vilotte (2007), Insights on fault friction from seismic nucleation phases: scale-dependent or non-linear slip weakening?, *in preparation*.
- Ampuero, J. P., J. P. Vilotte, and F. J. Sánchez-Sesma (2002), Nucleation of rupture under slip dependent friction law: Simple models of fault zone, *J. Geophys. Res.*, *107*(B12), doi:10.1029/2001JB000452.
- Ampuero, J. P., J. Ripperger, and P. M. Mai (2006), Properties of dynamic earthquake ruptures with heterogeneous stress drop, in *Earthquakes: Radiated energy and the physics of faulting*, *Geophysical Monograph Series*, vol. 170, edited by R. Abercrombie, A. McGarr, and H. Kanamori, pp. 255–261, AGU.
- Andrews, D. J. (1974), Evaluation of static stress on a fault plane from a Green's function, *B. Seismol. Soc. Am.*, *64*(6), 1629–1633.
- Andrews, D. J. (1978), Coupling of energy between tectonic processes and earthquakes, *J. Geophys. Res.*, *83*(B5), 2259–2264.
- Andrews, D. J. (1980), A stochastic fault model 1. Static case, *J. Geophys. Res.*, *85*(B7), 3867–3877.
- Andrews, D. J. (1981), A stochastic fault model 2. Time-dependent case, *J. Geophys. Res.*, *86*(11), 10,821–10,834.
- Andrews, D. J. (2005), Rupture dynamics with energy loss outside the slip zone, *J. Geophys. Res.*, *110*, B01307, doi:10.1029/2004JB003191.
- Aochi, H., and J. Douglas (2006), Testing the validity of simulated strong ground motion from the dynamic rupture of a finite fault, by using empirical equations, *Bull. Earthquake Eng.*, *4*, 211–229, doi:10.1007/s10518-006-0001-3.
- Aochi, H., and S. Ide (2004), Numerical study on multi-scaling earthquake rupture, *Geophys. Res. Lett.*, *31*, L02606, doi:10.1029/2003GL018708.
- Archuleta, R. J., and G. A. Frazier (1978), Three-dimensional numerical simulations of dynamic faulting in a half-space, *B. Seismol. Soc. Am.*, *68*(3), 541–572.
- Beroza, G. C. (1991), Near-source modeling of the Loma Prieta earthquake: Evidence for heterogeneous slip and implications for earthquake hazard, *B. Seismol. Soc. Am.*, *81*(5), 1603–1621.
- Beroza, G. C., and T. Mikumo (1996), Short slip duration in dynamic rupture in the presence of heterogeneous fault properties, *J. Geophys. Res.*, *101*(B10), 22,449–22,460.

- Beroza, G. C., and P. Spudich (1988), Linearized inversion for fault rupture behavior; application to the 1984 Morgan Hill, California, earthquake, *J. Geophys. Res.*, *93*(6), 6275–6296.
- Beyer, K., and J. J. Bommer (2006), Relationships between median values and between aleatory variabilities for different definitions of the horizontal component of motion, *B. Seismol. Soc. Am.*, *96*(4A), 1512–1522, doi:10.1785/0120050210.
- Boatwright, J., and H. Quin (1986), The seismic radiation from a 3-D dynamic model of a complex rupture process: Part I, Confined ruptures, in *Earthquake source mechanics, Geophysical Monographs*, vol. 37, edited by S. Das, J. Boatwright, and C. H. Scholz, pp. 97–109, American Geophysical Union, Washington.
- Boatwright, J., K. Thywissen, and L. C. Seekins (2001), Correlation of ground motion and intensity for the 17 January 1994 Northridge, California, earthquake, *B. Seismol. Soc. Am.*, *91*(4), 739–752.
- Boore, D. M., W. B. Gibbs, W. B. Joyner, J. C. Tinsley, and D. J. Ponti (2003), Estimated ground motion from the 1994 Northridge, California, earthquake at the site of the Interstate 10 and La Cienega Boulevard bridge collapse, West Los Angeles, California, *B. Seismol. Soc. Am.*, *93*(6), 2737–2751.
- Boore, D. M., J. Watson-Lamprey, and N. A. Abrahamson (2006), Orientation-independent measures of ground motion, *B. Seismol. Soc. Am.*, *96*(4A), 1502–1511, doi:10.1785/0120050209.
- Bouchbinder, E., D. Kessler, and I. Procaccia (2004), Crack-microcrack interactions in dynamical fracture, *Phys. Rev. E*, *70*(4), Art. No. 046107.
- Bouchbinder, E., J. Mathiesen, and I. Procaccia (2005), Branching instabilities in rapid fracture: Dynamics and geometry, *Phys. Rev. E*, *71*(5), Art. No. 056118.
- Bouchon, M. (1997), The state of stress on some faults of the San Andreas system as inferred from near-field strong motion data, *J. Geophys. Res.*, *102*(B6), 11,731–11,744.
- Brunc, J. N. (1970), Tectonic stress and the spectra of seismic shear waves from earthquakes, *J. Geophys. Res.*, *75*(26), 4997–5009.
- Campbell, K. W. (1997), Empirical near-source attenuation relationships for horizontal and vertical components of peak ground acceleration, peak ground velocity, and pseudo-absolute acceleration response spectra, *Seis. Res. Lett.*, *68*(1), 154–179.



- Campbell, K. W. (2000), Erratum: "Empirical near-source attenuation relationships for horizontal and vertical components of peak ground acceleration, peak ground velocity, and pseudo-absolute acceleration response spectra", *Seis. Res. Lett.*, 71(3), 352–354.
- Campbell, K. W. (2001), Erratum: "Empirical near-source attenuation relationships for horizontal and vertical components of peak ground acceleration, peak ground velocity, and pseudo-absolute acceleration response spectra", *Seis. Res. Lett.*, 72(4), 474.
- Campbell, K. W., and Y. Bozorgnia (2003), Updated near-source ground-motion (attenuation) relations for the horizontal and vertical components of peak ground acceleration and acceleration response spectra, *B. Seismol. Soc. Am.*, 93(1), 314–331.
- Campillo, M., and I. R. Ionescu (1997), Initiation of antiplane shear instability under slip dependent friction, *J. Geophys. Res.*, 102, 20,363–20,371.
- Chopra, A. K. (2001), *Dynamics of structures: Theory and applications to earthquake engineering*, International series in civil engineering and engineering mechanics, 2nd ed., Prentice Hall, New Jersey.
- Cochard, A., J. P. Ampuero, and J. Schmittbuhl (2006), Seismic nucleation under nonlinear slip weakening friction, *Geophys. Res. Abstr.*, 8, EGU06-A-07176.
- Cochran, E. S., J. E. Vidale, and S. Tanaka (2004), Earth tides can trigger shallow thrust fault earthquakes, *Science*, 306, 1164–1166, doi:10.1126/science.1103961.
- Dahlen, F. A. (1974), On the ratio of P-wave to S-wave corner frequencies for shallow earthquake sources, *B. Seismol. Soc. Am.*, 64(4), 1159–1180.
- Day, S. M. (1982), Three-dimensional simulation of spontaneous rupture: The effect of nonuniform prestress, *B. Seismol. Soc. Am.*, 72(6), 1881–1902.
- Day, S. M., G. Yu, and D. J. Wald (1998), Dynamic stress changes during earthquake rupture, *B. Seismol. Soc. Am.*, 88(2), 512–522.
- Delouis, B., D. Giardini, P. Lundgren, and J. Salichon (2002), Joint inversion of InSAR, GPS, teleseismic, and strong-motion data for the spatial and temporal distribution of earthquake slip: Application to the 1999 Izmit mainshock, *B. Seismol. Soc. Am.*, 92(1), 278–299.
- Dunham, E. M. (2005), Dissipative interface waves and the transient response of a three-dimensional sliding interface with Coulomb friction, *J. Mech. Phys. Sol.*, 53, 327–357, doi:10.1016/j.jmps.2004.07.003.

- Dyskin, A. V. (1999), On the role of stress fluctuations in brittle fracture, *Int. J. Fracture*, *100*, 29–53.
- Fabrikant, V. I. (1989), *Applications of potential theory in mechanics*, Kluwer Academic Publishers, Dordrecht.
- Favreau, P., and R. J. Archuleta (2003), Direct seismic energy modeling and application to the 1979 Imperial Valley earthquake, *Geophys. Res. Lett.*, *30*(5), doi:10.1029/2002GL015968.
- Favreau, P., M. Campillo, and I. R. Ionescu (2002), Initiation of shear instability in three-dimensional elastodynamics, *J. Geophys. Res.*, *107*(B7), 2147, doi:10.1029/2001JB000448.
- Fletcher, J. B., L. M. Baker, P. Spudich, P. Goldstein, J. D. Sims, and M. Hellweg (1992), The USGS Parkfield, California, dense seismograph array: UPSAR, *B. Seismol. Soc. Am.*, *82*(2), 1041–1070.
- Fletcher, J. B., P. Spudich, and L. M. Baker (2006), Rupture propagation of the 2004 Parkfield, California, earthquake from observations at the UPSAR, *B. Seismol. Soc. Am.*, *96*(4B), S129–S142, doi:10.1785/0120050812.
- Frankel, A. (1991), High-frequency spectral falloff of earthquakes, fractal dimension of complex rupture, b value, and the scaling of strength on faults, *J. Geophys. Res.*, *96*(B4), 6291–6302.
- Freund, L. B. (1998), *Dynamic fracture mechanics*, Cambridge University Press, Cambridge, U.K.
- Fukuyama, E., and R. Madariaga (2000), Dynamic propagation and interaction of a rupture front on a planar fault, *Pure Appl. Geophys.*, *157*, 1959–1979.
- Futterman, W. I. (1962), Dispersive body waves, *J. Geophys. Res.*, *67*(13), 5279–5291.
- Gallovic, F., and J. Brokesova (2004), On strong ground motion synthesis with  $k^{-2}$  slip distributions, *J. Seismol.*, *8*, 211–224.
- Geubelle, P. H., and J. R. Rice (1995), A spectral method for three-dimensional elastodynamic fracture problems, *J. Mech. Phys. Sol.*, *43*(11), 1791–1824.
- Graves, R., and A. Pitarka (2004), Broadband time history simulation using a hybrid approach, in *Proceedings of the 13<sup>th</sup> World Conference on Earthquake Engineering, Vancouver, B.C., Canada*, Paper No. 1098.
- Graves, R. W. (1998), Three-dimensional Finite-Difference modeling of the San Andreas fault: Source parameterization and ground-motion levels, *B. Seismol. Soc. Am.*, *88*(4), 881–897.

- Guatteri, M., and P. Spudich (2000), What can strong-motion data tell us about slip-weakening fault-friction laws?, *B. Seismol. Soc. Am.*, *90*, 98–116.
- Guatteri, M., P. M. Mai, G. C. Beroza, and J. Boatwright (2003), Strong ground-motion prediction from stochastic-dynamic source models, *B. Seismol. Soc. Am.*, *93*(1), 301–313.
- Guatteri, M., P. M. Mai, and G. C. Beroza (2004), A pseudo-dynamic approximation to dynamic rupture models for strong ground motion prediction, *B. Seismol. Soc. Am.*, *94*(6), 2051–2063.
- Hardebeck, J. L. (2006), Homogeneity of small-scale earthquake faulting, stress, and fault strength, *B. Seismol. Soc. Am.*, *96*(5), 1675–1688, doi:10.1785/0120050257.
- Hartzell, S., P. Liu, and C. Mendoza (1996), The 1994 Northridge, California, earthquake: Investigation of rupture velocity, risetime, and high-frequency radiation, *J. Geophys. Res.*, *101*(B9), 20,091–20,108.
- Hartzell, S. H., and T. H. Heaton (1983), Inversion of strong-ground motion and teleseismic waveform data for the fault rupture history of the 1979 Imperial Valley, California, earthquake, *B. Seismol. Soc. Am.*, *73*, 1553–1583.
- Haskell, N. (1969), Elastic displacements in the near-field of a propagating fault, *B. Seismol. Soc. Am.*, *59*(2), 865–908.
- Heaton, T. H. (1990), Evidence for and implications of self-healing pulses of slip in earthquake rupture, *Phys. Earth Planet. Inter.*, *64*, 1–20.
- Heimpel, M. (1996), Earthquake size-frequency relations from an analytical stochastic rupture model, *J. Geophys. Res.*, *101*(B10), 22,435–22,448.
- Heimpel, M., and P. Malin (1998), Aseismic slip in earthquake nucleation and self-similarity: Evidence from Parkfield, California, *Earth Planet. Sci. Lett.*, *157*, 249–254.
- Herrero, A., and P. Bernard (1994), A kinematic self-similar rupture process for earthquakes, *B. Seismol. Soc. Am.*, *84*(4), 1216–1228.
- Hickman, S., and M. Zoback (2004), Stress orientations and magnitudes in the SAFOD pilot hole, *Geophys. Res. Lett.*, *31*, L15S12, doi:10.1029/2004GL020043.
- Hillers, G., Y. Ben-Zion, and P. M. Mai (2006), Seismicity on a fault controlled by rate-and-state dependent friction with spatial variation of the critical slip distance, *J. Geophys. Res.*, *111*, B01403, doi:10.1029/2005JB003859.

- Hillers, G., P. M. Mai, Y. Ben-Zion, and J. P. Ampuero (2007), Statistical properties of seismicity of fault zones at different evolutionary stages, *Geophys. J. Int.*, doi:10.1111/j.1365-246X.2006.03275.x.
- Husseini, M. I., and M. J. Randall (1976), Rupture velocity and radiation efficiency, *B. Seismol. Soc. Am.*, 66(4), 1173–1187.
- Husseini, M. I., D. B. Jovanovich, M. J. Randall, and L. B. Freund (1975), The fracture energy of earthquakes, *Geophys. J. R. Astron. Soc.*, 43, 367–385.
- Ide, S., and H. Aochi (2005), Earthquakes as multiscale dynamic ruptures with heterogeneous fracture surface energy, *J. Geophys. Res.*, 110, B11303, doi:10.1029/2004JB003591.
- Ide, S., and M. Takeo (1997), Determination of constitutive relations of fault slip based on seismic wave analysis, *J. Geophys. Res.*, 102(B12), 27,379–27,391.
- Inoue, T., and T. Miyatake (1998), 3D simulation of near-field strong ground motion based on dynamic modeling, *B. Seismol. Soc. Am.*, 88(6), 1445–1456.
- Johnson, E. (1990), On the initiation of unidirectional slip, *Geophys. J. Int.*, 101, 125–132.
- Kanamori, H., and D. L. Anderson (1975), Theoretical basis of some empirical relations in seismology, *B. Seismol. Soc. Am.*, 65, 1073–1095.
- Kanamori, H., and E. Brodsky (2004), The physics of earthquakes, *Rep. Prog. Phys.*, 67, 1429–1496, doi:10.1088/0034-4885/67/8/R03.
- Kostrov, B. V. (1974), Seismic moment and energy of earthquakes, and seismic flow of rock, *Izv. Earth Physics*, (1), 23–40, translated by F. Goodspeed.
- Lai, Y.-S., A. B. Movchan, and G. J. Rodin (2002), A study of quasi-circular cracks, *International Journal of Fracture*, 113, 1–25.
- Lavallée, D., and R. J. Archuleta (2003), Stochastic modeling of slip spatial complexities for the 1979 Imperial Valley, California, earthquake, *Geophys. Res. Lett.*, 30(5), 1245–1248.
- Lavallée, D., P. Liu, and R. J. Archuleta (2006), Stochastic model of heterogeneity in earthquake slip spatial distributions, *Geophys. J. Int.*, 165, 622–640, doi:10.1111/j.1365-246X.2006.02943.x.
- Leise, T. L., and J. R. Walton (2001), Dynamically accelerating cracks Part 2: A finite length mode III crack in elastic material, *Quart. Appl. Math.*, 59(4), 601–614.

- Liu-Zeng, J., T. Heaton, and C. DiCaprio (2005), The effect of slip variability on earthquake slip-length scaling, *Geophys. J. Int.*, *162*, 841–849, doi:10.1111/j.1365-246X.2005.02679.x.
- Madariaga, R. (1977), High-frequency radiation from crack (stress drop) models of earthquake faulting, *Geophys. J. R. Astron. Soc.*, *51*, 625–651.
- Madariaga, R. (1979), On the relation between seismic moment and stress drop in the presence of stress and strength heterogeneity, *J. Geophys. Res.*, *84*(B5), 2243–2250.
- Madariaga, R. (1983), High-frequency radiation from dynamic earthquake fault models, *Ann. Geophys.*, *1*, 17–23.
- Mai, P. M. (2004), SRCMOD: A database of finite-source rupture models, [www.seismo.ethz.ch/srcmod](http://www.seismo.ethz.ch/srcmod), last accessed December 2006.
- Mai, P. M., and G. C. Beroza (2002), A spatial random field model to characterize complexity in earthquake slip, *J. Geophys. Res.*, *107*(B11), 2308, doi:10.1029/2001JB000588.
- Mai, P. M., P. Spudich, and J. Boatwright (2005), Hypocenter locations in finite-source rupture models, *B. Seismol. Soc. Am.*, *95*(3), 965–980, doi:10.1785/0120040111.
- Mai, P. M., P. Somerville, A. Pitarka, L. Dalguer, H. Miyake, G. Beroza, S.-G. Song, and K. Irikura (2006), Fracture-energy scaling in dynamic rupture models of past earthquakes, in *Earthquakes: Radiated energy and the physics of faulting*, *Geophysical Monograph Series*, vol. 170, edited by R. Abercrombie, A. McGarr, and H. Kanamori, pp. 283–293, AGU.
- McGarr, A., J. B. Fletcher, and N. M. Beeler (2004), Attempting to bridge the gap between laboratory and seismic estimates of fracture energy, *Geophys. Res. Lett.*, *31*, L14606, doi:10.1029/2004GL020091.
- McGuire, J. J., L. Zhao, and T. H. Jordan (2002), Predominance of unilateral ruptures for a global catalog of large earthquakes, *B. Seismol. Soc. Am.*, *92*(8), 3309–3317.
- Miyatake, T. (1992a), Reconstruction of dynamic rupture process of an earthquake with constraints of kinematic parameters, *Geophys. Res. Lett.*, *19*, 349–352.
- Miyatake, T. (1992b), Dynamic rupture process of inland earthquakes in Japan: weak and strong asperities, *Geophys. Res. Lett.*, *19*, 1041–1044.
- Nielsen, S. B., and K. B. Olsen (2000), Constraints on stress and friction from dynamic rupture models of the 1994 Northridge, California, earthquake, *Pure Appl. Geophys.*, *157*, 2029–2046.

- Oglesby, D. D., and S. M. Day (2002), Stochastic fault stress: Implications for fault dynamics and ground motion, *B. Seismol. Soc. Am.*, *92*(8), 3006–3021.
- Ohnaka, M. (2003), A constitutive scaling law and a unified comprehension for frictional slip failure, shear fracture of intact rock, and earthquake rupture, *J. Geophys. Res.*, *108*(B2), 2080, doi:10.1029/2000JB000123.
- Okada, Y. (1992), Internal deformation due to shear and tensile faults in a half-space, *B. Seismol. Soc. Am.*, *82*(2), 1018–1040.
- Olsen, K. B., R. Madariaga, and R. J. Archuleta (1997), Three-dimensional dynamic simulation of the 1992 Landers earthquake, *Science*, *278*, 834–838.
- Olsen, K. B., S. M. Day, J. B. Minster, Y. Cui, A. Chourasia, M. Faerman, R. Moore, P. Maechling, and T. Jordan (2006), Strong shaking in Los Angeles expected from southern San Andreas earthquake, *Geophys. Res. Lett.*, *33*, L07305, doi:10.1029/2005GL025472.
- Olson, A. H., J. A. Orcutt, and G. A. Frazier (1984), The discrete wavenumber / finite element method for synthetic seismograms, *Geophys. J. R. Astron. Soc.*, *77*, 421–460.
- Olson, E. L., and R. M. Allen (2005), The deterministic nature of earthquake rupture, *Nature*, *438*, 212–215, doi:10.1038/nature04214.
- Peyrat, S., and K. B. Olsen (2004), Nonlinear dynamic rupture inversion of the 2000 Western Tottori, Japan, earthquake, *Geophys. Res. Lett.*, *31*, L05604, doi:10.1029/2003GL019058.
- Peyrat, S., K. Olsen, and R. Madariaga (2001), Dynamic modeling of the 1992 Landers earthquake, *J. Geophys. Res.*, *106*(B11), 26,467–26,482.
- Richardson, E., and T. H. Jordan (2002), Seismicity in deep gold mines of South Africa: Implications for tectonic earthquakes, *B. Seismol. Soc. Am.*, *92*, 1766–1782.
- Ripperger, J., P. M. Mai, and J.-P. Ampuero (2005), Nucleation and propagation of dynamic earthquake rupture under constrained stochastic shear stress, *EOS Trans. AGU*, *86*(52), Fall Meet. Suppl., Abstract S53A-1081.
- Ripperger, J., J.-P. Ampuero, P. M. Mai, and D. Giardini (2007), Earthquake source characteristics from dynamic rupture with constrained stochastic fault stress, *JGR*, *112*, B04311, doi:10.1029/2006JB004515.
- Rivera, L., and H. Kanamori (2005), Representations of the radiated energy in earthquakes, *Geophys. J. Int.*, *162*, 148–155, doi:10.1111/j.1365-246X.2005.02648.x.

- Rose, L. R. F. (1976), On the initial motion of a Griffith crack, *Int. J. Fracture*, *12*(6), 829–841.
- Rundle, J., E. Preston, S. McGinnis, and W. Klein (1998), Why earthquakes stop: Growth and arrest in stochastic fields, *Phys. Rev. Lett.*, *80*(25), 5698–5701.
- Sekiguchi, H., K. Irikura, T. Iwata, Y. Takehi, and M. Hoshiya (1996), Determination of the location of faulting beneath Kobe during the 1995 Hyogo-ken Nanbu, Japan, earthquake from near-source particle motion, *Geophys. Res. Lett.*, *23*(4), 387–390.
- Shakal, A., H. Haddadi, V. Graizer, K. Lin, and M. Huang (2006), Some key features of the strong-motion data from the M6.0 Parkfield, California, earthquake of 28 September 2004, *B. Seismol. Soc. Am.*, *96*(4b), S90–S118, doi:10.1785/0120050817.
- Smith, D. E. (2006), A new paradigm for interpreting stress inversions from focal mechanisms: How 3D stress heterogeneity biases the inversions toward the stress rate, PhD thesis, Calif. Inst. Tech., Pasadena CA.
- Somerville, P., K. Irikura, R. Graves, S. Sawada, D. Wald, N. Abrahamson, Y. Iwasaki, T. Kagawa, N. Smith, and A. Kowada (1999), Characterizing crustal earthquake slip models for the prediction of strong ground motion, *Seis. Res. Lett.*, *70*(1), 59–80.
- Somerville, P. G., N. F. Smith, R. W. Graves, and N. A. Abrahamson (1997), Modification of empirical strong ground motion attenuation relations to include the amplitude and duration effects of rupture directivity, *Seis. Res. Lett.*, *68*(1), 199–222.
- Spudich, P., and L. Xu (2003), Software package COMPSYN: Programs for earthquake ground motion calculation using complete 1-D Green's functions, in *International Handbook of Earthquake & Engineering Seismology, International geophysics series*, vol. 81, edited by W. H. K. Lee, H. Kanamori, P. Jennings, and C. Kisslinger, Academic Press, Amsterdam.
- Steketee, J. A. (1958), On Volterra's dislocation in a semi-infinite elastic medium, *Can. J. Phys.*, *36*, 192–205.
- Uenishi, K., and J. R. Rice (2003), Universal nucleation length for slip-weakening rupture instability under nonuniform fault loading, *J. Geophys. Res.*, *108*(B1), 2042, doi:10.1029/2001JB001681.
- Uenishi, K., and J. R. Rice (2004), Three-dimensional rupture instability of a slip-weakening fault under heterogeneous loading, *Eos Trans. AGU*, *85*(47), Fall Meet. Suppl., Abstract S13E-04.

- Venkataraman, A., G. C. Beroza, S. Ide, K. Imanishi, H. Ito, and Y. Iio (2006), Measurements of spectral similarity for microearthquakes in western Nagano, Japan, *J. Geophys. Res.*, *111*, B03303, doi:10.1029/2005JB003834.
- Voss, R. F. (1988), Fractals in nature: From characterization to simulation, in *The science of fractal images*, edited by H. O. Peitgen and D. Saupe, pp. 21–70, Springer-Verlag, New York.
- Wald, D., and T. Heaton (1994), Spatial and temporal distribution of slip for the 1992 Landers, California, earthquake, *B. Seismol. Soc. Am.*, *84*, 668–691.
- Wald, D. J., V. Quitoriano, T. H. Heaton, and H. Kanamori (1999), Relationships between peak ground acceleration, peak ground velocity and Modified Mercalli Intensity in California, *Earthquake Spectra*, *15*(3), 557–564.
- Wells, D. L., and K. J. Coppersmith (1994), New empirical relationships among magnitude, rupture length, rupture width, rupture area, and surface displacement, *B. Seismol. Soc. Am.*, *84*(4), 974–1002.
- Wesnousky, S. G. (1988), Seismological and structural evolution of strike-slip faults, *Nature*, *335*(6188), 340–342.
- Wu, H.-Y., K.-F. Ma, M. Zoback, N. Boness, H. Ito, J.-H. Hung, and S. Hickman (2007), Stress orientations of Taiwan Chelungpu-Fault Drilling Project (TCDP) hole-A as observed from geophysical logs, *Geophys. Res. Lett.*, *34*, L01301, doi:10.1029/2006GL028050.
- Zeng, Y., J. G. Anderson, and G. Yu (1994), A composite source model for computing realistic synthetic strong ground motions, *Geophys. Res. Lett.*, *21*(8), 725–728.
- Zhang, W., T. Iwata, K. Irikura, H. Sekiguchi, and M. Bouchon (2003), Heterogeneous distribution of the dynamic source parameters of the 1999 Chi-Chi, Taiwan, earthquake, *J. Geophys. Res.*, *108*(B5), 2232.



Seite Leer /  
Blank leaf

# Curriculum Vitae

**Johannes Ripperger**

Born August 24th 1974, Augsburg, Germany

Citizen of Germany

**1995–2001:** Undergraduate Studies in Geophysics at LMU Munich, Germany

**2001:** Diploma thesis ‘Seismic Wave Propagation in the Presence of Volcano Topography’, LMU Munich, Germany

**2001–2002:** Bavarian Earthquake Service, Munich, Germany

**2002–2003:** Swiss Seismological Service, Zurich, Switzerland

**2003–2007:** Doctoral student, Inst. of Geophysics, ETH Zurich, Switzerland

Seite Leer /  
Blank leaf

# Acknowledgments

Finally, I am happy to have reached this point and to be able to say thank you for many things.

I would like to start with Domenico Giardini, who did an excellent job in providing all the ingredients required for a successful PhD thesis. Mille Grazie!

Special thanks to Martin Mai for everything, but most of all for his apparently unlimited supply of enthusiasm, scientific curiosity and optimism. Things a PhD student might happen to run out of during certain stages of his thesis. Tausend Dank!

Jean-Paul Ampuero, joining the group in the second half of the thesis, quickly became a great assistance in many ways. I would award him an extra doctoral degree for all the contributions to my thesis. Muchas Gracias Pablo!

I would also like to thank Raul Madariaga for some interesting scientific discussions and for agreeing to be co-examiner on my jury. Muchas Gracias!

An extra thanks goes also to Stefan Wiemer for setting up and running the whole project together with Martin. Vielen Dank!

Much of my work would not have been possible without the use of software and codes I received from other people. Although some of them have already been mentioned briefly in the acknowledgments section of the individual papers, I want to take the opportunity to thank them again: Joe Andrews for his DYNELF code, Eric Dunham for the MDSBI code and kind support along with it, Pablo and Martin for various Matlab scripts, Banu for the Newmark method along with friendly explanations. Thank you very much!

But since computers do not only solve problems but rather often produce problems, its good to have people around to help you also with all the hard- and software related mysteries that inevitably appear. So I am grateful to Bongo for support regarding the Alpha cluster, to Jochen and Danijel for various tips and hints and for keeping the Marx Brothers alive and finally to Stefan Heimers for the higher level magic he can do on Linux machines. Vielen Dank!

The final assemblage of the thesis was facilitated very much by the Latex template which seems to have been passed on with slight modifications from Danijel to Jochen to Gregor and finally to me. Danke Leute!

In general I would like to thank all my colleagues at the Swiss Seismological Service; without exceptions I met kind and friendly people there. However I would like to point out André and Elisabeth, who were extremely helpful in dealing with all the smaller and larger logistical and administrative tasks that came my way. Merci Vilmols!

Since work is not everything, I would like to thank all the people that made life enjoyable in one way or the other:

Sjonni for relaxed evenings on his roof terrace, Danijel for all the Punk concerts and long discussions on everything, Jochen, Miro, Thomas, Henriette and Falko for the fun together, Damiano for real Italian Pasta, Sune and Morten for pre-concert paranoia, Christa & Ralf for always being great hosts during numerous visits in Munich, Michael, Olaf and Michelle for the rare, but much appreciated extended lunch breaks and everybody I might have forgotten due to the special mental conditions in this final thesis stage. Thanks a lot!

I am lucky to have received unconditional support from my parents through all the years. Auch an dieser Stelle herzlichen Dank für alles!

Finally my biggest thanks goes to Sonja for exploring the valleys and summits of the Swiss alps together with me as well as the highs and lows of life. She dared to take on my name during the course of this thesis. Vielen Dank für die gemeinsame Zeit, bis hierhin und weiter.

Zurich, January 2007